

UNIVERSITÀ DEGLI STUDI DI CATANIA

IN CONVENZIONE CON

UNIVERSITÀ DEGLI STUDI DI PALERMO

**TESI PER IL CONSEGUIMENTO DEL TITOLO DI DOTTORE DI RICERCA IN
SCIENZA DEI MATERIALI E NANOTECNOLOGIE - XXXII CICLO**

**Versatile Pulsed Laser Technique to
prepare Metal Nanoparticles and
Perovskite Thin Films**

Maria Censabella

TUTOR: PROF.SSA M.G. GRIMALDI

PROF. F. RUFFINO

COORDINATORE: PROF.SSA M.G. GRIMALDI



UNIVERSITÀ DEGLI STUDI DI CATANIA

IN CONVENZIONE CON



UNIVERSITÀ DEGLI STUDI DI PALERMO

**DOTTORATO DI RICERCA IN
SCIENZA DEI MATERIALI E NANOTECNOLOGIE - XXXII CICLO**

Maria Censabella

**Versatile Pulsed Laser Technique to
prepare Metal Nanoparticles and
Perovskite Thin Films**

TUTOR: PROF.SSA M.G. GRIMALDI

PROF. F. RUFFINO

COORDINATORE: PROF.SSA M.G. GRIMALDI

TESI PER IL CONSEGUIMENTO DEL TITOLO DI DOTTORE DI RICERCA

**Versatile Pulsed Laser Technique to prepare Metal
Nanoparticles and Perovskite Thin Films**

Maria Censabella – maria.censabella@gmail.com

Ph. D. Thesis - University of Catania (Italy)

Printed in Catania, January 2019

*“Everyone knew it was impossible,
until a fool who didn’t know
came along and did it”
— Albert Einstein*

*“Research is what I’m doing
when I don’t know
what I’m doing”*

*“I have learned to use the word ‘impossible’
with greatest caution”*

— Wernher von Braun

List of abbreviations

0-D: Zero Dimensional
1-D: One Dimensional
2-D: Two Dimensional
3-D: Three Dimensional
AFM: Atomic Force Microscopy
BZY: Yttrium doped Barium Zirconate
C-AFM: Conductive Atomic Force Microscopy
CVD: Chemical Vapor Deposition
EDX: Energy Dispersive X-ray Spectroscopy
FTO: Fluorine doped Tin Oxide
GB: Grain Boundary
HAADF-STEM: High-Angle Annular Dark Field Scanning Transmission
Electron Microscopy
HTPC: High-Temperature Proton Conductor
ITO: Indium Tin Oxide
MBE: Molecular Beam Epitaxy
MOCVD: Metal-Organic Chemical Vapor Deposition
NP: Nanoparticle
PIXE: Particle Induced X-ray Emission
PLAL: Pulsed Laser Ablation in Liquid
PLD: Pulsed Laser Deposition
PVD: Physical Vapor Deposition
RBS: Rutherford Backscattering Spectrometry
SAED: Selected Area Electron Diffraction
SEM: Scanning Electron Microscopy
SOFC: Solid Oxide Fuel Cell
TEM: Transmission Electron Microscopy
TCO: Transparent Conducting Oxide
UV-Vis: Ultraviolet-Visible Spectroscopy
XRD: X-Ray Diffraction
XRR: X-Ray Reflectometry

Contents

Abstract	13
Chapter 1	17
Nanostructured materials and their laser-based fabrication methods ..	17
1.1 Nanotechnologies and nanostructures.....	17
1.1.1 Introduction	17
1.1.2 Metallic Nanoparticles.....	21
1.1.3 Perovskite Thin Films	23
1.2 Techniques to fabricate nanostructures.....	28
1.3 Laser-based Techniques.....	31
1.3.1 Laser Irradiation and dewetting process	34
1.3.2 Pulsed Laser Ablation in Liquid	36
1.3.3. Pulsed Laser Deposition.....	39
Chapter 1 References	42
Chapter 2	51
Mono- and bimetallic nanoparticles produced by Laser Irradiations of thin films deposited on Transparent Conductive Oxides	51
2.1 Fluorine doped Tin Oxide (FTO).....	52
2.2 Bimetallic PtPd NPs produced by nanosecond laser irradiation on topographically-structured FTO.....	54

2.2.1 Experimental section.....	55
2.2.2 Results and discussion	57
2.3 Characteristics of monometallic Pt and Pd NPs produced on FTO and study of dewetting process on structured substrates	65
2.3.1 Experimental section.....	65
2.3.2 Results and discussion	66
2.4 Conclusions.....	79
Chapter 2 References	80
Chapter 3	87
Laser ablation synthesis of Pd and Pt nanoparticles and study of the charge transfer effect in NPs/Graphene hybrid composites	87
3.1 Experimental section.....	88
3.2 Synthesis by pulsed laser ablation in liquid of mono and bimetallic Pt/Pd nanoparticles	91
3.2.1 Results and discussion	92
3.3 Study of the charge transfer effect in NPs/Graphene hybrid composites	105
3.3.1 Results and discussion	106
3.4 Conclusions.....	120
Chapter 3 References	122
Chapter 4	127
Light-assisted Impedance Studies of Grain Boundaries in the Thin Film Proton Conductors grown by Pulsed Laser Deposition	127

4.1 Experimental section.....	129
4.2 Results and discussion	132
4.3 Conclusions.....	143
Chapter 4 References	144
Summary and Conclusions	147
List of publications.....	149
Conferences	150
Awards.....	151
Schools and Workshops.....	151
Research Period Abroad	153
Curriculum Vitae.....	155
Acknowledgements	157

Abstract

Nanostructures are defined as novel materials whose size of the elemental units has been engineered at the nanoscale. A nanometer is only a one-billionth part of a meter, 1/10000 part of the diameter of human hair or twenty times more than the diameter of the hydrogen atom. Nanotechnology is the manipulation and manufacture of materials and devices on the scale of atoms or small groups of atoms.

Nanomaterials have attracted widespread attention since 1990s due to their tunable physical, chemical and biological properties with enhanced performance over their bulk counterparts. The manipulation of matter at the nanoscale has opened enormous possibilities to meet challenges in different disciplines like optoelectronics, medicine, biotechnology, energy sustainability and engineering of new, effective and efficient devices, drugs or tools.

Due to the exciting nature of nanostructures, nowadays there is an increasing demand towards economical, effective and high-quality nanofabrication. In particular, research efforts are focused on laser-based techniques for the growth and fabrication of nanostructures. In fact, laser-based techniques are simple and environmentally friendly and, in addition, with these methods is possible to control the size, shape and composition of the materials being manufactured.

In the nanoscale, the size, the morphological structure and the shape are the major driving factors for changing the properties of the nanomaterials. Indeed, depending on the overall shape, they are classified as 0-Dimensional (0-D, nanoparticles and nanodots), 1-D (nanowires, nanotubes), 2-D (thin films) or 3-D (bulk materials). This classification is highly dependent on the electron movement along the dimensions in the nanostructures.

Among the various nanomaterials, metallic nanoparticles (NPs) have received great interest by scientific community due to the huge surface-volume ratio and their optical, electrical and magnetic properties, which make them useful for many applications in several fields, such as medicine,

catalysis, optics, cosmetics, renewable energies, microelectronics and environmental remediation. In particular, mono- and bimetallic Pt and Pd NPs find important devices applications in catalysis, hydrogen storage, direct alcohol fuel cell, reduction of environmental pollutants and for sensing detection.

On the other hand, in the last twenty years, the interest in Perovskite-structures has been literally booming due to their wide range of applications in photovoltaic field, sensors, random access memories, fuel cells, piezoelectric devices and capacitors. In particular, Y-doped Barium Zirconate (BaZrO_3) has been recognized as one of the most promising proton conductors due to its good chemical stability and high proton conductivity. It may become an excellent electrolyte for Solid Oxide Fuel Cells if the blocking effect of conductivity at grain boundary is solved.

Aim of the work reported in the present thesis is the synthesis of different nanomaterials with the use of different laser-based techniques: laser irradiation, Pulsed Laser Ablation in Liquid and Pulsed Laser Deposition. In particular, I fabricated mono- and bimetallic Pt/Pd nanoparticles and perovskite Y-doped BaZrO_3 thin films and their complete characterizations have been performed.

This dissertation is structured as follows:

Chapter 1: in the first part of the chapter, a brief introduction to the world of nanotechnology and nanostructures is presented, with a focus on the importance of Pt and Pd nanoparticles and on perovskite Y-doped BaZrO_3 thin films. The second part describes the nano-fabrication techniques, focusing particularly on laser-based techniques. In particular, the three different techniques used in the thesis to fabricate nanomaterials are described: laser irradiation, Pulsed Laser Ablation in Liquid and Pulsed Laser Deposition.

Chapter 2: the exploitation of the laser irradiation technique to fabricate monometallic and bimetallic Pd and Pt NPs supported on Fluorine-doped Tin Oxide is presented. In particular, the laser irradiation is used to induce the dewetting process in order to obtain nanoparticles starting by layers deposited

on structured surface. Then, the produced nanoparticles are characterized from a structural and morphological point of view. In addition, an elucidation of the effect of the substrate's topography on the dewetting process is shown.

Chapter 3: describes the synthesis of ligand-free mono- and bi-metallic Pd and Pt nanoparticles by nanosecond Pulsed Laser Ablation in Liquid environment. The chemical, structural and morphological characterization was performed on the produced particles. In addition, the nanoparticles have been used to decorate graphene layers by simple spin-coating of the colloidal solutions onto the substrates, obtaining NPs/graphene nanocomposites. Furthermore, a study on the charge transfer effect between nanoparticles and graphene is presented.

Chapter 4: shows the fabrication and the characterization of perovskite thin films of 20% Y-doped BaZrO₃ by using Pulsed Laser Deposition on single crystal substrate ((001) MgO). The crystalline structure, the thickness and the electrical performance of these films have been characterized. In addition, preliminary results on the increasing of the grain boundary conductivity due to the UV illumination is showed.

Summary and Conclusion: the basic results of the work thesis are outlined.

Chapter 1

Nanostructured materials and their laser-based fabrication methods

1.1 Nanotechnologies and nanostructures

1.1.1 Introduction

Nanotechnology is the manipulation and manufacture of materials and devices on the scale of atoms or small groups of atoms. The “nanoscale” is typically measured in nanometers, being a nanometer a billionth of a meter (10^{-9} m). The concept of nanotechnology dates back to 1959, when Feynman, during his famous lecture at Caltech “There is Plenty of Room at the Bottom”, considered the possibility of maneuvering things atom by atom [1]. Since then the nanomaterials are described as materials with length of 1-100 nm in at least one dimension [2].

The advances in nanotechnology over the years have made nanostructures potential targets of industries and scientific community due to their unique characteristics that differ from the bulk materials. A bulk material has constant physical properties regardless of their size and shape, but at the nanoscale, the size and shape are the major driving factors for changing their physical-chemical properties. In fact, all materials, metals, semiconductors or insulators, at nanoscale exhibit some prominent effects, as mentioned below [3,4]:

- a. *Electrical properties*: the electrons can't move freely due to the size in the nanometer range, this confinement resulted in the changes in electrical properties, such as the bulk conductor materials behaving as

- superconductors (and viceversa) at nanoscale. Or ferroelectric materials become non-ferroelectric at reduced sizes.
- b. *Optical properties*: the color and transparency of materials change by changing the size of nanoparticles. The confinement of the electrons causes them to react to light differently. For example, gold appears golden at the macroscale, but the nanosized gold particles are red.
 - c. *Thermal properties*: it is found that melting point is lowered with decreasing particle size. It may be reduced to half of the original. Again, at the macro scale, gold has a melting point of 1064°C but by decreasing the particle size from 100 to 10 nm diameter, its melting temperatures drops up to 100°C.
 - d. *Mechanical properties*: it has been observed that nanocrystalline materials have reduced elastic modulus and density by 30% or less. In addition, with decreasing size, hardness or strength increases by 4-5 times; diffusivity also increases up to double of the initial.
 - e. *Magnetic properties*: Curie temperature of ferromagnetic materials decreases with decreasing size of nanoparticles, and hence the substance remains paramagnetic even below usual Curie temperature showing super paramagnetism.

All the afore mentioned changes in the properties of nanostructures are mainly due to [3,4]:

- *Increase in surface area to volume ratio*: atoms at surface or interface have different environment and bonding configuration, therefore these exhibit different characteristics. For example in the case of nanoparticles, as size is reduced, relative number of atoms on surface increases inversely as particle size. For small sizes, less than 100 nm, the fraction of surface atoms is large and therefore influences the properties by greater amount making the properties size dependent.
- *Quantum size effect*: when the size of the structure is comparable to phase coherent length of electrons, the energy spectrum is quantized into discrete levels. The effect is observable for particle sizes of the order of few 10 nm. Quantum size effect is more

pronounced in semiconductor nanoparticles because of moderate forbidden energy gap. Quantum size effect makes the energy states at the edges of valence and conduction bands forbidden, increasing the effective band gap, which affects the electronics and optical properties.

Nowadays, many types of nanostructures have been reported in literature and many other varieties are predicted to appear in the future. Therefore, the need for their classification has ripened. The first idea for nanomaterials classification was given by Gleiter et al. [5]. Here, nanomaterials were classified depending on their crystalline form and chemical composition. However, this scheme was not fully complete, because the dimensionality was not considered [6]. In 2007, Pokropivny and Skorokhod made a new scheme of classification for nanostructures which included the recently developed composites such as 0 Dimensional (0-D), 1 Dimensional (1-D), 2 Dimensional (2-D) and 3 Dimensional (3-D), as shown in figure 1.1 [7]. This classification is highly dependent on the electron movement along the dimensions in the nanostructures. In particular, for a bulk (3-D) material charge carriers are free to move in all directions; whereas for a planar material or thin film (2-D, fig. 1.1.a), charge carriers are confined only in a plane. The charge carriers in a wire or 1-D (Nanotubes, Nanowires, Nanosheets, Quantum wires, fig. 1.1.b) material will be allowed to flow only in one direction; whereas charge carriers inside a cluster, nanoparticle or quantum dot (0-D, fig.1.1.c) are confined in a very small region in space. This gives rise to quantum confinement and most of the properties vary due to this effect.

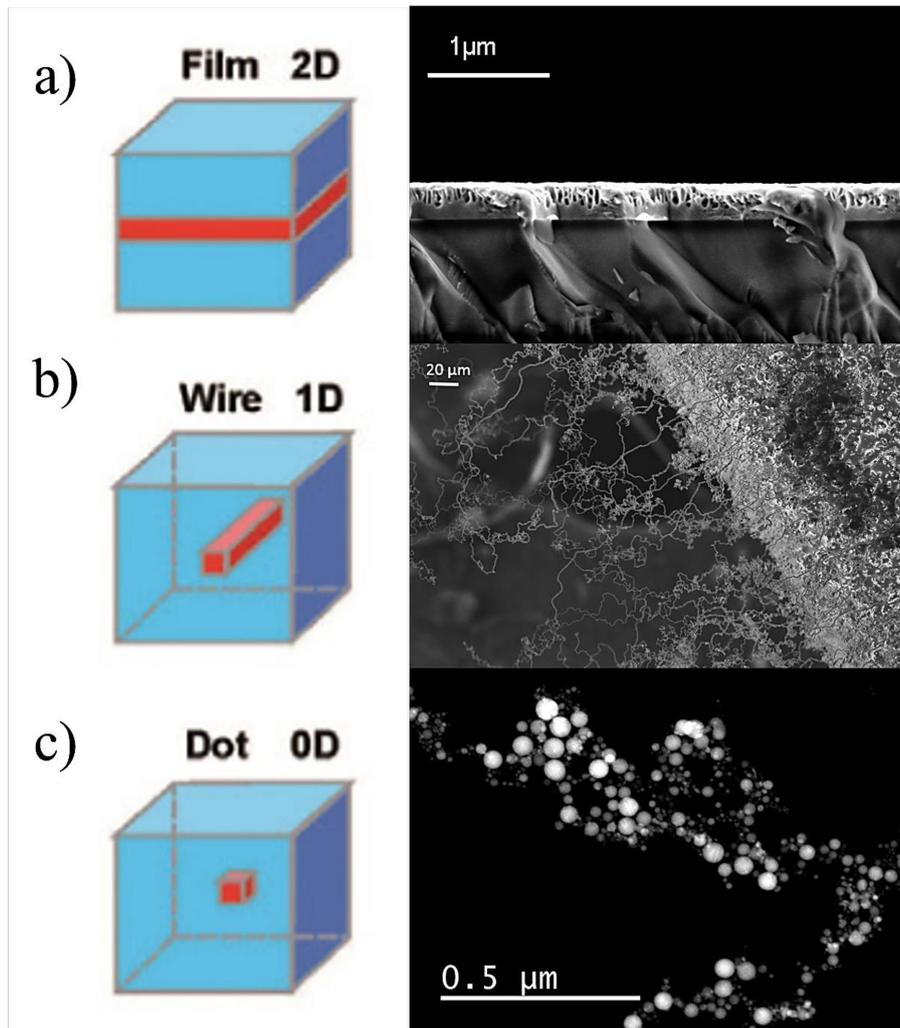


Figure 1.1 Nanomaterials with different morphologies: (a) thin film of nanoporous Ge on Si (2-D), (b) Si nanowires (1-D) and (c) Pt nanoparticles (0-D).

1.1.2 Metallic Nanoparticles

Metallic nanoparticles (NPs) have received great attention by scientific community due to the huge surface-volume ratio compared to the correspondent bulk materials and their optical, electrical and magnetic properties, which make them useful for many application in several fields (fig. 1.2): medicine, catalysis, optics, cosmetics, renewable energies, inks, microelectronics, medical imaging, environmental remediation [8-18].

The physicochemical properties of metal nanoparticles are dictated by various attributes like size, shape, architecture, crystallinity and composition.

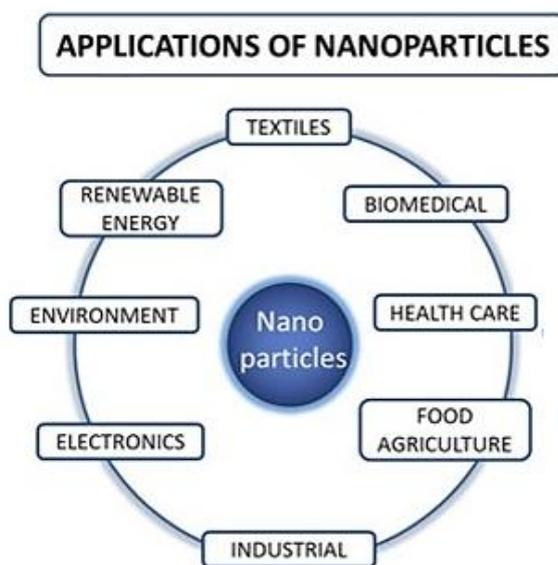


Figure 1.2 Schematic summary of various application fields of nanoparticles.

For examples, noble metals nanoparticles (Au, Pt, Pd, Ag, Rh, Ru, Ir and Os) show unique properties, such as resistance to corrosion and oxidation, high melting point, non-reactiveness, high reduction potential, high ionization energy. Compared to other non-noble metals, they show surface plasmon resonance, antibacterial action and, in the field of catalysis, they increase the yield of redox reactions [19-23]. For these unique properties, noble metals

NPs have attracted great interest to design of functional nanoparticles for both basic as well as applied research.

In particular, among noble metals, Pt and Pd NPs find important devices applications in catalysis, hydrogen storage, direct alcohol fuel cell, reduction of environmental pollutants and for sensing detection (fig. 1.3) [24-27]. For example, Pt is the most common catalyst, but it is expensive. Instead, palladium is cheaper than Pt and more abundant, making it a good substitute for Pt in Pt-based catalyst [24]. Furthermore, Pt and Pd are suggested as key elements for the hydrogen economy, as result of their synergic catalytic and hydrogen absorbing properties. Indeed, Pd is able to absorb large amounts of hydrogen, but its hydrogen solubility decreases as the nanoparticle size decreases; on the other hand, Pt NPs exhibit effective hydrogen storage ability, although bulk Pt is a poor hydrogen absorber [28-29]. These incredible differences have prompted researchers to look for a possible use of these nanoparticles in bimetallic form. Indeed, bimetallic nanoparticles improved the properties of monometallic ones, due to synergistic effects between the two elements [30-33]. In particular, in the field of catalysis, bimetallic NPs show superior catalytic properties than their monometallic counterparts [30,33]. For hydrogen storage applications, the amount of hydrogen absorption of PdPt NPs was found to be greater than that of Pd NPs [28].

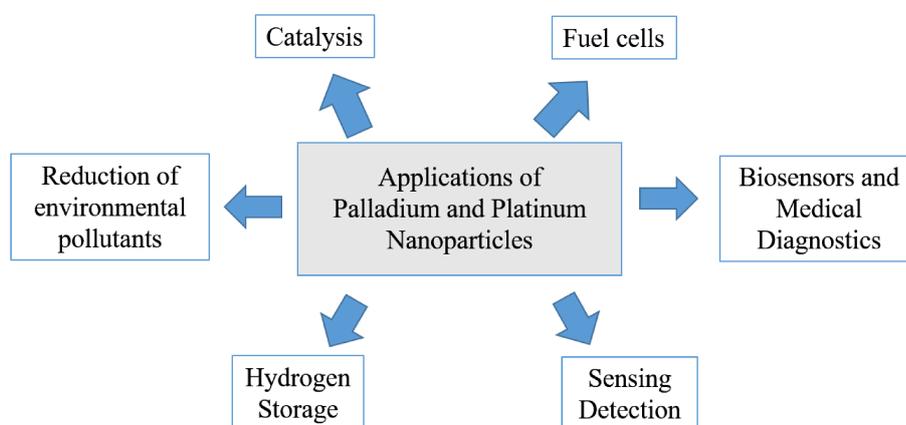


Figure 1.3 Summary of some applications of Pt and Pd NPs.

Therefore, more and more research groups are focused on the manufacture of monometallic and bimetallic Pt and Pd nanoparticles, because they have bright future in broad research areas of high-tech applications.

1.1.3 Perovskite Thin Films

The mineral perovskite (CaTiO_3) was discovered in the Ural mountains of Russia by Gustav Rose (1839). It was later named after a Russian mineralogist L.A. Perovski, who first characterized the structure [34]. Research on perovskites did not catch on until the mid-40s, when there was a dramatic increase in solid-state research. Since the 1940s, perovskite materials have been a hot topic of research, and it remains, still, a promising research frontier for future.

Nowadays the term perovskite is used to indicate materials that have a perovskite type structure, therefore, the terms "perovskite" and "perovskite structure" are used interchangeably.

The perovskite structure has the general stoichiometry ABX_3 and a cubic crystal structure, where "A" and "B" are cations and "X" is an anion. The perovskite structure is adopted by many oxides that have the chemical formula ABO_3 , with small B cations and larger A cations, as shown in fig. 1.4 [35].

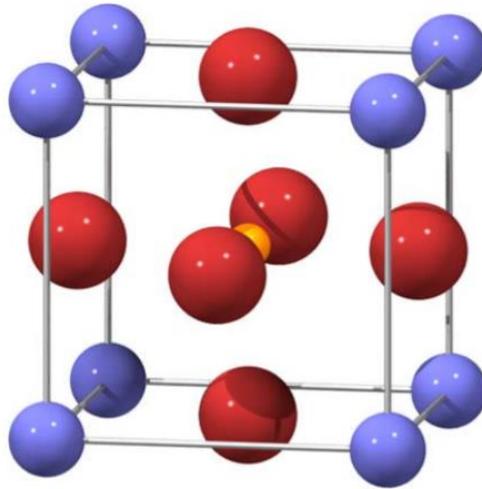


Figure 1.4 Cubic perovskite unit cell. Blue spheres represent the A cations, yellow spheres represent the B cations and red spheres represent oxygen anions forming an octahedra.

Perovskite-structure ceramics have a wide range of applications in technology, especially in solid-state ionics. Table 1 lists the properties and applications of some commonly studied perovskites [36]. Perovskites are currently used in sensors, random access memories [37], piezoelectric devices [38], actuators, tunable microwave devices displays [39], transducers, photovoltaic field, wireless communications [40] and capacitors [41]. In several applications perovskites proved to have great interest due to their useful properties in surface acoustic wave signal processing devices, electrochromic, switching, image storage, filtering and photochromic [42].

Property	Application	Material
	SOFC electrolyte	
Proton conductivity	Hydrogen sensor	BaCeO ₃ , SrCeO ₃ BaZrO ₃
	H ₂ production/ extraction	
Ionic conductivity	Solid electrolyte	(La,Sr)(Ga,Mg)O _{3-δ}
Mixed conductivity	SOFC electrode	La(Sr,Ca)MnO _{3-δ} , LaCoO ₃ (La,Sr)(Co,Fe)O _{3-δ}
Ferroelectric/ piezoelectric	Piezoelectric transducer Thermistor, actuator	BaTiO ₃ , Pb(Zr,Ti)O ₃ Pb(Mg,Nb)O ₃
Catalytic	Catalyst	LaFeO ₃ , La(Ce,Co)O ₃
	Multilayer capacitor	
Electrical/ dielectric	Dielectric resonator Thin film resistor	BaTiO ₃ , BaZrO ₃
Magnetic	Magnetic memory Ferromagnetism	GdFeO ₃ , LaMnO ₃
Optical	Electrooptical modulator Laser	(Pb,La)(Zr,Ti)O ₃ YAlO ₃ , KNbO ₃
Super-conductivity	Superconductor	Ba(Pb,Bi)O ₃ , BaKBiO ₃

Table 1 Properties and applications of perovskites [36].

Perovskites have an unusually high tolerance for oxygen ion vacancies, which makes it an ideal electrolyte material for Solid Oxide Fuel Cells (SOFCs) and, in particular, for High-Temperature Proton Conductors (HTPCs). For many years the SOFCs' research has been focused on oxygen-ion conductors, but in recent years, the interest towards HTPCs is increasing.

In the ABO_3 perovskite structure shown in figure 1.4. the B cation, which is usually a transition metal or a rare earth (usually Ce or Zr), has +4 valence and forms a six-coordinated octahedron with its neighboring oxygen ions, being itself located in the centre, while the A cation presents a +2 valence (Ba, Ca and Sr), and its coordination number is 12. The partial substitution of the B cation with a trivalent dopant M(III) (Y, In, Eu, Sm, Nd) results in the creation of oxygen vacancies for balancing the valence charge, leading to the general formula of HTPC perovskite-type oxides that can be written $AB_{1-x}M_xO_{3-\delta}$, where δ is the oxygen deficiency per unit cell [43]. The oxygen vacancies play an important role in the proton conduction in a HTPC. Protons incorporated in this structure migrate between adjacent oxygen sites via a Grotthuss-type [44] mechanism shown in figure 1.5: the bond between the cation (red sphere) and the oxygen A bends, so that the proton can move from the oxygen ion A to the oxygen ion B. Then, the bond length between A and B is shortened and this reduces the energetic barrier for proton transfer, that can form a bond with the oxygen atom B (from position 1 to position 2). From this position, the proton can move towards another oxygen ion by means of rotational motion around the oxygen B (from 2 to 3) and then, the same processes as described are repeated [43].

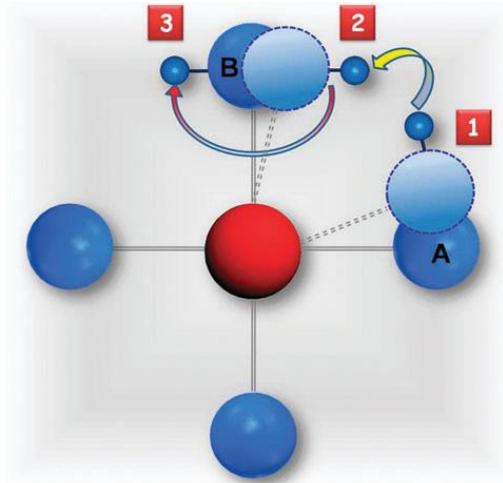


Figure 1.5 Schematic proton transfer mechanism in a HTPC [43].

The perovskite structures can be used as electrolyte in a HTPC only if they exhibit good chemical stability and a good conductivity. Among, the oxide proton conductor, Yttrium doped Barium Cerate (Y-doped BaCeO_3) and Zirconate (Y-doped BaZrO_3) show the best performance. In particular, Y: BaCeO_3 shows the highest proton conductivity, but low chemical stability, because reacts with water and carbon dioxide [45,46]. On the other hand, Y: BaZrO_3 has good chemical stability but his poor sinterability leads to the presence of large grain boundary regions, resulting in quite low conductivity [45, 47,48]. Anyway, Kreuer has assumed that the grain interior conductivity of Y-doped BaZrO_3 , particularly at low temperature, is higher than that of the best oxide-ion conductors. In particular, the bulk conductivity increases (but not linearly) with the dopant concentration. The higher proton conductivity has been reported so far for BaZrO_3 doped with 20mol% of Yttrium [49].

In the last twenty years the interest in fuel cell applications of these materials has been literally booming. In particular, Y-doped BaZrO_3 has been recognized as one of the most promising proton conductors, and it may become an excellent electrolyte for SOFCs if the blocking effects at the grain boundary is solved. For this purpose, the fabrication methods are particularly

needed to process thin and dense membranes with small grain boundary volumes.

1.2 Techniques to fabricate nanostructures

A variety of methods are used to obtain nanostructured material. Currently there are two approaches (fig. 1.6):

1. *Top-down approach*: larger materials are reduced to nano-size dimensions;
2. *Bottom-up approach*: the structures are built by assembling atom by atom to the nanometer size.

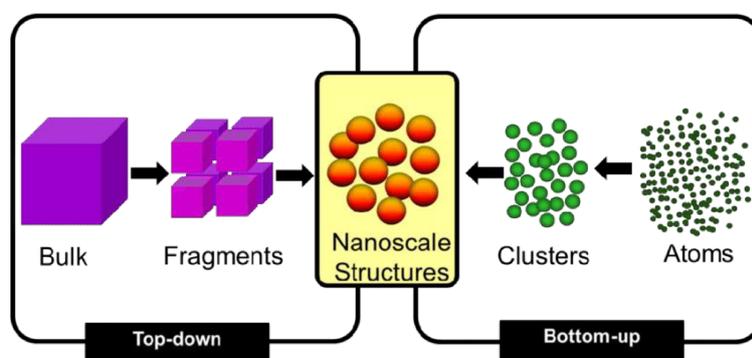


Figure 1.6 Top-down and bottom-up approaches for the synthesis of nanostructures.

Top-down methods of fabrication of nanomaterials include: milling (mechanical and mechanochemical), etching and lithography [50]. There are different bottom-up fabrication approaches, such as the wet chemical method [51], physical vapor deposition (PVD) [52], pulsed laser ablation (PLD) [53], metal-organic chemical vapor deposition (MOCVD) [54], molecular beam epitaxy (MBE) [55], sputtering [56], electrospinning [57] and flux method [58]. Some of the principal characteristics of these fabrication techniques include controllability of fabrication conditions (e.g. deposition rate,

temperature and pressure), uniformity of nanostructure, high-quality nanomaterial with limited impurities, reproducibility, high throughput, choice of substrate [58,59].

The commonly used methods can be categorized as physical and chemical methods. A summary of some physical and chemical methods of the bottom-up and top-down fabrication techniques is shown in figure 1.7.

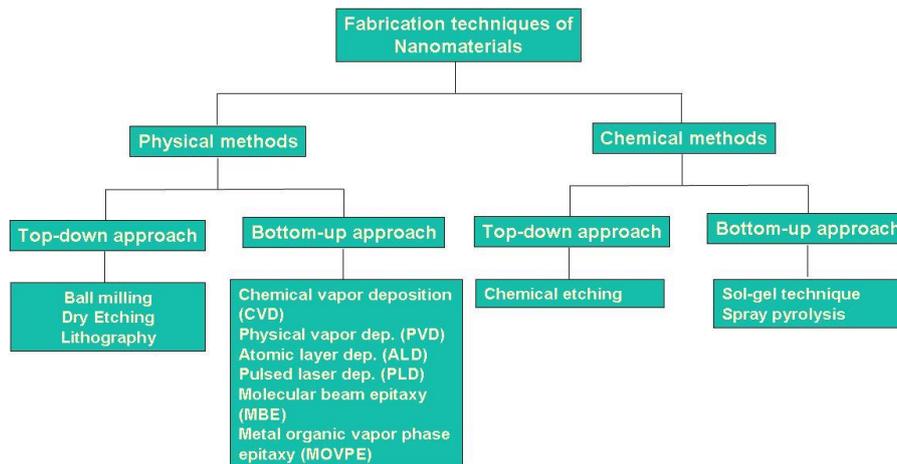


Figure 1.7 Summary of some chemical and physical nanostructure fabrication techniques.

Among the various techniques for the fabrication of nanostructures [50] the most used are:

- *Physical vapor deposition*: the target material is released from a source and transferred to the substrate. Pressure, temperature and carrier gas control the catalyzed process of physical vapor deposition. This technique requires elevated temperature deposition of sublimed source material. Also can incorporate impurities to nanostructures from the reactor chamber or from the use of catalysts in the fabrication;
- *Sputtering deposition*: is a method of thin films deposition by sputtering material from a target. The atoms are ejected from a surface of a material when that surface is struck by sufficiently energetic ions

generated by low-pressure gas plasma (Ar). The sputtered atoms pass through the plasma and deposit on the substrate causing growth of nanocrystals. Film morphology may be altered by the high kinetic energy of sputtered particles due to the atomic mobilization process;

- *Lithographic method*: uses electron beams to remove micro-scale structures from resists, which are precursor materials. The mask image is transferred to a substrate by coating while exposing the resist to electron beams and applying appropriate chemicals to develop the image on the substrate. The cost of using this technique is high (from hundreds of thousands of dollars to millions of dollars);
- *Molecular beam epitaxy*: epitaxial techniques are techniques of arranging atoms in single-crystal fashion on crystalline substrates so that the lattice of the newly grown film duplicates that of the substrate. If the film is of the same material as the substrate, the process is called homoepitaxy. In molecular beam epitaxy the heated single-crystal sample is placed in an ultrahigh vacuum (10^{-10} Torr) in the path of streams of atoms from heated cells that contain the materials of interest. These atomic streams impinge on the surface, creating layers whose structure is controlled by the crystal structure of the surface, the thermodynamics of the constituents, and the sample temperature. Can be used to fabricate nanostructures of different geometries from 1-D to 3-D. The deposition rate of MBE is very low.
- *Pulsed laser deposition*: involves physical vapor deposition of thin films using high-powered beam to strike a deposition material in a vacuum chamber or in presence of some background gas. It can work at a temperature that varies from room temperature to above 1000°C . Temperature, laser energy density, pulse repetition rate, pressure, type of gas inside the chamber and substrate-to-target distance determine the quality of the nanostructures produced

1.3 Laser-based Techniques

A laser (Light Amplification by Stimulated Emission of Radiation) is a device that emits light (i.e., electromagnetic radiation) through the process of stimulated emission [60].

Like all great discoveries, even that of the laser started as a joke: “A laser is a solution seeking for a problem”, this is how, in 1960, the first functional laser was described by sceptics who wanted to mock the invention of Theodore Maiman. He constructed the first laser at Hughes Research Laboratories in Malibu. The laser was based on an optical pumping of a ruby crystal using a flash lamp that generated pulsed laser radiation at 694 nm. Many researchers just did not realize the importance of this invention. In fact, the first report on the laser was rejected by reviewers of the journal *Physical Review Letters*, but Maiman turned it to *Nature*, where his paper was published on August 6th 1960 [61].

From then on, lasers have been widely used in several fields: from medical clinics to steel industry, from research laboratories to pointing devices, from dentistry to eye surgery, from cosmetics to building mobile phone.

In the research field, one of the most significant applications is the laser - assisted fabrication of functional materials. The drivers for micro/nano fabrication research are mainly in the renewable energy (e.g., solar panels, fuel cells), catalysis, semiconductor industry (photo-lithography), electronic industry (e.g., display panels), data storage (multi-dimensional data storage), biomedical (e.g., stents, implants, micro-fluidics) and photonic/telecom industries.

The laser-target interaction can lead to an astonishing outcome and can be performed in different environments (gas, liquid or vacuum) in order to fabricate various materials.

The interaction of the material upon laser irradiation can be described as follows: the incident laser pulse penetrates into the surface of the material within a certain penetration depth. This dimension is dependent on the refraction index of the target material and the laser wavelength, and it is usually in the range of 1000-10 nm. The strong electrical field generated by the laser light is sufficient to remove electrons from the penetrated volume, these free

electrons oscillate within the electromagnetic field and transfer their energy colliding with the atoms of the bulk material [62]. At a high laser fluence (density of the laser energy, typically some J/cm^2) the irradiated surface is heated up, ablated, vaporized and converted to plasma, which contains various energetic species, including atoms, electrons, ions, clusters, molecules (Fig. 1.8), and therefore possesses some unique characteristics such as high pressure, temperature and density [63]. After, the large pressure difference between the plasma, produced by the laser, and ambient atmosphere causes a rapid expansion of the plasma plume and then it cools down. Under suitable condensation conditions (temperature and pressure), the plasma species will nucleate and grow into desirable nanostructures, either on a substrate or in a cool liquid medium [64].

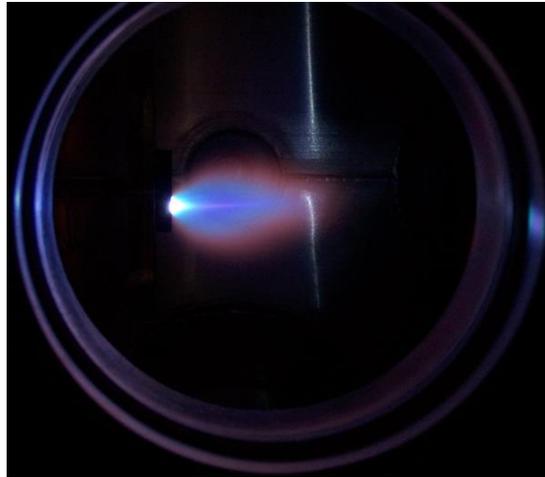


Fig 1.8 Plasma plume ejected from a laser irradiation of $SrRuO_3$ target.

From a quantitative point of view, the laser photons when are absorbed by the irradiated solid give place to an energy source inside the material [60,65-67]. The interaction of the photons with matter occurs mainly through electronic excitations. This results in a non-equilibrium electronic distribution. Then, the electrons thermalization occurs through electron-electron and electron-phonon scatterings. In semiconductors and insulators,

the laser photons absorption results in electrons transitions from the valence band to the conduction band and the subsequent thermalization process occurs by electron-hole recombination, which tends to re-establish the equilibrium condition. Therefore, the thermalization process is dependent on the specific electronic band structure of the material [60,65-67]. However, this recombination process typically occurs in the nanosecond time range scale [65]. The situation is completely different for laser irradiated metals. In this case, the electrons thermalization process is faster (in the femtosecond time range scale) since it is due to the intraband scattering events since the laser photons are absorbed, mainly, by the free electrons of the metal. A first rough approach to describe the metal heating under laser irradiation can be drawn on the basis of the Drude model [65]. Within this model, the electron scattering mean time is connected to the free electrons gas conductivity by $\sigma = ne^2\tau_D/m$, with σ being the conductivity, n being the electron density, m being the electron mass, and τ_D being the electron scattering mean time. This timescale is important for a description of the phenomenon, as it sets the boundary between strictly thermal and possible non-thermal routes to ablation, as well as between “long” and “short” pulses [68]. So, considering a laser pulse of duration τ_{pulse} , the lifetime of excited electrons τ_{ee} and the electron-phonon coupling time τ_{ep} , if $\tau_{pulse} \gg \tau_{ee}, \tau_{ep}$, equilibrium between electrons and phonons prevails throughout the heating stage and phase changes can be regarded as slow thermal processes involving quasi-equilibrium thermodynamics. In contrast, for ultrashort pulses ($\tau_{pulse} \leq 10^{-12}$ s), the material is driven into a highly non-equilibrium state and, in this case, the time with which structural changes take place determines whether thermal mechanisms are involved or not.

In the case of ns pulses, the processes take place in the thermal regime. The hot electrons gas relaxes via electrons-phonons interaction and thermal effects are dominant. In addition, if during heating stage the material reaches temperatures higher than the melting temperature, a portion of the target, of the order of the temperature diffusion length melts and vaporizes. The fluence threshold (F_{th}) is set by the minimum energy required the expulsion of the material: $F_{th} \approx \rho\Omega\sqrt{DT_{pulse}}$, being ρ the material density, Ω the evaporation enthalpy, D the thermal diffusion coefficient.

Here, I present, three different laser-based techniques used to fabricate nanostructures: laser irradiation of thin film deposited on surface, laser ablation in liquid environment and pulsed laser deposition.

1.3.1 Laser Irradiation and dewetting process

The laser radiation can be used to provide the thermal budget required to induce the dewetting process of a thin film, deposited on a functional substrate. In fact, the controlled dewetting process of thin metal films is a promising and powerful patterning strategy for metal nanostructures on surfaces. The application of dewetting is present in a wide range of industrial and scientific areas, where one typical application emerging in recent years is synthesis of nanometer-scale structures [69,70].

The dewetting process is driven by the total surface free energy minimization of the system. The total free energy, associated with the surfaces and interfaces of a film, is minimized if the film breaks to form droplets. The wettability or non-wetting nature of the film on the substrate is defined by the spreading coefficient S [71-74]:

$$S = \gamma_S - \gamma_F - \gamma_{S/F}$$

being γ_S , γ_F , and $\gamma_{S/F}$ the substrate surface free energy, the film surface free energy and the substrate– film interface energy, respectively. If $S > 0$ ($\gamma_F + \gamma_{S/F} < \gamma_S$), the film on the surface is thermodynamically stable and it wets the substrate. When $S < 0$ ($\gamma_F + \gamma_{S/F} > \gamma_S$), the film is thermodynamically unstable and it does not wet the substrate and it is inclined to dewet in droplets. Considering also, the characteristic contact angle, expressed by the Young-Dupree equation [71-74]:

$$\cos \theta_C = \frac{(\gamma_S - \gamma_{F/S})}{\gamma_F}$$

when a thin film wets a substrate $\theta_C < 90^\circ$, as shown in figure 1.9.a, while, a thin film doesn't wet the substrate $\theta_C > 90^\circ$ (fig. 1.9.b).

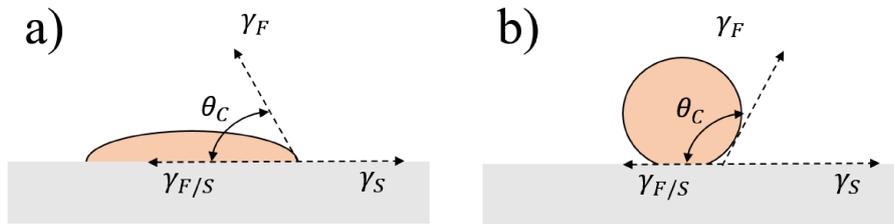


Figure 1.9 Schematic representation of contact angle for thin film that wets a surface (a) and thin film that doesn't wet a surface (b).

In a general dewetting phenomenon, a thin film breaks up into particles via one of three mechanisms [75,76]: (1) heterogeneous nucleation (a surface defect catalyses the process), (2) homogeneous nucleation (the hole's formation caused by thermal density fluctuations and (3) spinodal dewetting (determined by the enhancement of periodical film thickness fluctuation).

In particular, it is widely accepted that the dewetting process starts by the film perforation, which leads to holes' formation in the film. These perforations are likely to occur where the film is thinner since the thermal budget required for melting is lower for thinner films [77]. Then, the holes reach the film surface and start to grow; as a consequence of mass conservation and also a curvature gradient at their edges, the holes develop a thickened rim. At this point, the corners of the hole growing become unstable and the rims break by a fingering instability with the consequent formation of material lines. Subsequently the lines decay into droplets (the nanoparticles) through a Rayleigh-like instability. A schematic representation of dewetting process is shown in figure 1.10. The mean diameter of the obtained nanoparticles and the spacing between the particles depend on the initial film thickness h , with a power law relation.



Figure 1.10 Schematic representation of a dewetting process leading to the formation of droplets from a continuous film [75].

In the specific case of thin metal films deposited on non-metal substrates (e.g. oxides), the films are, typically, thermodynamically unstable at elevated temperatures, as a consequence of the fact that, typically, metal-metal interaction is much stronger than metal–non-metal interaction. The energetic budget needed to start the dewetting process of the film can be furnished to the film by standard thermal annealing or, alternatively, by laser irradiations. The use of the laser (at enough high energy fluence) to induce the dewetting process, compared to a standard annealing process, allows the rapid fusion of the film and, consequently, the rapid solidification, obtaining an array of metal nanoparticles in chosen regions of the sample; in other words, it allows to pattern the surface only where the laser impacts and not on the whole sample.

1.3.2 Pulsed Laser Ablation in Liquid

The primary “eye-visible” effect of laser action on a solid target is removal of some material from the target surface within the laser spot. This process was called “laser ablation” from a Latin word *ablatio*, which means removal.

In the past two decades, with the rise of nanoscience, laser ablation has been broadly applied and developed for the synthesis of nanostructures. In particular, nanoparticles play an important role in many fields, as biotechnology, catalysis, medical and energy technology. But these applications require nanoparticles with specific surface activities, without residual chemical precursors and without any stabilizing ligands.

Pulsed Laser Ablation in Liquid (PLAL) has been proposed as a simple, versatile and green nanoparticles synthesis method, due to overcome many limitations of other fabrication methods. The experimental setup is very simple: laser radiation is used to ablate a solid target in a liquid environment, resulting in the formation of a nanoparticle colloid. More specifically, the laser beam is focused onto a solid-state material, using an appropriate optics, in a liquid medium. The energy provided by the laser pulse can be absorbed by the target and leads to the formation of an expanding plasma plume, containing the ablated material (figure 1.11). This is accompanied by the emission of a shockwave that releases energy in the surrounding liquid. When the plasma

cools down, it releases its heat to the liquid, which is transformed into hot vapor. This leads to the formation of an oscillating cavitation bubble containing both the ablated matter and the liquid vapor, where particles formation takes place. After the collapse of the cavitation bubble, another shockwave is generated and the particles are released into the solvent [78].

Nevertheless, the mechanisms involved in the nucleation and phase transition of nanocrystals during PLAL are not yet well understood. It has to be considered that quenching times in PLAL are so short that the metastable phases which form during the intermediate stage of the conversion can be frozen into this metastable state and form the synthesized final products [79].

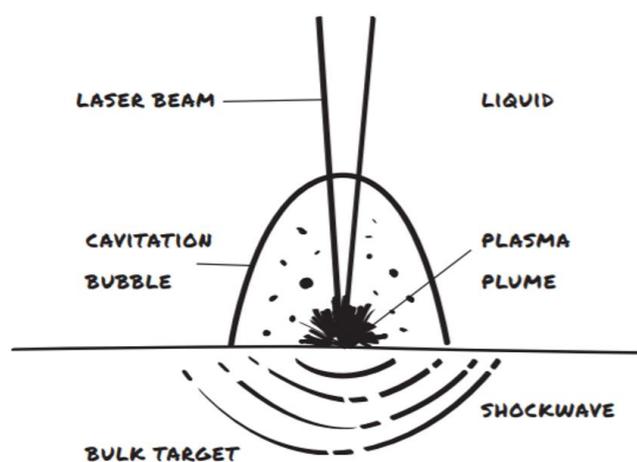


Figure 1.11 Schematic illustration of the pulsed laser ablation process in liquid [78].

Several parameters influence the properties of the obtained particles [64, 78,80]:

- a) *the laser fluence*: the fluence rules the productivity during laser ablation, determines the temperature reached of the target and is the main parameter to control particle size by pulsed laser melting in liquid;

- b) *repetition rate*: nanoparticles are ejected from the solid target at each pulse provided that the absorbed laser energy is sufficient to melt the target. Therefore, the higher is the repetition rate of laser pulses, the higher is the rate of generation of NPs;
- c) *the beam wavelength*: it is mostly established to use the fundamental wavelength of 800-1064 nm for laser ablation in liquids, but also green light with 532 nm is often used. But, in the last case, laser radiation can be absorbed by NPs that are generated and the ablation of the target and the re-irradiation of the NPs take place simultaneously;
- d) *the duration of the laser pulse (t_p)*: it is proportionate to the heat diffusion length (h): $h \propto (at_p)^{1/2}$, where $a=k/c\rho$, where k is the heat conduction coefficient of the target. The longer is the laser pulse duration t_p , the thicker is the layer of the material that is heated by absorbed laser energy;
- e) *the solvent*: the liquid environment influences the nature of the resulting nanoparticles; it has to be transparent (or with small absorption coefficient) at laser wavelength, in order to prevent absorption of laser light. In addition, some solvents (such as toluene and acetone) lead to formation of a thin carbon layer on the particle's surface, which results in the interruption of nucleation and hindering of the growth of nanoparticles, determining the fabrication of smaller nanoparticles.

Laser ablation is a physical process that is fundamentally different from chemical nanoparticle synthesis routes. The nanoparticles produced by PLAL are characterized by the following potential advantages:

1. *Versatility*: compared to common chemical reduction or precipitation routes which rely on the availability of the respective precursors, this physico-chemical laser ablation method allows the production of NPs from any base material (metal, alloy, semiconductor, ceramic) and in numerous liquids environments. Indeed, depending on experimental parameters not only pure materials such as metallic or oxide nanoparticles, but also alloy or core-shell nanoparticles are produced;

2. *Availability* of target: the solid material for laser-based nanoparticle production is easily available and often 5 to 10 times cheaper than commonly used metal-organic precursor compounds;
3. *Purity*: highly pure colloids are produced with this method. In fact, very important is, with respect to the most used chemical methods, its independence from chemical precursors (such as metal-organic substances), from the use of toxic substances or reducing agents and free of chemical stabilizers. The last point appears to be determinant for the application of NPs in biomedical or biological applications, where chemical agents can be harmful and reduce cell viability after NP treatment; moreover, the absence of ligands on the particle surface enhances the possibility of their functionalization with biomolecules, making them very effective as biomarkers or for targeted cell therapies [81,82]. Furthermore, the bare surface of NPs is very attractive for all the applications exploiting their chemical properties, as for example catalysis purposes.

1.3.3. Pulsed Laser Deposition

In 1965, for the first time, lasers have been used in thin film deposition experiments when H.M Smith and A.F Turner ablated material from a target in a low pressure chamber, by using a ruby laser, but the thin films were not perfectly uniform in thickness and did not adhere to the substrate [79].

Pulsed laser deposition (PLD) is a growth technique in which the photon energy of a laser, characterized by pulse duration and laser frequency, interacts with a bulk material [84,85]. As a result, material is removed from the bulk depending on the absorption properties of the target materials. The working principle of PLD is sketched in figure 1.12.a: in ultrahigh vacuum or in the presence of a background gas, the focused laser pulses are absorbed at the target surface. The absorbed energy density is sufficient to break any chemical bonds of the molecules within that volume, producing an expansion of hot plasma (plume) through the deposition chamber (fig. 1.12.b). The ablated species condense on the substrate placed opposite to the target forming a thin film after some hundreds or thousands of laser pulses [86]. The growth

kinetic of such films depends on the material flux, repetition rate, growth temperature, substrate material, pressure and background gas (vacuum, reactive).

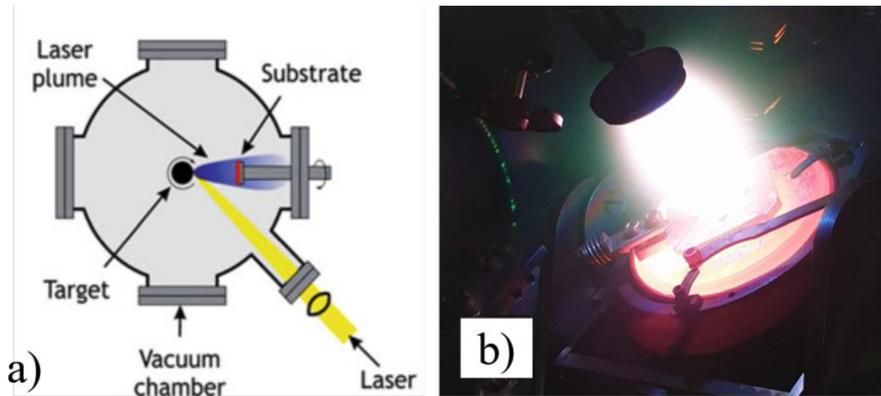


Figure 1.12 Schematic of pulsed laser deposition. The incoming laser beam is focused onto a target, thereby vaporizing the material of the surface. The ejected material is partially ionized and forms the ablation plume which is directed towards the substrate [60] (a). Photograph of the PLD process (b).

To use PLD for thin film growth has advantages for a number of reasons [60,87]:

1. The flexibility in wavelength and power density allows to ablate almost any material or materials combination, growing thin films with high crystalline quality, including ceramic oxides, nitrides, metallic multilayers, and various superlattices, as well as polycrystalline or single-crystal films with different textures; preserving the capability for stoichiometric transfer of material from target to substrate;
2. The laser is not part of the vacuum system. Therefore, a considerable degree of freedom in the ablation geometry is possible;
3. The use of a pulsed laser beam enables a precise control over the growth rate (direct relation number of pulses-thickness);
4. The congruent transfer of the composition can be achieved for most ablated material or materials combinations;

5. The use of a carousel, housing a number of target materials, enables multilayer films to be deposited without the need to break vacuum when changing between materials;
6. Relatively high deposition rates can be achieved at moderate laser fluences, with film thickness controlled in real time by simply turning the laser on and off;
7. Compared with other methods, PLD demonstrates relatively lower costs than, e.g., MBE and MOCVD, but generally allows the preparation of films with higher crystalline quality than most of the other methods.

Epitaxial growth of a material require an appropriate substrate material, indeed, basic requirements are a good crystallographic lattice match between film and substrate, the substrate material should be chemically compatible to the film, it should have comparable thermal expansion coefficients, and a thermodynamically and chemically stable surface. When species of the plume arrive at a substrate surface, the first arriving pulse causes the nucleation of a high density of smaller clusters. These subcritical clusters tend to dissociate into mobile species that will nucleate new clusters of a different size during the time of no vapor arrival. The next pulse will initiate the same process again, with the difference that some of the mobile atoms will reach the previous formed clusters [60].

The substrate temperature is important to ensure a sufficient surface mobility of the arriving species to support epitaxial growth.

To obtain the correct film composition, the background pressure and gas is another parameter which needs to be controlled. For most oxides, an oxygen atmosphere is necessary for the correct oxygen content in a film. While, some materials require a reducing atmosphere [68,88].

Chapter 1 References

1. R. P. Feynman, (1960) There's Plenty of Room at the Bottom. *Engineering and Science*, 23 (1960) 22-36. ISSN 0013-7812 <http://resolver.caltech.edu/CaltechES:23.5.1960Bottom>
2. J. Jeevanandam, A. Barhoum, Y. S. Chan, A. Dufresne, M. K. Danquah, Review on nanoparticles and nanostructured materials: history, sources, toxicity and regulations, *Beilstein J. Nanotechnol.*, 9 (2018) 1050–1074. doi:10.3762/bjnano.9.98
3. M. Ramrakhiani, Nanostructures and their applications, *Recent Research in Science and Technology*, 4 (2012) 14-19. <https://updatepublishing.com/journal/index.php/rrst/article/view/910>
4. N. Chouhan, Silver Nanoparticles-Fabrication, Characterization and Applications, Edited by Khan Maaz (2018). <http://dx.doi.org/10.5772/intechopen.75611>
5. H. Gleiter, Nanostructured materials: basic concepts and microstructure *Acta Mater.*, 48 (2000) 1–29. doi:10.1016/S1359-6454(99)00285-2
6. J. N. Tiwari, R. N. Tiwari, K. S. Kim, Zero-dimensional, one-dimensional, two-dimensional and three-dimensional nanostructured materials for advanced electrochemical energy devices, *Prog. Mater. Sci.*, 57 (2012) 724–803. doi:10.1016/j.pmatsci.2011.08.003
7. V. V. Pokropivny, V. V. Skorokhod, Classification of nanostructures by dimensionality and concept of surface forms engineering in nanomaterial science *Mater. Sci. Eng., C*, 27 (2007) 990–993. doi:10.1016/j.msec.2006.09.023
8. M. Censabella, V. Torrisi, S. Boninelli, C. Bongiorno, M. G. Grimaldi, F. Ruffino, Laser ablation synthesis of mono- and bimetallic Pt and Pd nanoparticles and fabrication of Pt-Pd/Graphene nanocomposites, 475 (2019) 494-503. <https://doi.org/10.1016/j.apsusc.2019.01.029>
9. W. P. McConnell, J. P. Novak, L. C. Brousseau, R. R. Fuierer, R. C. Tenent, D. L. Feldheim, Electronic and optical properties of chemically modified metal nanoparticles and molecularly bridged nanoparticle

- arrays, *The Journal of Physical Chemistry B.*, 104 (2000): 8925-8930. DOI: 10.1021/jp000926t
10. C. P. Collier, R. J. Saykally, J. J. Shiang, S. E. Henrichs, J. R. Heath, Reversible tuning of silver quantum dot monolayers through the metal-insulator transition, *Science*, 277 (1997) 1978-1981. DOI: 10.1126/science.277.5334.1978
 11. M. De, P. S. Ghosh, V. M. Rotello, Applications of nanoparticles in biology, *Advanced Materials*, 20 (2008) 4225-4241. DOI: 10.1002/adma.200703183
 12. A. H. Lu, E. E. Salabas, F. Schüth, Magnetic nanoparticles: Synthesis, protection, functionalization and application, *Angewandte Chemie International Edition*. 2007; 46(8):1222- 1244. DOI: 10.1002/anie.200602866
 13. R. Ghosh Chaudhuri, S. Paria S., Core/shell nanoparticles: Classes, properties, synthesis mechanisms, characterization and applications, *Chemical Reviews*, 112 (2011) 2373-2433. DOI: 10.1021/cr100449n
 14. D. R. Monteiro, L. F. Gorup, A. S. Takamiya, A. C. Ruvollo-Filho, E. R. de Camargo, D. B. Barbosa, The growing importance of materials that prevent microbial adhesion: Antimicrobial effect of medical devices containing silver, *International Journal of Antimicrobial Agents*, 34 (2009) 103-110. DOI: 10.1016/j.ijantimicag.2009.01.017
 15. R.L. Johnston, J.P. Wilcoxon, *Metal Nanoparticles and Nanoalloys*, first ed., Elsevier, Amsterdam, 2012.
 16. S.A. Maier, *Plasmonics: Fundamentals and Applications*, Springer, New York, 2007.
 17. G. Sharma, A. Kumar, S. Sharma, M. Naushad, R.P. Dwivedi, Z.A. Alothman, G.T. Mola, Novel development of nanoparticles to bimetallic nanoparticles and their composites: a review, *J. King Saud Univ.-Sci.* (2017) (in press). 10.1016/j.jksus. 2017.06.012.
 18. F. Mafunè, J. Kohno, Y. Takeda, T. Kondow, Formation of stable platinum nanoparticles by laser ablation in water, *J. Phys. Chem. B* 107 (2003) 4218–4223. <https://pubs.acs.org/doi/abs/10.1021/jp021580k>.
 19. A. Rostek, M. Breisch, K. Pappert, K. Loza, M. Heggen, M. Köller, C. Sengstock, M. Epple, Comparative biological effects of spherical noble

- metal nanoparticles (Rh, Pd, Ag, Pt, Au) with 4–8 nm diameter, Beilstein J. Nanotechnol., 9 (2018) 2763–2774. doi:10.3762/bjnano.9.258
20. Homberger, M.; Simon, U. Philos. Trans. R. Soc. London, A 2010, 368, 1405–1453. doi:10.1098/rsta.2009.0275
 21. Jain, P. K.; Huang, X.; El-Sayed, I. H.; El-Sayed, M. A. Acc. Chem. Res. 2008, 41, 1578–1586. doi:10.1021/ar7002804
 22. Li, J.; Zhao, T.; Chen, T.; Liu, Y.; Ong, C. N.; Xie, J. Nanoscale 2015, 7, 7502–7519. doi:10.1039/c5nr00857c
 23. Liu, H.-l.; Nosheen, F.; Wang, X. Chem. Soc. Rev. 2015, 44, 3056–3078. doi:10.1039/c4cs00478g
 24. B.D. Adams, A. Chen, The role of palladium in a hydrogen economy, Mater. Today 14 (2011) 282–289, [https://doi.org/10.1016/S1369-7021\(11\)70143-2](https://doi.org/10.1016/S1369-7021(11)70143-2).
 25. S.K. Konda, A. Chen, Palladium based nanomaterials for enhanced hydrogen spillover and storage, Mater. Today 19 (2016) 100–108, <https://doi.org/10.1016/j.mattod.2015.08.002>.
 26. C. Zhou, J.A. Szpunar, Hydrogen storage performance in Pd/Graphene nanocomposites, ACS Appl. Mater. Interf. 8 (2016) 25933–25940 <https://pubs.acs.org/doi/abs/10.1021/acsami.6b07122>
 27. M. Censabella, F. Ruffino, M. Zimbone, E. Bruno, M. G. Grimaldi, Self-Organization Based Fabrication of Bimetallic PtPd Nanoparticles on Transparent Conductive Oxide Substrates, Phys. Status Solidi A, 215 (2017) 1700524–1700524. <https://doi.org/10.1002/pssa.201700524>
 28. M. Yamauchi, H. Kobayashi, H. Kitagawa, Hydrogen Storage Mediated by Pd and Pt Nanoparticles, Chem. Phys. Chem., 10 (2009) 2566 – 2576. <https://doi.org/10.1002/cphc.200900289>
 29. N. G. Semaltianos, P. Petkov, S. Scholz, L. Guetaz, Palladium or palladium hydride nanoparticles synthesized by laser ablation of a bulk palladium target in liquids., J. Colloid Interface Sci., 402 (2013) 307–311. doi: 10.1016/j.jcis.2013.03.062
 30. R. Esparza, A. Santovena, A. Ruiz-Baltazar, A. Angeles-Pascual, J. Maya-Cornejo, J. Ledesma-Garcia, R. Perez, Study of PtPd Bimetallic Nanoparticles for Fuel Cell Applications, Mater. Res. 20 (2017) 1193–1200. <http://dx.doi.org/10.1590/1980-5373-mr-2016-0934>

31. R. Esparza, A. F. Garzia-Ruiz, J. J. Velázquez Salazar, R. Pérez, M. J. Yacamàn, Structural characterization of Pt-Pd core-shell nanoparticles by Cs-corrected STEM, *J. Nanopart. Res.*, 15 (2012) 1342, <https://doi.org/10.1007/s11051-012-1342-2>
32. J. Liu, S. D. Zou, L. Xiao, J. Fan, Well-dispersed bimetallic nanoparticles confined in mesoporous metal oxides and their optimized catalytic activity for nitrobenzene hydrogenation, *Catal. Sci. Technol.* 4 (2014) 441–446. DOI: 10.1039/C3CY00689A
33. X. Yang, Q. Yang, J. Xu, C. S. Lee, Bimetallic PtPd nanoparticles on Nafion–graphene film as catalyst for ethanol electro-oxidation, *J. Mater. Chem.*, 22 (2012) 8057. DOI: 10.1039/C2JM16916A
34. G. D. P. Rose, *Fossili Novo. In De Novis Quibusdam Fossilibus Quae in Montibus Uraliis Inveniuntur*; AG Schade: Berlin, Germany, 1839.
35. E. A. R. Assirey, Perovskite synthesis, properties and their related biochemical and industrial application, *Saudi Pharmaceutical Journal*, 27 (2019) 817–829. <https://doi.org/10.1016/j.jsps.2019.05.003>
36. E. C. C. de Souza, R. Muccillo, Properties and Applications of Perovskite Proton Conductors, *Materials Research*, 13 (2010) 385-394. <http://dx.doi.org/10.1590/S1516-14392010000300018>
37. P. Fu, Q. Shan, Y. Shang, J. Song, H. Zeng, Z. Ning, J. Gong, Perovskite nanocrystals: synthesis, properties and applications, *Sci. Bull.*, 62 (2017) 369–380. <https://doi.org/10.1016/j.scib.2017.01.006>
38. L. Protesescu, S. Yakunin, M. I. Bodnarchuk, F. Krieg, R. Caputo, C. H. Hendon, R. X. Yang, A. Walsh, M. V. Kovalenko, Nanocrystals of cesium lead halide perovskites (CsPbX₃, X= Cl, Br, and I): novel optoelectronic materials showing bright emission with wide color gamut, *Nano Lett.*, 15 (2015) 3692–3696. <https://doi.org/10.1021/nl5048779>
39. E. Nenasheva, A. Kanareykin, N. Kartenko, A. Dedyk, S. Karmanenko, Ceramics materials based on (Ba, Sr)TiO₃ solid solutions for tunable microwave devices, *J. Electroceram.*, 13 (2004) 235–238. <https://doi.org/10.1007/s10832-004-5104-0>
40. P. Muralt, R. Polcawich, S. Trolier-McKinstry, Piezoelectric thin films for sensors, actuators, and energy harvesting, *MRS Bull.*, 34 (2009) 658–664. <https://doi.org/10.1557/mrs2009.177>

41. Y. Kawamura, H. Mashiyama, K. Hasebe, K., Structural study on cubic–tetragonal transition of $\text{CH}_3\text{NH}_3\text{PbI}_3$, *J. Phys. Soc. Jpn*, 71 (2002) 1694–1697. <https://doi.org/10.1143/JPSJ.71.1694>
42. N. F. Atta, A. Galal, E. H. El-Ads, Perovskite nanomaterials-synthesis, characterization, and applications, *Tech. Chapter 4*, (2006) 108–151. DOI: 10.5772/61280.
43. E. Fabbri, D. Pergolesi, E. Traversa, Materials challenges toward proton-conducting oxide fuel cells: a critical review, *Chem. Soc. Rev.*, 39 (2010) 4355-4369. DOI: 10.1039/B902343G
44. A. S. Nowick, Y. Du, High-temperature protonic conductors with perovskite-related structures, *Solid State Ionics*, 77 (1995) 137–146. [https://doi.org/10.1016/0167-2738\(94\)00230-P](https://doi.org/10.1016/0167-2738(94)00230-P)
45. K. Katahira, Y. Kohchi, T. Shimura and H. Iwahara, Protonic conduction in Zr-substituted BaCeO_3 , *Solid State Ionics*, 138 (2000) 91–98. [https://doi.org/10.1016/S0167-2738\(00\)00777-3](https://doi.org/10.1016/S0167-2738(00)00777-3)
46. N. Zakowsky, S. Williamson, J. T. S. Irvine, Elaboration of CO_2 tolerance limits of $\text{BaCe}_{0.9}\text{Y}_{0.1}\text{O}_{3-\delta}$ electrolytes for fuel cells and other applications, *Solid State Ionics*, 176 (2005) 3019-3026. <https://doi.org/10.1016/j.ssi.2005.09.040>
47. K. D. Kreuer, Proton-Conducting Oxides, *Annu. Rev. Mater. Res.*, 33 (2003) 333–359. <https://doi.org/10.1146/annurev.matsci.33.022802.091825>
48. A. D’Epifanio, E. Fabbri, E. Di Bartolomeo, S. Licoccia, E. Traversa, Design of $\text{BaZr}_{0.8}\text{Y}_{0.2}\text{O}_{3-\delta}$ Protonic Conductor to Improve the Electrochemical Performance in Intermediate Temperature Solid Oxide Fuel Cells (IT-SOFCs), *Fuel Cells*, 8 (2008) 69–76. <https://doi.org/10.1002/fuce.200700045>
49. K. D. Kreuer, S. Adams, W. Munch, A. Fuchs, U. Klock, J. Maier, Proton conducting alkaline earth zirconates and titanates for high drain electrochemical applications, *Solid State Ionics*, 145 (2001) 295-306. [https://doi.org/10.1016/S0167-2738\(01\)00953-5](https://doi.org/10.1016/S0167-2738(01)00953-5)
50. C. I. Ossai, N. Raghavan, Nanostructure and nanomaterial characterization, growth mechanisms, and applications, *Nanotechnol Rev*, 7 (2018) 209–231. DOI: <https://doi.org/10.1515/ntrev-2017-0156>

51. X. Huang, Z. Zeng, S. Bao, M. Wang, X. Qi, Z. Fan, H. Zhang, Solution-phase epitaxial growth of noble metal nanostructures on dispersible single-layer molybdenum disulfide nanosheets, *Nat. Commun.*, 4 (2013) 1444. doi: 10.1038/ncomms2472
52. Y. C. Kong, D. P. Yu, B. Zhang, W. Fang, S. Q. Feng, Ultraviolet-emitting ZnO nanowires synthesized by a physical vapor deposition approach, *Appl. Phys. Lett.*, 78 (2001) 407–409. <https://doi.org/10.1063/1.1342050>.
53. R. Dolbec, M. A. El Khakani, A. M. Serventi, M. M. Trudeau, R. G. Saint-Jacques, Microstructure and physical properties of nanostructured tin oxide thin films grown by means of pulsed laser deposition, *Thin Solid Films*, 419 (2002) 230–236. DOI: 10.1016/S0040-6090(02)00769-1
54. J. L. Yang, S. J. An, W. I. Park, G. C. Yi, W. Choi, Photocatalysis using ZnO thin films and nanoneedles grown by metal-organic chemical vapor deposition, *Adv. Mater.*, 16 (2004) 1661–1664. <https://doi.org/10.1002/adma.200306673>
55. M. Yoshizawa, A. Kikuchi, M. Mori, N. Fujita, K. Kishino, Growth of self-organized GaN nanostructures on Al₂O₃ (0001) by RF-radical source molecular beam epitaxy, *Jpn. J. Appl. Phys.*, 36 (1997) L459. <https://doi.org/10.1143/JJAP.36.L459>
56. H. Söderberg, M. Odén, J. M. Molina-Aldareguia, L. Hultman, Nanostructure formation during deposition of TiN/SiN {sub x} nanomultilayer films by reactive dual magnetron sputtering, *J. Appl. Phys.*, 97 (2005) 11432. <https://doi.org/10.1063/1.1935135>
57. M. Bognitzki, W. Czado, T. Frese, A. Schaper, M. Hellwig, M. Steinhart, A. Greiner, J. H. Wendorff, Nanostructured fibers via electrospinning, *Adv. Mater.*, 13 (2001) 70–72. [https://doi.org/10.1002/1521-4095\(200101\)13:1<70::AID-ADMA70>3.0.CO;2-H](https://doi.org/10.1002/1521-4095(200101)13:1<70::AID-ADMA70>3.0.CO;2-H)
58. S. Xu, Z. L. Wang, One-dimensional ZnO nanostructures: solution growth and functional properties, *Nano Res.*, 4 (2011) 1013–1098. <https://doi.org/10.1007/s12274-011-0160-7>
59. F. Zhang, H. Yang, X. Xie, L. Li, L. Zhang, J. Yu, H. Zhao, B. Li, Controlled synthesis and gas-sensing properties of hollow sea urchin-like

- α -Fe₂O₃ nanostructures and α -Fe₂O₃ nanocubes, *Sens. Actuators B Chem.*, 141 (2009) 381–389. DOI: 10.1016/j.snb.2009.06.049
60. P. Schaaf, *Laser Processing of Materials: Fundamentals, Applications and Developments*, Springer Series in Materials Science, 2010. DOI 10.1007/978-3-642-13281-0
 61. T. H. Maiman, Stimulated Optical Radiation in Ruby, *Nature*, 187 (1960) 493–494. <https://doi.org/10.1038/187493a0>
 62. M. Hashida, H. Mishima, S. Tokita, S. Sakabe, Non-thermal ablation of expanded polytetrafluoroethylene with an intense femtosecond-pulse laser, *Opt. Express*, 17 (2009) 13116–13121. <https://doi.org/10.1364/OE.17.013116>
 63. S. Chakraborty, H. Sakata, E. Yokoyama, M. Wakaki, D. Chakravorty, Laser-induced forward transfer technique for maskless patterning of amorphous V₂O₅ thin film, *Appl. Surf. Sci.*, 254 (2007) 638. <https://doi.org/10.1016/j.apsusc.2007.06.066>
 64. H. Zeng, X. Du, S. C. Singh, S. A. Kulinich, S. Yang, J. He, W. Cai, Nanomaterials via Laser Ablation/Irradiation in Liquid: A Review, *Adv. Funct. Mater.*, 22 (2012) 1333–1353. doi:10.1002/adfm.201102295
 65. V. P. Veiko, V. I. Konov, *Fundamentals of Laser-Assisted Micro- and Nanotechnologies*, Springer: New York, NY, USA, 2014.
 66. S. C. Singh, H. B. Zeng, C. Guo, W. P. Cai, *Nanomaterials-Processing and Characterization with Lasers*, Wiley: Weinheim, Germany, 2012.
 67. K. Sugioka, Y. Cheng, *Ultrafast Laser Processing-From Micro- to Nanoscale*, CRC Press: Boca Raton, FL, USA, 2013.
 68. D. von der Linde, K. Sokolowski-Tinten, The physical mechanisms of short-pulse laser ablation, *Appl. Surf. Sci.*, 1 (2000) 154–155. [https://doi.org/10.1016/S0169-4332\(99\)00440-7](https://doi.org/10.1016/S0169-4332(99)00440-7)
 69. C. V. Thompson, Solid-State Dewetting of Thin Films, *Annu. Rev. Mater. Res.*, 42 (2102) 399–434. <https://doi.org/10.1146/annurev-matsci-070511-155048>
 70. S. Herminghaus, M. Brinkmann, R. Seemann, Wetting and Dewetting of Complex Surface Geometries *Annu. Rev. Mater. Res.* 38 (2008) 101–121. <https://doi.org/10.1146/annurev.matsci.38.060407.130335>

71. D. Bonn, J. Eggers, J. Indekeu, J. Meunier, E. Rolley, Wetting and spreading, *Rev. Mod. Phys.* 81(2009) 739. <https://doi.org/10.1103/RevModPhys.81.739>
72. P. G. de Gennes, Wetting: statics and dynamics, *Rev. Mod. Phys.* 57 (1985) 827 <https://doi.org/10.1103/RevModPhys.57.827>
73. L. Leger, J. F. Joanny, Liquid spreading, *Rep. Prog. Phys.* 55 (1992) 431. <https://doi.org/10.1088/0034-4885/55/4/001>
74. M. Geoghegan, G. Krausch, Wetting at polymer surfaces and interfaces, *Prog. Polym. Sci.*, 28 (2003) 261. [https://doi.org/10.1016/S0079-6700\(02\)00080-1S](https://doi.org/10.1016/S0079-6700(02)00080-1S).
75. F. Ruffino, M. G. Grimaldi, Controlled dewetting as fabrication and patterning strategy for metal nanostructures, *Phys. Stat. Sol. A*, 212 (2015) 1662-1684. <https://doi.org/10.1002/pssa.201570453>
76. M. Censabella, F. Ruffino, M. Zimbone, E. Bruno, M. G. Grimaldi, Self-Organization Based Fabrication of Bimetallic PtPd Nanoparticles on Transparent Conductive Oxide Substrates, *Phys. Status Solidi A*, 215 (2017) 1700524-1700524. <https://doi.org/10.1002/pssa.201700524>
77. J. Trice, D. Thomas, C. Favazza, R. Sureshkumar, R. Kalyanaraman, Pulsed-laser induced dewetting in nanoscopic metal films: theory and experiments, *Phys. Rev. B*, 75 (2007) 235439. DOI:<https://doi.org/10.1103/PhysRevB.75.235439>
78. Barcikowski, V. Amendola, G. Marzun, C. Rehbock, S. Reichenberger, D. Zhang, B. Gokce, *Handbook of laser synthesis of colloids*, DuEPublico, 2016.
79. S. Barcikowski, G. Compagnini, Advanced nanoparticle generation and excitation by lasers in liquids, *Phys. Chem. Chem. Phys.*, 15 (2013) 3022-3026. DOI: 10.1039/C2CP90132C
80. G. Yang, *Laser Ablation in Liquids: Principles and Applications in the Preparation of Nanomaterials*, Pan Stanford Publishing Pte. Ltd 2012.
81. U. Taylor, S. Klein, S. Petersen, W. Kues, S. Barcikowski, D. Rath, Nonendosomal cellular uptake of ligand-free, positively charged gold nanoparticles, *Cytometry, Part A*, 77A (2010) 439–446. DOI: 10.1002/cyto.a.20846
82. G. Cristoforetti, E. Pitzalis, R. Spiniello, R. Ishak, M. M. Miranda, Production of Palladium Nanoparticles by Pulsed Laser Ablation in

- Water and Their characterization, *J. Phys. Chem. C.* 115 (2011) 5073-5083. <https://pubs.acs.org/doi/abs/10.1021/jp109281q>
83. H. M. Smith, A. F. Turner, Vacuum Deposited Thin Films Using a Ruby Laser, *Appl. Opt.*, 4 (1965) 147-148. <https://doi.org/10.1364/AO.4.000147>
84. D. Chrisey, G.K. Hubler, Pulsed Laser Deposition of Thin Films, vol. 154–155, Wiley, New York 1994.
85. X. Yang, Y. Tang, M. Yu, Q. Qin, Pulsed laser deposition of aluminum tris-8-hydroxyquinoline thin films, *Thin Solid Films*, 358 (2000) 187-190. [https://doi.org/10.1016/S0040-6090\(99\)00687-2](https://doi.org/10.1016/S0040-6090(99)00687-2)
86. E. Morintale, C. Constantinescu, M. Dinescu, Thin films development by pulsed laser-assisted deposition, *Annals of the University of Craiova*, 2010, Physics 20 (1), 2010, 43-56.
87. D. B. Chrisey, G. K. Hubler, Pulsed Laser Deposition of Thin Films, John Wiley & Sons, Weinheim 1994.
88. R.R. Gattass, E. Mazur, Femtosecond laser micromachining in transparent materials, *Nat. Photonics*, 2 (2008) 219-225. <https://doi.org/10.1038/nphoton.2008.47>

Chapter 2

Mono- and bimetallic nanoparticles produced by Laser Irradiations of thin films deposited on Transparent Conductive Oxides

In the previous chapter, the excellent properties of monometallic (Pt and Pd) and bimetallic PtPd NPs have been widely illustrated. However, a critical issue is the formation of NPs with a desired size that should take place directly on a support. Hence, for the exploitation of these nanostructures in real devices, the design of simple, cost-effective, versatile, high-throughput fabrication methods on suitable supporting surfaces, allowing desired NPs size and shape control, is of paramount importance [1]. Obviously, the detailed understanding of the basic microscopic mechanisms governing the involved process is crucial in assuring the desired NPs control.

Some of the work described in this chapter has been previously published as:

¹ M. Censabella, F. Ruffino, M. Zimbone, E. Bruno, M. G. Grimaldi, *Self-Organization Based Fabrication of Bimetallic PtPd Nanoparticles on Transparent Conductive Oxide Substrates*, *Phys. Status Solidi A*, 215 (2017) 1700524-1700524. <https://doi.org/10.1002/pssa.201700524>

² V. Torrisi, M. Censabella, G. Piccitto, G. Compagnini, M. G. Grimaldi, F. Ruffino, *Characteristics of Pd and Pt Nanoparticles Produced by Nanosecond Laser Irradiations of Thin Films Deposited on Topographically-Structured Transparent Conductive Oxides*, *Coatings*, 8 (2018) 68. <https://doi.org/10.3390/coatings9020068>

Taking into account this analysis, in the present chapter I describe on the exploitation of a laser-based approach to fabricate monometallic and bimetallic Pd and Pt NPs supported on a functional surface. The approach is based on the sputtering deposition of nanoscale-thick Pd or Pt films onto the surface of a Fluorine-doped Tin Oxide ($\text{SnO}_2\text{:F}$) layer on glass (soda-lime), i.e. FTO/glass substrate. Then, nanosecond laser irradiations ($\lambda = 532 \text{ nm}$) were carried on the metallic films surface so to exploit the potentialities of the laser-matter interaction for surface nanostructuring [2-12].

2.1 Fluorine doped Tin Oxide (FTO)

Transparent conducting oxides (TCOs) have attracted considerable attention because of their high electronic conduction and optical transparency. These thin films are an important component in a number of electronic devices, such as OLEDs (Organic Light-Emitting Diodes), liquid-crystal displays, touchscreens and photovoltaics. Between TCOs most common are Indium Tin Oxide (ITO) and Fluorine doped Tin Oxide (FTO). In particular FTO, is a TCO which use is largely diffused as coating in solar cell heat mirror for its high electrical conductivity and high transparency at visible and near-IR region of the electromagnetic spectrum or for photoelectrochemical reactions on surface [13-18].

In our case, FTO/glass (soda-lime) slides, purchased from KINTEC factory [18], were the starting substrates. The electrical and optical characterizations of these substrates have been done by Gentile et al. [16]. Moreover, they also measured the effect produced, on the FTO substrate, by a thermal process at $500 \text{ }^\circ\text{C}$ _3h and by laser irradiation ($\lambda=532 \text{ nm}$) at high fluence (1 J/cm^2). The transmittance spectra (T%) in the range from 330 to 1100 nm are shown in figure 2.1.a. The transmittance does not vary significantly after the thermal treatments (laser and furnace). Indeed, it varies within 20 % (likely modification in the FTO refractive index) and the transmittance values after the thermal processes range in the same interval. The spectrum oscillations are due to the interference phenomena at glass/FTO interface. In addition, the values of the glass/FTO sheet resistances before ($R_s=8.6\Omega/\text{sq}$) and after

thermal treatments are reported in figure 2.1.b. In particular, the electrical characterization highlights an alteration of the FTO/glass electrical properties as a consequence of furnace thermal treatment at 500°C_3h ($R_{s_500\text{ }^\circ\text{C}} = 22.9\ \Omega/\text{sq}$). While, the laser irradiation of the FTO substrates does not produce significant differences to electrical properties ($R_{s_laser} = 8.4\ \Omega/\text{sq}$) [16].

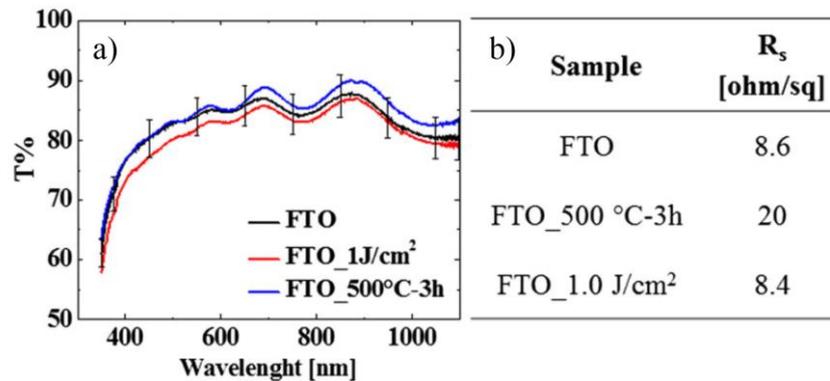


Figure 2.1 Transmittance spectra (T%) in the visible range related to FTO/glass substrate (black line), the substrate after thermal process at 500 °C_3h (blue line) and the substrate after laser annealing at 1 J/cm² (red line) a). In Table are reported the values of the sheet resistance related to substrate before and after thermal treatments b) [16].

Therefore, the FTO lends itself well to being used as a substrate for our work being transparent to the used wavelength ($\lambda = 532\ \text{nm}$) and not modified (regarding the electrical and optical properties) by the laser processing [15-16].

Figure 2.2 reports a Scanning Electron Microscopy (SEM) image of the bare FTO surface used as substrate. It appears that the FTO layer on the glass substrate has a complex non-flat topography. Indeed, by the inspection of this plan-view image, the FTO layer results to be formed by micrometric structures having, about, a truncated-pyramidal shape and which, randomly arranged, cover the entire surface of the glass slide. We point out that this is the standard morphology for deposited FTO layers [20,21] and that it is desired in several applications (solar cells, etc.) due to its ability in efficiently scatter light [15-

17, 21]. A mean value for FTO roughness, calculated with Atomic Force Microscopy (AFM), is $\sigma_{FTO} = 32.7 \pm 8.7 \text{ nm}$ [16].

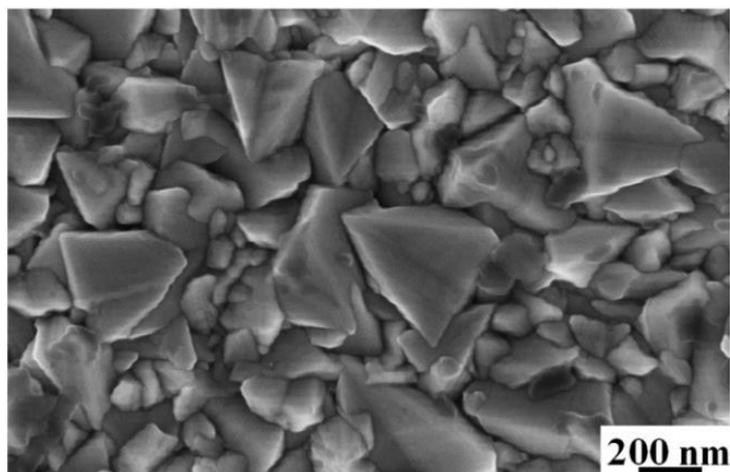


Figure 2.2 FTO bare surface as imaged by SEM. The surface structuration in pyramidal-like structures is recognizable.

2.2 Bimetallic PtPd NPs produced by nanosecond laser irradiation on topographically-structured FTO

It is known in literature that bimetallic nanoparticles improved the properties of monometallic ones due to synergistic effects between the two elements [22]. In particular, in the field of catalysis, bimetallic NPs show superior catalytic properties than their monometallic counterparts [23,24] and for hydrogen storage applications, the amount of hydrogen absorption of PdPt NPs was found to be greater than that of the single components [25]. Nevertheless, there is no scientific papers, at present, in which bimetallic PtPd nanoparticles are produced through simple laser based technique on surface. In the same way, there is not literature for Pd NPs, while Pt nanoparticles are produced by laser irradiation, on a flat surface, by Zhou et al. [26].

For this reason, I have chosen to focus our attention on PtPd bimetallic particles and in this section I present a method for the controlled production of bimetallic PtPd NPs directly on FTO by nanosecond laser irradiation.

In detail, I deposited, by sequential sputter depositions, thin Pd/Pt bilayers on FTO substrate with thickness h_{Pd} and h_{Pt} of the Pd and Pt layers. Then, I induced the melting, alloying and dewetting processes of the films by the nanosecond laser irradiations.

2.2.1 Experimental section

The samples were prepared starting from the glass/FTO slides. For each metal deposition, some glass/FTO slides were inserted within the vacuum chamber of a RF Emitech K550X sputter coater. In addition, Si slides were introduced with the glass/FTO slide; they served as reference samples for successive check of the effective thickness of the deposited metal films. Pd or Pt films were sputter-deposited onto the FTO surface clamping the substrates against the cathode located straight in front of the source (99.999% purity target). The electrodes were laid at a distance of 40mm under Ar flow, keeping a pressure of 0.02 mbar in the chamber. The resulting thickness h of the films was tuned by the control of the emission current and deposition time and it was checked, after the depositions, by Rutherford Backscattering Spectrometry (RBS) analysis indicating a 5% error in h . These analyses (RBS 2.0 MeV He⁺ beam) were performed by using a 3.5 MV HVEEE Singletron accelerator system, with normal incidence and detection modes (165° backscattering angle). The beam spot is circular, 1 mm in diameter. RBS spectra were analyzed using XRump software.

Two sets of samples were prepared, labeled set A and B, which differ for the different Pd and Pt layers' sequences. Each set consists of three samples with different film thickness, see Tables 2.1 and 2.2 and the schematic representation in figure 2.3.

Table 2.1 Thickness and sequence of the Pt and Pd layers deposited on FTO substrate for the samples A.

Sample A	Layer 1: Pt (nm)	Layer 2: Pd (nm)
A1	3	4
A2	9	4
A3	8	8

Table 2.2 Thickness and sequence of the Pd and Pt layers deposited on FTO substrate for the samples B.

Sample B	Layer 1: Pd (nm)	Layer 2: Pt (nm)
B1	4	3
B2	4	9
B3	8	8

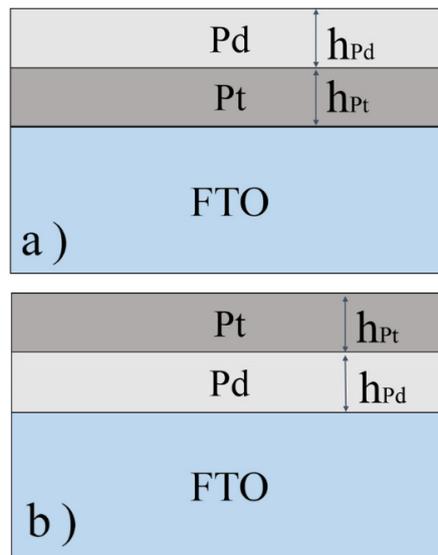


Figura 2.3 Schematic representation of the samples A (a) and samples B (b), which present opposite sequence of the bilayers compared to samples A [22].

Laser irradiations were performed by pulsed (10 ns) Nd:YAG laser (neodymium-doped yttrium aluminum garnet, Quanta-ray PRO-Series pulsed Nd:YAG laser), operating at 532 nm and laser fluence of 0.25 J cm^{-2} . The spot laser has a circular shape of 3 mm in diameter. The laser intensity profile is Gaussian and it is characterized by full width at half maximum of 1 mm. 97% of the highest laser intensity is maintained within a circular area of $600 \mu\text{m}$ in diameter centered at the maximum of laser intensity. The error in the fluence measurement is 25 mJ cm^{-2} . One pulse per sample was performed.

The NPs' structure was analyzed by X-Ray Diffraction (XRD) in grazing incidence mode ($\theta_{\text{inc}}=0.1^\circ$) using a Smartlab Rigaku diffractometer, equipped with a rotating anode of Cu $K\alpha$ radiation operating at 45 kV and 200 mA.

In order to study the evolution of the samples morphology, SEM analyses were performed by a FEI Versa 3D Dual Beam Focused Ion Beam. Due to the Gaussian profile of the laser intensity all the SEM images were performed within a circular area of about $600 \mu\text{m}$ in diameter having as center the center of the laser spot. The images were analyzed by Gatan Digital Micrograph software. In particular, to extract from the SEM images the average diameter, several SEM images per sample were considered, each containing several particles. The mean value of the NPs diameter, $\langle D \rangle$, for each sample has been calculated on a statistical population of 150 particles, with the associated error the standard deviation on the mean value.

2.2.2 Results and discussion

Figure 2.4 shows SEM images of the as-deposited Pt and Pd thin films on the FTO surface in the samples A2 and B2, respectively (so, in (a) the exposed metal surface is the Pd, in (b) the Pt one). From the images, I can recognize the typical nano-granular morphology of thin metal films (high surface energy) deposited on non-metal surface (lower surface energy) [27].

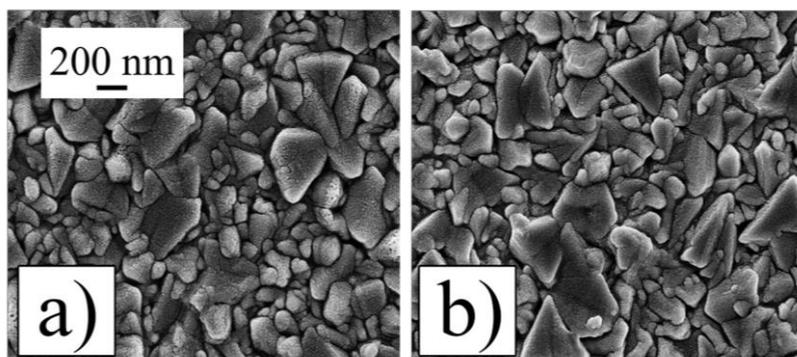


Figure 2.4 SEM images of the as-deposited Pt-Pd films on the FTO in the samples A (Pd as surface layer) (a) and with opposite sequence of the bilayers in the samples B (Pt as surface layer) (b). The pyramidal structuration of the FTO substrate is evident [22].

A RBS spectrum taken as example is shown in figure 2.5. In particular, the RBS spectrum of the reference sample A3 deposited on Si is the black line while the red line is the simulation. The XRump simulation indicates that the top layer is a Pd film with 8 nm as thickness and that the other layer is a Pt film with thickness of 8 nm.

Figure 2.6 shows the comparison between SEM images corresponding to samples irradiated by a single laser pulse at 0.25 J cm^{-2} . I can see in both sets of the samples that this fluence is enough to induce the complete breakup of the bilayers in NPs as a consequence of the films melting and solidification processes (i.e., the dewetting process [6, 28, 29]). This process is driven by the minimization of the free energy of the system and it begins with the formation of holes in the film that grow up and move to substrate surface. This mechanism leads to formation of isolated islands: the NPs. A schematic representation of NPs formation is shown in figure 2.7.

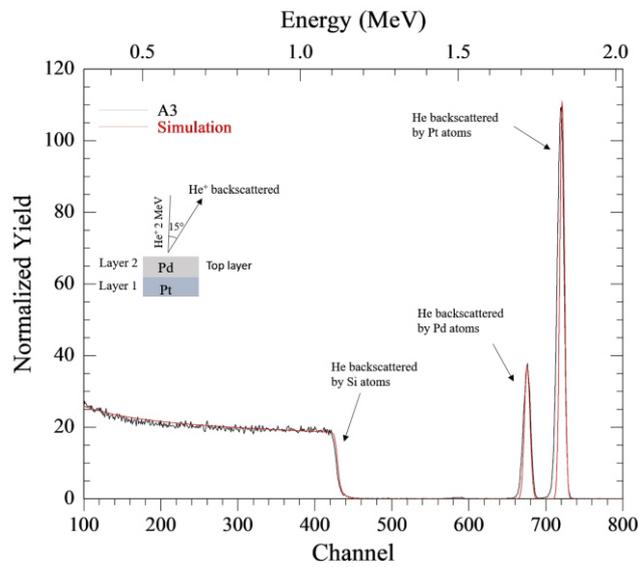


Figure 2.5 RBS spectrum of the as-deposited A3 sample with the relative simulation; the peaks of Pd, Pt and Si elements are clearly visible.

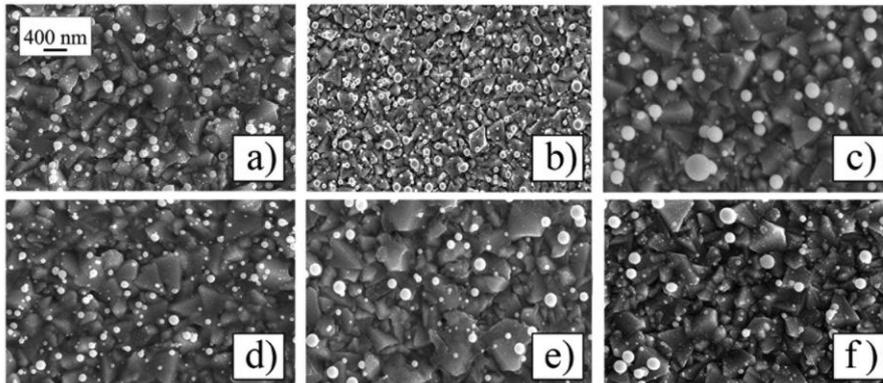


Figure 2.6 Examples of SEM images of the PtPd NPs formed on the FTO substrate after laser irradiations at 0.25 J cm^{-2} of the bilayers deposited. In particular sample A1 (a), A2 (b), A3 (c), B1 (d), B2 (e) and B3 (f) [22].

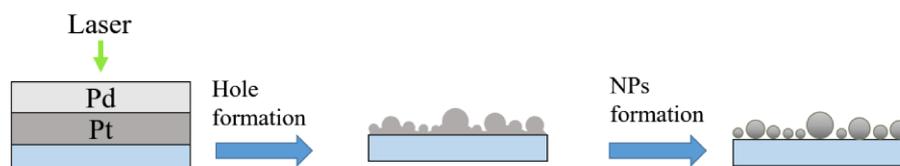


Figure 2.7 Schematic representation of the thin films retreating process and consequently NPs formation caused by laser radiation.

I have chosen the laser fluence of 0.25 J cm^{-2} because at lower fluence the temperature reached by the films is lower than film melting temperature and the dewetting does not occur.

By SEM analyses I proceeded to the quantitative evaluations of the mean size of the particles. Figure 2.8 reports the diameter distributions, respectively, of the sample A1 (a), A2 (b), A3 (c), B1 (d), B2 (e) and B3 (f). Each diameter's distribution was statically analyzed in order to extract the mean diameter of NPs, $\langle D \rangle$, and the corresponding standard deviation, ΔD , and they are shown in figure 2.9.

The following conclusions can be drawn from this plot:

- (a) $\langle D \rangle$ is independent on the Pt and Pd layers sequence once fixed the total thickness of the bilayer;
- (b) at least in the investigated 7–16 nm total thickness range, $\langle D \rangle$ seems to be independent on the total thickness of the bilayer .

So, I estimate an overall mean value of $\langle D \rangle = 75.5 \pm 27.16 \text{ nm}$ for all the samples (this implies, obviously, that increasing the total bilayer thickness, the NPs surface density increases).

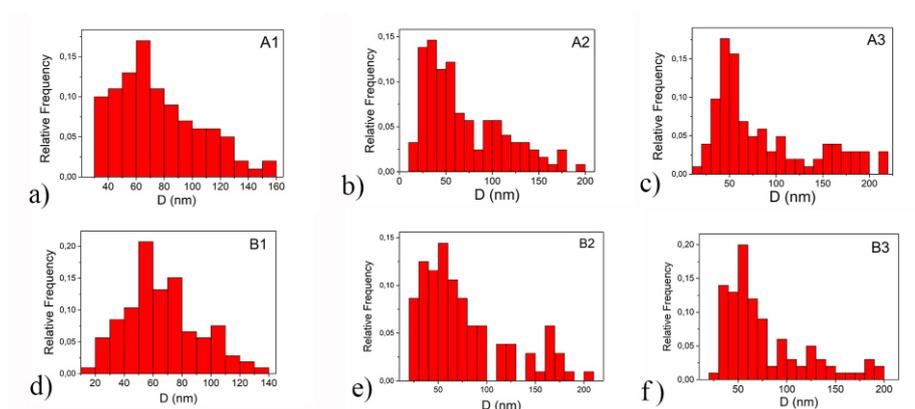


Figure 2.8 Diameter distribution of the sample A1 (a), A2 (b), A3 (c), B1 (d), B2 (e) and B3 (f) [22].

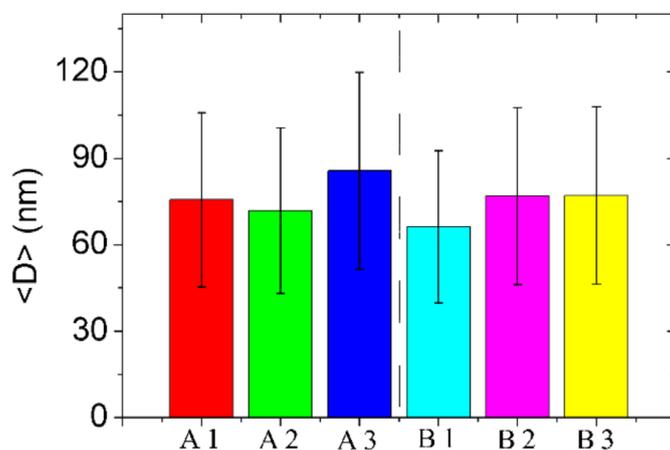


Figure 2.9 Mean Diameters of bimetallic PtPd NPs as a function of the Pt and Pd film thickness and bilayers sequence [22].

Regarding the result for which $\langle D \rangle$ is independent on the Pt and Pd layers sequence, I can comment that the total thickness of the Pt-Pd bilayer melts uniformly interacting with the laser radiation independently on the first surface layer with which the laser beam firstly interacts. In fact, at $\lambda = 532$ nm (the laser wavelength), the optical absorption lengths of Pt and Pd are

$\alpha_{Pt}^{-1}=9\text{nm}$ and $\alpha_{Pd}^{-1}=11\text{nm}$, respectively [30]. So, considering samples A1 and B1, in which the total thickness of the bilayers is 7 nm, these absorption lengths values are greater than the thickness of the deposited films ($h_{Pt} + h_{Pd} < \alpha_{Pt}^{-1}, \alpha_{Pd}^{-1}$) and, so, the laser energy is uniformly absorbed by Pt and Pd. Consequently, the total thickness of the bilayers melts uniformly interacting with the laser radiation. Instead, in the case of samples A2, A3, B2 and B3 the total thickness of Pt-Pd bilayer is greater than the optical absorption lengths ($h_{Pt} + h_{Pd} > \alpha_{Pt}^{-1}, \alpha_{Pd}^{-1}$).

However, considering the high thermal conductivity values of Pt and Pd ($K_{Pt}=71.6\text{ W/mK}$, $K_{Pd}=71.8\text{ W/mK}$, respectively [31-32]), after absorption of the laser radiation in the first outmost surface layer and in part of the second underlying layer, the laser-generated heat does not remain confined in the first surface layer, but it spreads in the second underlying layer, causing the melting of the overall bilayer. So, at least for the investigated range of the total bilayer thickness (7-16 nm), considering that the thermal conductivity and the optical absorption lengths values of Pt and Pd are very similar ($K_{Pt}\cong K_{Pd}$, $\alpha_{Pt}^{-1}\cong \alpha_{Pd}^{-1}$), I can assert that, from an optical and thermal point of view, the two materials are equivalent and interchangeable. Then, the presence of the Pd or Pt film as first surface layer on which the laser radiation impacts does not influence the melting of the second underlying layer (Pt or Pd). Once in the molten state, the Pd and Pt layers, independently on the layers sequence, mix to form the PdPt alloy and then the alloy NPs by the dewetting process.

Regarding the observed independence of $\langle D \rangle$ on the bilayer thickness, further future experimental analyses are needed to understand such a behaviour. In fact, generally, the dewetting process of thin metal films should determine the formation of NPs with increasing size by increasing the film thickness [28]. However, this result is expected for the dewetting process of thin metal films on flat surfaces. For example, Kunwar, Pandey et al. obtained monometallic Pd and Pt NPs on a flat sapphire substrate by solid-state dewetting of deposited Pd or Pt thin films by means of thermal process in oven, maintaining the temperature below the melting temperature of Pt and Pd [33, 34]. This process leads to the formation of NPs from the deposited film through surface diffusion, nucleation, Volmer-Weber growth and surface

energy minimization mechanism [33-36]. So, Kunwar et al. obtained NPs with size that increases when the thickness of the deposited films increases from 1 to 40 nm [34].

I recall that in a general dewetting phenomenon, a deposited thin film breaks up into particles via one of three mechanisms [6]: (1) heterogeneous nucleation (a surface defect catalyses the process), (2) homogeneous nucleation (the holes' formation in the film is due to thermal density fluctuations) and (3) spinodal dewetting (caused by the enhancement of periodical film thickness fluctuation).

In our case, because the temperature reached by the film, by interacting with the laser, is higher than the metals melting temperature, the dewetting process takes place in the molten phase, which involves, mainly, spinodal dewetting [6, 37-41]. Indeed, when a nanosecond laser irradiation is used to melt film with thickness from 1 to 100 nm, the decomposition of the film and the formation of holes occurs spontaneously and the formation of the NPs ensues. In this case, characteristic length scales emerge which vary with film thickness [37,42,43]. In particular, the NPs obtained by this process should be characterized by mean diameter $\langle D \rangle$ which can be expressed, as a function of the initial film thickness h , by a power-law relation $\langle D \rangle \propto h^{5/3}$ [28, 9]. However, even if the spinodal dewetting process should be the dominant nano-structuration mechanism, in our case, it occurs for the Pt-Pd bilayers on a structured surface (the pyramidal structured FTO surface). In this case, the situation is more complex than the dewetting process of deposited films on flat surfaces. In fact, in this case, also the local surface curvature drives the dewetting process in addition to the total surface energy minimization, leading to a preferential formation of the NPs in-between, or over, the FTO pyramids.

This point will be deeper analyzed in the next section by performing the laser-induced dewetting process of the Pt and Pd films on patterned surfaces and studying the resulting properties of the formed NPs.

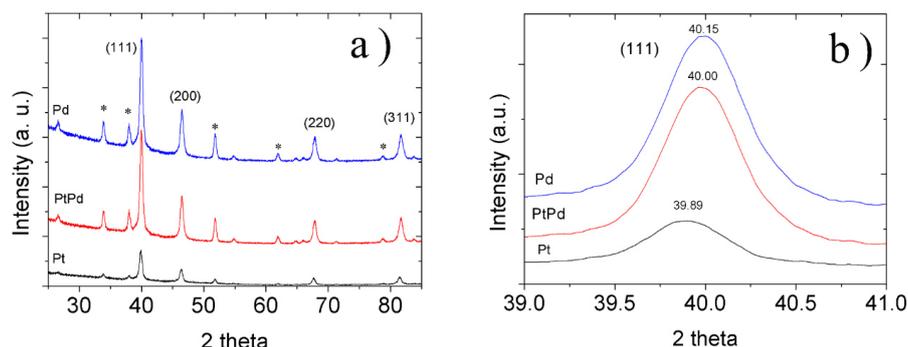


Figure 2.10 a) XRD patterns of Pt, PtPd and Pd NPs on fluorine-doped tin oxide coated glass substrates. Peaks marked with * originated from the FTO substrate. b) An expanded view of the (111) peaks [22].

XRD measurements on the samples were carried out to determine whether the NPs consisted of PtPd alloy. In order to make a comparison, Pt and Pd NPs were prepared following the same procedure: 13 nm-thick Pd film or 13 nm-thick Pt film was deposited on the FTO substrate and laser irradiations (a single laser pulse at the 0.25 J/cm^2) were performed to obtain the Pd or Pt NPs. XRD patterns of Pt, Pd, PtPd NPs on FTO substrate are shown in fig. 2.10. In the case of Pt and Pd NPs, the XRD peaks match that of fcc Pt (JCPDF 04-0802) and Pd (JCPDF 46-1043), respectively. The PtPd NPs show peaks similar to those of the elemental NPs. An expanded view of the (111) peak of three samples is shown in fig. 2.10 b). It can be clearly seen that the position of the (111) peak of PtPd (40.00°) is between that of pure Pt (39.89°) and pure Pd (40.15°) NPs. This is a clear indication of the formation of PtPd alloy [23-24, 44-45]. This is consistent to the fact that the Pt-Pd system shows no (or negligible) miscibility gap for the whole range of concentrations, forming continuous and homogeneous solid solutions across the entire range of composition by alloying [46].

2.3 Characteristics of monometallic Pt and Pd NPs produced on FTO and study of dewetting process on structured substrates

In the previous section, bimetallic nanoparticles were produced by laser irradiation of multilayers through the dewetting process. But, I found that the mean diameter of the NPs was independent on the total thickness of the deposited bilayer. In a general dewetting process, the size of the particles should be increase when the film thickness increases. However, this result is expected for the dewetting process of thin metal films on flat surfaces, and in our case, the substrate was structured, with pyramidal morphology. Moreover, observing the size distributions in figure 2.8, in particular for thicker films, there seems to be the presence of two different NPs sub-populations, consist by small nanoparticles (subpopulation 1) and large nanoparticles (subpopulation 2) and not only one, as in standard dewetting on a flat surface.

So, in order to deep the previous results, I deposited monometallic Pt and Pd films, with various thickness h , on FTO substrate and I processed, by the laser pulse, the films melting and solidification processes. The results concerning the Pd and Pt NPs sizes versus starting films thickness and substrate topography are discussed. In particular, the presented discussion is based on the elucidation of the effect of the substrate topography on the dewetting process through the excess of chemical potential [47].

2.3.1 Experimental section

The same experimental setup as in the previous section has been used. Pt and Pd have been sputtered on FTO substrates. The thicknesses of the samples are: $h_{Pd}=3.0, 7.5, 17.6, 27.9$ nm for the Pd films, and $h_{Pt}=7.5, 12.2, 19.5$ nm for the Pt films, with a measurement error of 5%.

The metal films supported on the FTO surface of the glass/FTO slides were processed by nanosecond laser irradiation (1 pulse per film). For the experiments presented in this section, a laser fluence of 0.50 J/cm^2 is used (measurement error of 0.025 J/cm^2). Compared to the previous experiment for

Pt-Pd bilayers, I used higher fluence because thicker films have been irradiated. In fact, the thermal budget necessary to cause the dewetting process induced by laser irradiation depends on how the laser-generated heat is dissipated: if the metal film deposited on a low thermal conductive substrate (i.e. SiO₂, thermal conductivity 1.4 W/mK [48]), the laser-generated heat will remain confined in the metal film, resulting in a high increase of the temperature; instead, if a metal film is deposited on higher thermal conductive substrate (i.e. SnO₂, thermal conductivity 40 W/mk [49]), the laser-generated heat it will dissipate quickly through the substrate [50]. In this last case, the thermal budget needed for the same temperature increase (as in the case of SiO₂ substrate) will be higher. So, to induce dewetting of a thicker film on FTO the laser fluence is higher.

Microscopic morphological analyses were carried out by using a scanning electron microscope. The Gatan Digital Micrograph software was used to extract quantitative information by the SEM images. The mean value of the NPs' diameter $\langle D \rangle$ (and the corresponding error arising as the standard deviation) for each sample has been quantified on a statistical population of 400 NPs. In addition, the mean surface density $\langle N \rangle$ (number of particles per unit area) was evaluated by direct counting and averaging on several SEM images.

2.3.2 Results and discussion

- ***Morphology of the as-deposited monometallic films on FTO***

In figure 2.11 and figure 2.12 some exemplificative microscopies of the FTO surface naked and covered by the Pd and Pt films are reported. In particular, in fig. 2.11.a and 2.12.a the pyramidal structuration of the pristine FTO used as substrate is evident. Figure 2.11 refers to the Pd covered FTO surface with increasing effective thickness of the covering metal film: $h_{Pd}=3.0$ nm (b) and $h_{Pd}=27.9$ nm (c); the figures d), e) and f) are an enlargement of fig. a), b) and c), respectively. Figure 2.12 refers to the Pt covered FTO surface with increasing effective thickness of the covering metal film: $h_{Pt}=7.5$ nm (b)

and $h_{Pt}=19.5$ nm (c); the figures d), e) and f) are an enlargement of fig. a), b) and c), respectively. Increasing the amount of sputtered Pd or Pt (i. e. increasing the effective thickness of the deposited metal film), an evolution of the surface morphology can be observed: the pyramidal structuration of the FTO layer is yet recognizable; however, over the pyramids surfaces a nano-granular morphology develops (see, in particular, the figures ad high magnification fig. 2.11 (f) and fig. 2.12 (f)).

This morphology is the standard one, in the initial stages of growth (i. e. nucleation and growth) for metal films deposited on non-metal substrates and which leading growth process is the Volmer-Weber growth mode [7, 8, 15, 21, 28, 51-54].

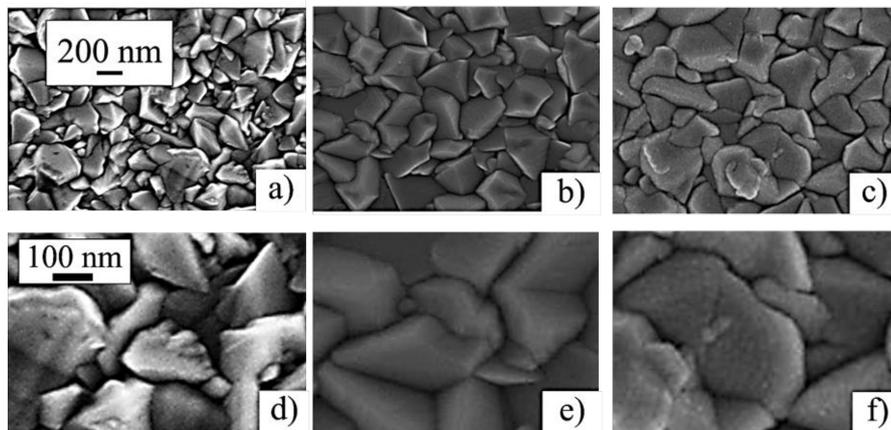


Figure 2.11 SEM images of the FTO bare surface a) and FTO surface covered by Pd film with effective thickness of: 3 nm b) and 27.9 nm c). The figures d), e) and f) are an enlargement of fig. a), b) and c), respectively. The presence of the films can be recognized in more rough pyramids surfaces with respect to bare surfaces [47].

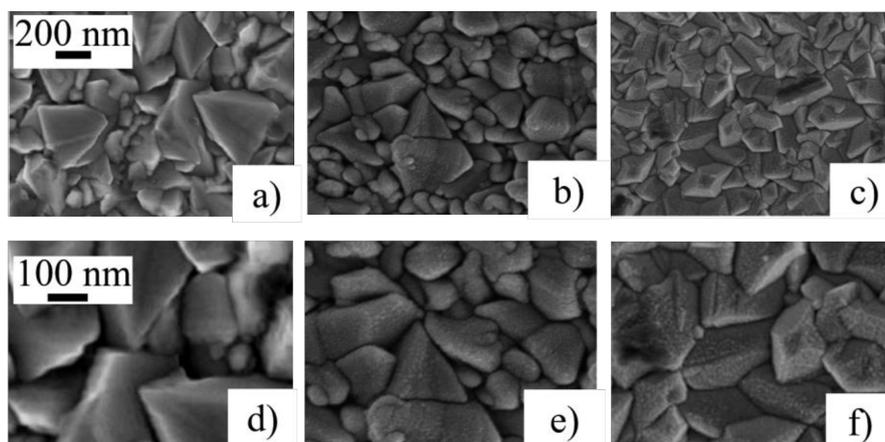


Figure 2.12. SEM images of the FTO bare surface a) and FTO surface covered by Pt film with effective thickness of: 7.5 nm b) and 19.5 nm c). The figures d), e) and f) are an enlargement of fig. a), b) and c), respectively. The presence of the films can be recognized in more rough pyramids surfaces with respect to bare surfaces [47].

However, in late stages of growth, increasing the amount of deposited atoms, the nucleated small metal islands grow until to contact each other giving place to a coalesce process [52-54]. In this stage, a percolative surface morphology of the metal film is obtained in the sense that it is formed by ramified interconnected nano-islands separated by small gaps [52-54]. Finally, continuing to deposit more and more material, holes in the growing metal film are filled to form a continuous rough film [52-54].

- ***Laser irradiations and NPs formation***

On each metal-covered sample, I carried out the laser irradiation. Then, I used the SEM analysis to study the metal surface morphology evolution versus the metal film thickness, see fig. 2.13 and fig. 2.14. In general, the pulsed laser-induced dewetting of the metal film is observed, i. e. the 0.50 J/cm² laser irradiation for 10 ns causes the melting of the Pd or Pt film followed by the film rupture and retreating processes towards the formation of NPs of circular

section (fig. 2.13 and fig. 2.14). The spherical (or quasi-spherical) shape of the NPs can be easily recognized from the SEM images in fig. 2.13 and fig. 2.14 where in several cases NPs are observed from a tilted configuration due to the surface structuration of the FTO surface (i. e. the NPs placed on the lateral surfaces of the FTO pyramids). In fact, generally, metal films on transparent conductive oxides are highly non-wetting systems [8] so that, after the dewetting process, spherical or almost-spherical NPs are obtained (i. e. maximization of the contact angle).

In particular, fig. 2.13 presents typical SEM microscopies showing the Pd NPs originated from the pulsed laser irradiation of the FTO-supported Pd film having thickness 3.0 nm (a) and 27.9 nm (b); in addition, fig. 2.14 presents SEM microscopies showing the Pt NPs originated from the irradiation of the FTO-supported Pt film with thickness 7.5 nm (a) and 19.5 nm (b).

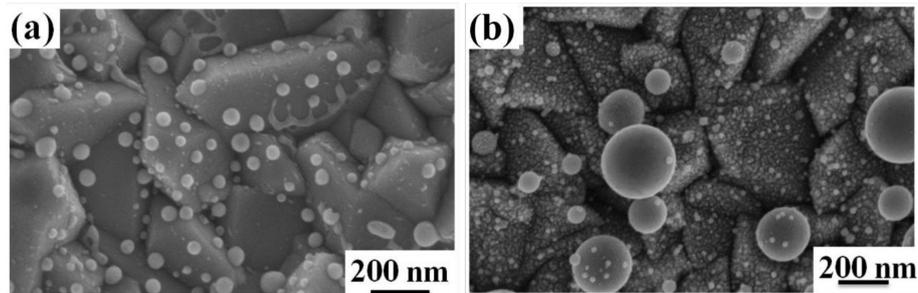


Figure 2.13 SEM images of the FTO surface covered by Pd film after the 0.50 J/cm^2 laser pulse ((a) 3 nm-thick, (b) 27.9 nm-thick). The formation of almost-spherical particles on the FTO surface is recognizable both in (a) and (b) [47].

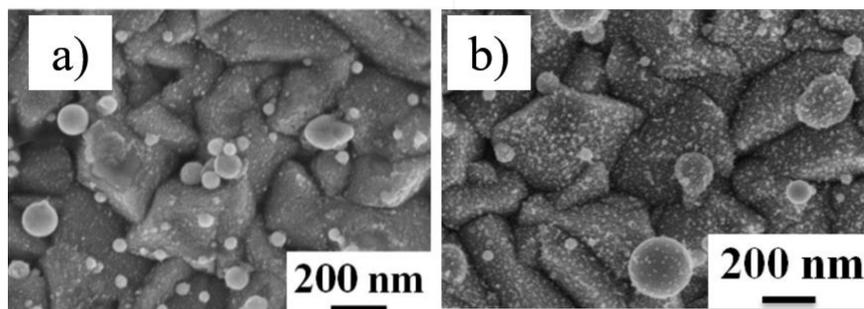


Figure 2.14. SEM images of the FTO surface covered by Pt film after the 0.50 J/cm^2 laser pulse ((a) 7.5 nm-thick, (b) 19.5 nm-thick). The formation of almost-spherical particles on the FTO surface is recognizable [47].

It is, nowadays, well-established [4-9, 15, 21, 26, 55] that during the nanosecond pulsed laser irradiation of deposited nanoscale-thick metal films, the NPs are formed from the continuous films by a molten-phase dewetting process. In fact, in standard metals (such as Pd and Pt) the thermal equilibrium between hot electrons and phonons is established, typically, within a characteristic time $t_{\text{eq}} \approx 50 \text{ ps}$ [4-9, 15, 21, 26, 55]. Using nanosecond pulsed laser to generate heat in the film, as in the present experiments for which the pulse duration is $\tau = 10 \text{ ns}$ so that $\tau \gg t_{\text{eq}}$, then the metal film melting dynamics is the main process [4-9, 15, 21, 26, 55]. Therefore, in the present experiments, the Pd and Pt dewetting process occurs with the films being in the molten state (i.e. spinodal dewetting [4-9, 15, 21, 26, 55]) followed by the films solidification. Shortly, as seen in chapter 1, the dewetting process starts by the film perforation that leads to holes' formation in the film and, in the final stage, leads to an array of metal NPs that uniformly cover the laser-irradiated surface.

I proceeded, then, to the quantitative analysis of the Pd and Pt NPs characteristics using the SEM images. In particular, for each sample, distributions of the NPs diameter D were constructed as described in the experimental section. Figure 2.15 reports some examples of obtained diameters distributions: (a) and (b) are the diameters distributions for the NPs obtained by the laser irradiation of the 3 nm-thick (a) and 27.9 nm-thick (b)

Pd films deposited on the FTO surface; (c) and (d) are the diameters distributions for the NPs obtained by the laser irradiation of the 7.5 nm-thick (c) and 19.5 nm-thick (d) Pt films deposited on the FTO surface. As easily recognizable, (a) and (c) show a monomodal size distribution (sub-population 1), while (b) and (d) bimodal sizes distributions (sub-population 1 of smaller nanoparticles and sub-population 2 of bigger nanoparticles).

Each diameters distribution was, hence, statistically analyzed to extract the mean diameter $\langle D \rangle$ (and the corresponding standard deviation ΔD) of the NPs. In addition, I evaluated the mean NPs surface density $\langle N \rangle$ and the corresponding errors. The results are summarized in the plots in fig. 2.16. In particular, performing these analyses, in some samples I observed a monomodal size distribution (one Gaussian distribution) indicative of an unique NPs population to which was associated an unique mean diameter, $\langle D1 \rangle$ sub-population 1, and mean NPs surface density, $\langle N1 \rangle$ sub-population 2. In other samples, I observed a bimodal size distribution (two different Gaussian distributions) indicative of two NPs sub-populations (in fig. 2.16 fully spheres represent sub-population 1 while empty spheres represent sub-population 2), to which were associated two mean diameters $\langle D1 \rangle$ sub-population 1 and $\langle D2 \rangle$ sub-population 2 and two mean NPs surface densities $\langle N1 \rangle$ sub-population 1 and $\langle N2 \rangle$ sub-population 2.

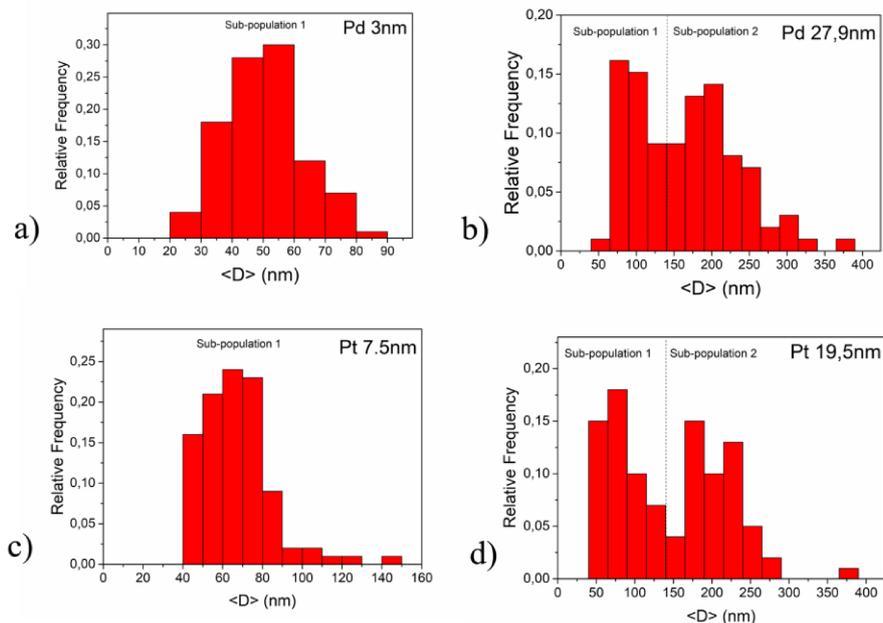


Figure 2.15 Examples of NPs diameters distributions: (a) and (b) are the diameters distributions for the NPs obtained by the laser irradiation of the 3 nm-thick ((a)) and 27.9 nm-thick ((b)) Pd films deposited on the FTO surface; (c) and (d) are the diameters distributions for the NPs obtained by the laser irradiation of the 7.5 nm-thick ((c)) and 19.5 nm-thick ((d)) Pt films deposited on the FTO surface. As easily recognizable, (a) and (c) shows a monomodal size distribution (sub-population 1) while (b) and (d) bimodal sizes distributions (sub-population 1 and sub-population 2).

Specific values for $\langle D1 \rangle$, $\langle D2 \rangle$, $\langle N1 \rangle$ and $\langle N2 \rangle$ are, further, summarized in Table 2.3 for the various samples.

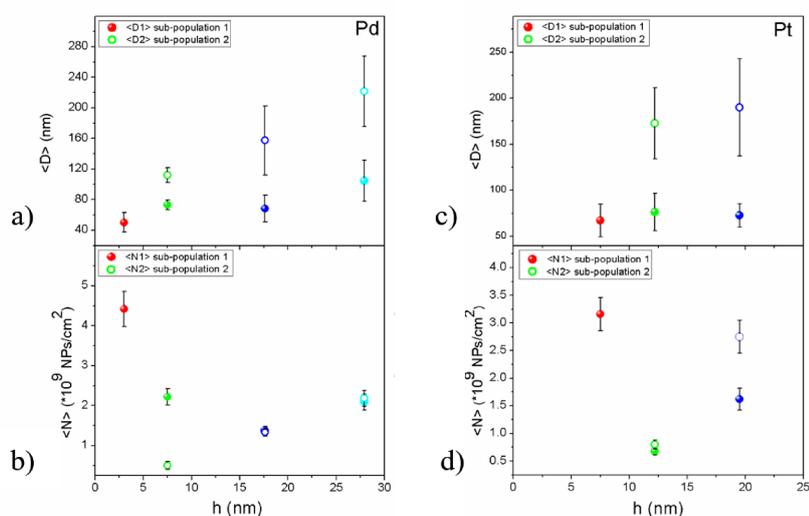


Figure 2.16 Mean diameter $\langle D \rangle$ (a) and mean surface density $\langle N \rangle$ (b) of the Pd NPs obtained by the 0.50 J/cm^2 laser irradiation of the 3 nm, 7.5 nm, 17.6 nm, 27.9 nm thick deposited Pd films. Mean diameter $\langle D \rangle$ (c) and mean surface density $\langle N \rangle$ (d) of the Pt NPs obtained by the 0.50 J/cm^2 laser irradiation of the 7.5 nm, 12.2 nm, 19.5 nm-thick deposited Pt films. The indication of two values for $\langle D \rangle$ or $\langle N \rangle$ for the same sample means the presence of two different NPs sub-populations in that sample, in particular full spheres represent the sub-population 1, while empty spheres represent the sub-population 2.

Table 2.3. Summary of the values of $\langle D_1 \rangle$, $\langle D_2 \rangle$, $\langle N_1 \rangle$, $\langle N_2 \rangle$ for the NPs in the samples.

Thickness of the film-material	$\langle D_1 \rangle$ [nm]	$\langle N_1 \rangle$ [$\times 10^9 \text{ cm}^{-2}$]	$\langle D_2 \rangle$ [nm]	$\langle N_2 \rangle$ [$\times 10^9 \text{ cm}^{-2}$]
3 nm-Pd	~50	~4.5	0	0
7.5 nm-Pd	~75	~2	~100	~0.5
17.6 nm-Pd	~70	~1.5	~150	~1.5
27.9 nm-Pd	~100	~2	~220	~2
7.5 nm-Pt	~70	~3.2	0	0
12.2 nm-Pt	~75	~0.6	~220	~0.6
19.5 nm-Pt	~70	~1.6	~180	~2.7

- *Dewetting on structured substrates*

Regarding the standard dewetting process of metal films on flat surfaces [4-12, 28], a unique NPs population is expected with a mean size, which increases by increasing the starting thickness of the deposited film. The observation of the formation of two different NPs population in some samples is, so, indicative of the effect of the substrate non-flat surface topography on the film dewetting process, influencing, then, the size of the NPs. To describe this effect I, briefly, discuss some results obtained by Gierman and Thompson [56]. They intentionally patterned, by using electron beam lithography, a SiO_2 surface in spatially ordered arrays of inverted pyramid shaped pits. However, different patterns were designed by changing the spatial period of the pits (175 or 377 nm) and the pit-to-mesa width ratio (1.5, 1.9, 5.3). Onto the so-patterned SiO_2 surface, Au films of different thickness (16, 21, 32 nm) were evaporated. The Au films solid-state dewetting process was activated by 800°C annealing process. The microscopic analysis revealed for the resulting Au NPs originated by the dewetting process, a spatial arrangement on the substrate surface and size distribution dependent on the geometric characteristics of the surface pattern (spatial period of the pits and pit-to-mesa width ratio) in combination with the Au film thickness. On the basis of the

combination of these parameters: in some cases, the preferential formation of a single NP per pits with no NPs on the mesa was observed; in other cases, the formation of one NP per pit with some other NPs on the mesa was achieved; in further cases, the generation of multiple NPs per pit with some other NPs on the mesa resulted; finally, some other combinations lead to the formation of large NPs on the mesa (often covering the pits) with no NPs in the pits. These results clearly demonstrated the crucial effect of the surface topography on the deposited metal film dewetting giving, also, the possibility to study, quantitatively, this effect taking into account the excess of local chemical potential as modulated by the finite local curvatures on the substrate surface [56]. In fact, considering the dewetting process of a thin metal film on a flat surface, it is clear that the driving force for the process is, solely, the minimization of the total surface and interface energy of the system. For a flat surface, the local radius of curvature is, in each surface point, $R \rightarrow \infty$. The corresponding local curvature is $\kappa = 1/R$ to which is related, by the Gibbs–Thomson relation, the local excess of chemical potential $\Delta\mu = \kappa\gamma\Omega \rightarrow 0$ (being γ the film surface energy and Ω the atomic volume). Consequently, the dewetting process of a thin film on a flat surface is not affected by the surface topography. The situation changes if the surface is not flat, i. e. if it presents finite local curvatures (as in the case of the patterned surfaces used by Giermann and Thompson). In this case, due to the finite values of R , the non-zero values of $\Delta\mu = \kappa\gamma\Omega$ introduce an additional driving force for the film dewetting process determining, in particular, a preferential material diffusion from the positions with $\kappa > 0$ (peaks or ridges, with curvature radius R_A) to the positions with $\kappa < 0$ (valleys, with curvature radius R_B), see the representative scheme in fig. 2.17. It is clear, then, the modulation of $\Delta\mu$ through the surface geometry impacts on the dewetting process and on the resulting characteristics (spatial arrangement and size) of the NPs originating from this process. Referring to the specific case reported by Giermann and Thompson [56], which is particularly useful for the interpretation of our data, the edge of a pit is characterized by a $\Delta\mu \propto 1/R_A > 0$ while the apex of an inverted pyramid is characterized by $\Delta\mu \propto -1/|R_B| < 0$, see fig. 2.17. It follows that, to minimize the total surface and interface energy of the system and to establish a global condition for which $\Delta\mu = 0$, the film material will diffuse away from the pit

edge toward the pit apex and here, preferentially, will form the NPs. However, since the local curvature at the pit edge and the apex decreases with increasing film thickness, the driving force for flow from the edge to the apex also decreases with increasing film thickness. So, overall, the effect becomes dependent on the film thickness.

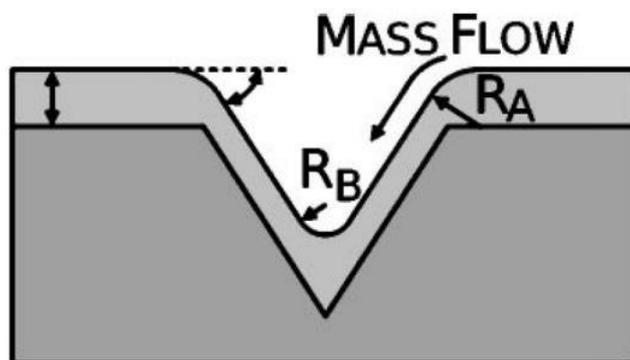


Figure 2.17 Representation of a thin film conformally covering a patterned surface. The curvature at the pit edge, R_A , and at the inverted apex, R_B are shown [56].

In our case, I observed that increasing the thickness of the Pd film from 3.5 nm to 27.9 nm and of the Pt film from 7.5 nm to 19.5 nm, the NPs population evolves from monomodal to bimodal. This indicates the existence of a critical film thickness h_c identifying a variation in the dewetting characteristics of the film, as pictured by the combination of fig. 2.18 and fig. 2.19. For $h < h_c$ (generally named “low-thickness” condition) the substrate topography does not affect the film dewetting process (fig. 2.18). In this condition, the film does not interact with the topographic features of the substrate and, then, the substrate behaves as a flat substrate with respect to the film dewetting. Hence, the film dewets as on a planar substrate originating NPs uniformly arranged over the surface of the substrate. In addition, the size of the dewetted NPs, being the starting thickness of the deposited film very low with respect to local surface curvatures (defined by the characteristic sizes of the FTO pyramids, i.e. height, width, spacing), is not influenced by the substrate topography. For $h > h_c$ (generally named “high-thickness” condition) the geometrical features of the substrate affect the film dewetting process and, hence, the resulting

mean size of the formed NPs (fig. 2.19). In this case, the thickness of the deposited film is, at least, comparable to the local surface curvatures. Then, the film dewetting is driven, in addition to the surface energy minimization, by the surface topography through the local excess of chemical potential. This results in the preferential formation of the NPs in-between or over the pyramids. In particular, at the apex of a pyramid, i.e. where the surface is flat, $\Delta\mu=0$ and the film dewetting is driven by the surface energy minimization; but, in and between the pyramids $\Delta\mu\neq 0$, hence, it is clear that the characteristic sizes of the FTO pyramids affects the final NPs mean size. The overall effect is determined by an interplay between the FTO pyramids sizes (establishing the local surface curvatures) and the thickness h of the film, or, in other words determined by an interplay between $\Delta\mu\neq 0$ and $\Delta\mu=0$, leading to the formation of nanoparticles with 2 different subpopulations: subpopulation 1, formed by smaller nanoparticles, and subpopulation 2, formed by larger nanoparticles.

Therefore, observing fig. 2.16, in that samples where a unique population of NPs is obtained, the situation $h < h_c$ is realized (dewetting as on a flat surface), whereas in that samples where two NPs sub-populations are obtained, the situation $h > h_c$ is realized (substrate topography-driven dewetting).

Then, I can conclude, also, that $3 \text{ nm} < h_c < 7.5 \text{ nm}$ for the Pd film and that $7.5 \text{ nm} < h_c < 12.2 \text{ nm}$ for the Pt film.

In addition, the film thicknesses are smaller than the roughness of the FTO, $h < \sigma_{FTO} = 32.7 \text{ nm}$, so the effect is driven only by the local curvature pyramids of the substrate.

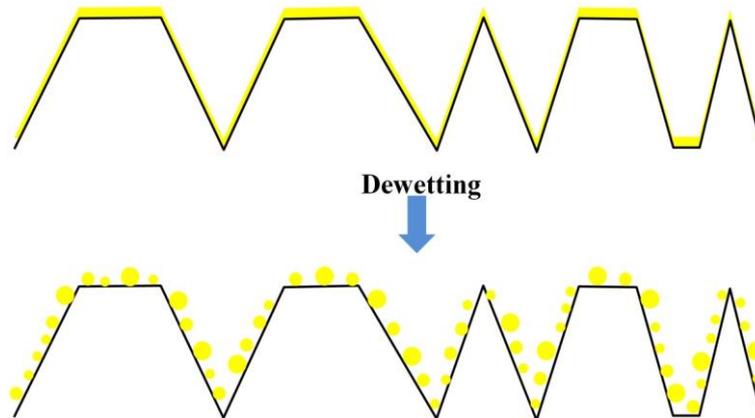


Figure 2.18 Picture of the result of the “low-thickness”-film dewetting process on the FTO topographically structured surface. Small NPs are uniformly distributed over the entire FTO surface (as on a flat surface) [47].

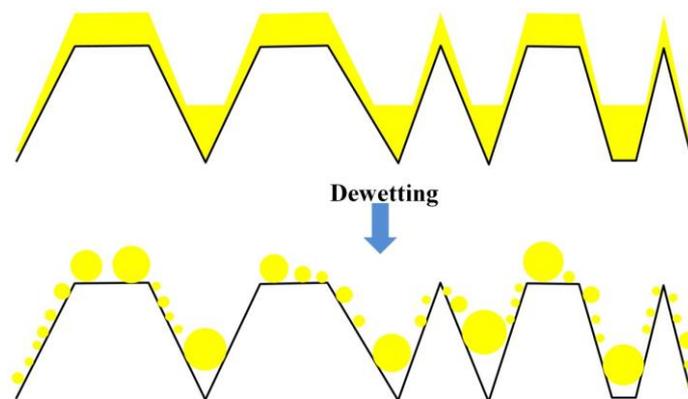


Figure 2.19 Picture of the result of the “high-thickness”-film dewetting process on the FTO topographically structured surface. Large NPs are preferentially formed in-between or over the FTO pyramids [47].

2.4 Conclusions

In this chapter has been shown a method for the controlled production of mono and bimetallic NPs on substrate, based on nanosecond laser irradiation of Pt-Pd deposited films that induces melting, alloying and dewetting of the films. The NPs have been characterized from a point of view morphological and chemical.

In the first instance, despite what is expected in a spinodal dewetting process on flat surface, the microscopic analyses revealed that the average diameter of NPs was independent on the thickness of the deposited film. Furthermore, the size distributions of the nanoparticles seemed to show the presence of two different NPs' sub-populations and not only one.

For these reasons, particular attention has been devoted to the study of the effect of substrate's topography on the average size of the produced NPs. In particular, I observed that increasing the thickness of the film the NPs population evolves from monomodal to bimodal. This indicates the existence of a critical film thickness h_c identifying a change in the dewetting characteristics of the film: for $h < h_c$ the substrate topography does not influence the film dewetting process, while for $h > h_c$ the topography of the substrate is crucial in determining the dewetting process and, so, the final mean size of the produced NPs. In those samples where a unique population of NPs is obtained the situation $h < h_c$ is realized (dewetting as on a flat surface), whereas in that samples where two NPs sub-populations are obtained the situation $h > h_c$ is realized (substrate topography-driven dewetting).

Chapter 2 References

1. J. Schulte, *Nanotechnology: Global Strategies, Industry Trends and Applications*, John Wiley & Sons Ltd., 2005.
2. K. Forte, J. Serbin, J. Koch, A. Egbert, C. Fallnich, A. Ostendorf, B. N. Chichkov, Towards nanostructuring with femtosecond laser pulse. *Appl. Phys. A* 2003, 77, 229-235. <https://doi.org/10.1007/s00339-003-2110-z>
3. J.P. Moening, S. S. Thanawala, D. G. Georgiev, Formation of high-aspect-ratio protrusions on gold films by localized pulsed laser irradiation. *Appl. Phys. A*, 95 (2009) 635-638. <https://doi.org/10.1007/s00339-009-5166-6>
4. C. Favazza, R. Kalayanaraman, R. Sureshkumar, Dynamics of ultrathin metal films on amorphous substrates under fast thermal processing, *J. Appl. Phys.*, 102 (2007) 104308. <https://doi.org/10.1063/1.2812560>
5. S. J. Henley, J. D. Carrey, S. R. P. Silva, Metal nanoparticle production by pulsed laser nanostructuring of thin metal films, *Appl. Surf. Sci.*, 253 (2007) 8080-8085. <https://doi.org/10.1016/j.apsusc.2007.02.132>
6. J. Trice, D. Thomas, C. Favazza, R. Sureshkumar, R. Kalyanaraman, Pulsed-laser induced dewetting in nanoscopic metal films: theory and experiments, *Phys. Rev. B*, 75 (2007) 235439. DOI:<https://doi.org/10.1103/PhysRevB.75.235439>
7. F. Ruffino, A. Pugliara, E. Carria, C. Bongiorno, C. Spinella, M. G. Grimaldi, Formation of nanoparticles from laser irradiated Au thin films on SiO₂/Si: elucidating the Rayleigh-instability role, *Mater. Lett.*, 84 (2012) 27-30. <https://doi.org/10.1016/j.matlet.2012.06.055>
8. F. Ruffino, E. Carria, S. Kimiagar, I. Crupi, F. Simone, M. G. Grimaldi, Formation and evolution of nanoscale metal structures on ITO surface by nanosecond laser irradiations of thin Au and Ag films, *Sci. Adv. Mater.*, 4 (2012) 708-718. DOI: 10.1166/sam.2012.1342
9. F. Ruffino, M. G. Grimaldi, Controlled dewetting as fabrication and patterning strategy for metal nanostructures, *Phys. Stat. Sol. A*, 212 (2015) 1662-1684. <https://doi.org/10.1002/pssa.201570453>

10. A. G. González, J. A. Diez, Y. Wu, J. D. Fowlkes, P. D. Rack, L. Kondic, Instability of liquid Cu films on a SiO₂ substrate, *Langmuir*, 29 (2013) 9378-9387. <https://doi.org/10.1021/la4009784>
11. J. D. Fowlkes, L. Kondic, J. Diez, P. D. Rack, Self-assembly versus directed assembly of nanoparticles via pulsed laser induced dewetting of patterned metal films, *Nano Lett.*, 11 (2011) 2478-2485. <https://doi.org/10.1021/nl200921c>
12. F. Ruffino, A. Pugliara, E. Carria, L. Romano, C. Bongiorno, G. Fisicaro, A. La Magna, C. Spinella, M. G. Grimaldi, Towards a laser fluence dependent nanostructuring of thin Au films on Si by nanosecond laser irradiation, *Appl. Surf. Sci.*, 258 (2012) 9128-9137. DOI: 10.1016/j.apsusc.2011.12.087
13. A. E. Rakhshani, Y. Makdisi, H. A. Ramazaniyan, Electronic and optical properties of fluorine-doped tin oxide films, *J. Appl. Phys.*, 83 (1998) 1049-1057. <https://doi.org/10.1063/1.366796>
14. E. Elangovan, K. Ramamurthi, A study on low cost-high conducting fluorine and antimony-doped tin oxide thin films, *Appl. Surf. Sci.*, 249 (2005), 183-196. <https://doi.org/10.1016/j.apsusc.2004.11.074>
15. F. Ruffino, A. Gentile, M. Zimbone, G. Piccitto, R. Reitano, M. G. Grimaldi, Size-selected Au nanoparticles on FTO substrate: Controlled synthesis by the Rayleigh-Taylor instability and optical properties, *Superlatt. Microstruct.*, 100 (2016) 418-430. DOI: 10.1016/j.spmi.2016.09.047
16. A. Gentile, G. Cacciato, F. Ruffino, R. Reitano, G. Scapellato, M. Zimbone, S. Lombardo, A. Battaglia, C. Gerardi, M. Foti, M. G. Grimaldi, *J Mater Sci*, 49 (2014) 8498–8507. DOI 10.1007/s10853-014-8560-1
17. D. S. Ginley, H. Hosono, D. C. Paine, *Handbook of Transparent Conductors*, Springer, 2010.
18. C. A. Kent, J. J. Concepcion, C. J. Dares, D. A. Torelli, A.J. Rieth, A. S. Miller, T. J. Meyer, Water Oxidation and Oxygen Monitoring by Cobalt-Modified Fluorine-Doped Tin Oxide Electrodes, *J. Am. Chem. Soc.*, 135 (2013) 8432–8435. <https://doi.org/10.1021/ja400616a>
19. <http://www.kintec.hk/>

20. J. T. Wang, X. L. Shi, W. W. Liu, X. H. Zhong, J. N. Wang, L. Pyrah, K. D. Sanderson, P. M. Ramsey, M. Hirata, K. Tsuru, Influence of Preferred Orientation on the Electrical Conductivity of Fluorine-Doped Tin Oxide Films, *Sci. Rep.*, 4 (2014) 3679. <https://doi.org/10.1038/srep03679>
21. J. T. Wang, X. L. Shi, X. H. Zhong, J. N. Wang, L. Pyrah, K. D. Sanderson, P. M. Ramsey, M. Hirata, K. Tsuru, Morphology control of fluorine-doped tin oxide thin films for enhanced light trapping, *Solar Energy Materials and Solar Cells*, 132 (2015) 578-588. <https://doi.org/10.1016/j.solmat.2014.09.043>
22. M. Censabella, F. Ruffino, M. Zimbone, E. Bruno, M. G. Grimaldi, Self-Organization Based Fabrication of Bimetallic PtPd Nanoparticles on Transparent Conductive Oxide Substrates, *Phys. Status Solidi A*, 215 (2017) 1700524-1700524. <https://doi.org/10.1002/pssa.201700524>
23. R. Esparza, A. Santovena, A. Ruiz-Baltazar, A. Angeles-Pascual, J. Maya-Cornejo, J. Ledesma-Garcia, R. Pérez, Study of PtPd Bimetallic Nanoparticles for Fuel Cell Applications, *Mat. Res.* 20 (2017) 1193-1200. DOI: 10.1590/1980-5373-mr-2016-0934;
24. X. Yang, Q. Yang, J. Xu and C. S. Lee, Bimetallic PtPd nanoparticles on Nafion–graphene film as catalyst for ethanol electro-oxidation, *J. Mater. Chem.*, 22 (2012) 8057. DOI: 10.1039/C2JM16916A
25. M. Yamauchi, H. Kobayashi, H. Kitagawa, Hydrogen Storage Mediated by Pd and Pt Nanoparticles, *Chem. Phys. Chem.*, 10 (2009) 2566 – 2576. <https://doi.org/10.1002/cphc.200900289>
26. Z. Zhou, Z. Song, L. Li, J. Zhang, Z. Wang, Fabrication of periodic variable-sized Pt nanoparticles via laser interference patterning, *Appl. Surf. Sci.*, 335 (2015) 65-70. <https://doi.org/10.1016/j.apsusc.2015.02.021>
27. F. Ruffino, V. Torrisi, G. Marletta, M. G. Grimaldi, Surface diffusion coefficient of Au atoms on single layer graphene grown on Cu, *Appl. Phys. A*, 100 (2010) 7. <https://doi.org/10.1063/1.4866876>
28. C. V. Thompson, Solid-State Dewetting of Thin Films, *Annu. Rev. Mater. Res.*, 42 (2102) 399-434. <https://doi.org/10.1146/annurev-matsci-070511-155048>

29. J. Y. Kwon, T. S. Yoon, K. B. Kim, S. H. Min, Comparison of the agglomeration behavior of Au and Cu films sputter deposited on silicon dioxide, *J. Appl. Phys.*, 93 (2003) 3270-3278. <https://doi.org/10.1063/1.1556178>
30. <https://refractiveindex.info>
31. <http://www.efunda.com>
32. <http://periodictable.com>
33. P. Pandey, M. Sui, Q. Zhang, M. Y. Li, S. Kunwar, J. Lee, Systematic control of the size, density and configuration of Pt nanostructures on sapphire (0 0 0 1) by the variation of deposition amount and dwelling time, *Appl. Surf. Sci.*, 368 (2016) 198-207. <https://doi.org/10.1016/j.apsusc.2016.02.001>
34. S. Kunwar, M. Sui, P. Pandey, Q. Zhang, M. Y. Li, H. Bhandari, J. Lee, Determination of growth regimes of Pd nanostructures on c-plane sapphire by the control of deposition amount at different annealing temperatures, *Phys. Chem. Chem. Phys.*, 19 (2017) 15084-15097. DOI:10.1039/C7CP01410D
35. M. Sui, M. Y. Li, S. Kunwar, P. Pandey, Q. Zhang, J. Lee, Effects of annealing temperature and duration on the morphological and optical evolution of self-assembled Pt nanostructures on c-plane sapphire, *PLoS ONE* 12 (2017) : e0177048. <https://doi.org/10.1371/journal.pone.0177048>
36. S. Kunwar, P. Pandey, M. Sui, Q. Zhang, M. Y. Li, J. Lee, Nanoscale morphology and optical property evolution of Pt nanostructures on GaN (0 0 0 1) by the systematic control of annealing temperature and duration with various Pt thickness, *Mater. Res. Express*, 4 (2017). <https://doi.org/10.1088/2053-1591/aa72be>
37. H. Krishna, C. Favazza, A. K. Gangopadhyay, R. Kalyanaraman, Functional nanostructures through nanosecond laser dewetting of thin metal films, *JOM* 60 (2008) 37. <https://doi.org/10.1007/s11837-008-0115-y>
38. S. Yadavali, M. Khenner, R. Kalyanaraman, Pulsed laser dewetting of Au films: Experiments and modeling of nanoscale behavior, *J. Mater. Res.*, 28 (2013) 1715. <https://doi.org/10.1557/jmr.2013.90>

39. M. Khenner, S. Yadavali, R. Kalyanaraman, Controlling Nanoparticles Formation in Molten Metallic Bilayers by Pulsed-Laser Interference Heating, *Math. Model. Nat. Pheno.* 7 (2012) 20. <https://doi.org/10.1051/mmnp/20127403>
40. N. Shirato, H. Krishna, R. Kalyanaraman, Thermodynamic model for the dewetting instability in ultrathin films, *J. Appl. Phys.*, 108 (2010) 024313. <https://doi.org/10.1063/1.3456062>
41. H. Krishna, N. Shirato, C. Favazza, R. Kalyanaraman, Energy driven self-organization in nanoscale metallic liquid films, *Phys. Chem. Chem. Phys.*, 11 (2009) 8136. DOI: 10.1039/B906281P
42. R. G. Nikov, N. N. Nedyalkov, P. A. Atanasov, D. Hirsch, B. Rauschenbach, K. Grochowska, G. Sliwinski, Characterization of Ag nanostructures fabricated by laser-induced dewetting of thin films, *Appl. Surf. Sci.*, 374 (2016) 36-41 <https://doi.org/10.1016/j.apsusc.2015.09.004>
43. K. Grochowska, K. Siuzdak, P. A. Atanasov, C. Bittencourt, A. Dikovska, N. N. Nedyalkov, G. Śliwiński, Properties of plasmonic arrays produced by pulsed-laser nanostructuring of thin Au films, *Beilstein J. Nanotechnol.*, 5 (2014) 2102–2112. doi: 10.3762/bjnano.5.219
44. J. Liu, S. D. Zou, L. Xiao and J. Fan, Well-dispersed bimetallic nanoparticles confined in mesoporous metal oxides and their optimized catalytic activity for nitrobenzene hydrogenation, *Catal. Sci. Technol.* 4 (2014) 441–446. DOI: 10.1039/C3CY00689A
45. C. Zhu, S. Guo and S. Dong, PdM (M = Pt, Au) Bimetallic Alloy Nanowires with Enhanced Electrocatalytic Activity for Electro-oxidation of Small Molecules, *Adv. Mater.* 24 (2012) 2326-2331. <https://doi.org/10.1002/adma.201104951>
46. S. R. Bharadwaj, A. S. Kerkar, S. N. Tripathi, S. R. Dharwadkar, The palladium-platinum phase diagram, *Journal of the Less-Common Metals*, 169 (1991) 167. [https://doi.org/10.1016/0022-5088\(91\)90245-Y](https://doi.org/10.1016/0022-5088(91)90245-Y)
47. V. Torrisi, M. Censabella, G. Piccitto, G. Compagnini, M. G. Grimaldi, F. Ruffino, Characteristics of Pd and Pt Nanoparticles Produced by Nanosecond Laser Irradiations of Thin Films Deposited on Topographically-Structured Transparent Conductive Oxides, *Coatings*, 8 (2018) 68. <https://doi.org/10.3390/coatings9020068>

48. F. Font, S. Afkhami, L. Kondic, Substrate melting during laser heating of nanoscale metal films, *Int. J. Heat Mass Transf.*, 113(2017) 237–245. <https://doi.org/10.1016/j.ijheatmasstransfer.2017.05.072>
49. C. Poulhier, D. S. Smith, J. Absi, Thermal conductivity of pressed powder compacts: Tin oxide and alumina, *J. Eur. Ceram. Soc.*, 27 (2007) 475–478. <https://doi.org/10.1016/j.jeurceramsoc.2006.04.068>
50. S. J. Henley, J. D. Carey, S. R. P. Silva, Pulsed-laser-induced nanoscale island formation in thin metal-on-oxide films, *Physical Review B*, 72 (2005) 195408-195417. DOI:10.1103/physrevb.72.195408
51. F. Ruffino, I. Crupi, A. Irrera, M. G. Grimaldi, Pd/Au/SiC Nanostructured Diodes for Nanoelectronics: Room Temperature Electrical Properties, *IEEE Trans. Nanotechnol.*, 9 (2010) 414-421. DOI: 10.1109/TNANO.2009.2033270
52. J. A. Venables, G. D. Spiller, M. Hanbücken, Nucleation and growth of thin films, *Rep. Prog. Phys.*, 47 (1984) 399-459. <https://doi.org/10.1088/0034-4885/47/4/002>
53. F. Ruffino, M. G. Grimaldi, Island-to-percolation transition during the room-temperature growth of sputtered nanoscale Pd films on hexagonal SiC, *J. Appl. Phys.*, 107 (2010) 074301. <https://doi.org/10.1063/1.3361321>
54. L. Zhang, F. Cosandey, R. Persaud, T. E. Madey, Initial growth and morphology of thin Au films on TiO₂(110), *Surf. Sci.*, 439 (1999) 73-85. [https://doi.org/10.1016/S0039-6028\(99\)00734-7](https://doi.org/10.1016/S0039-6028(99)00734-7)
55. E. Owusu-Ansah, C. A. Horwood, H. A. El-Sayed, V. I. Birss, Y. J. Shi, A method for the formation of Pt metal nanoparticles using nanosecond pulsed laser dewetting, *Appl. Phys. Lett.*, 106 (2015) 203103. <https://doi.org/10.1063/1.4921528>
56. A. L. Giermann, C. V. Thompson, Solid-state dewetting for ordered arrays of crystallographically oriented metal particles, *Appl. Phys. Lett.* 86 (2005) 121903. DOI: 10.1063/1.1885180

Chapter 3

Laser ablation synthesis of Pd and Pt nanoparticles and study of the charge transfer effect in NPs/Graphene hybrid composites

In the first chapter has been explained how physico-chemical response of metallic nanoparticles can be tuned by controlling their size and composition. In particular, it is known in the literature that catalytic activity of metallic nanoparticles increases when their size decreases, because the surface area of nanoparticles is inversely proportional to the particle size [1-3]. Therefore, it is important that the fabrication methods allow such a fine control.

In the previous chapter, a method based on laser irradiation was shown, which it allowed us to fabricate mono and bimetallic nanoparticles with size > 50 nm (depending on the thickness of the irradiated film).

Here I present a laser-assisted synthesis method for the production of ligand-free mono- and bi-metallic Pd and Pt nanoparticles, with nanoparticles' average diameter around 10-15 nm. It is based on the nanosecond Pulsed Laser Ablation in Liquid environment (PLAL) of pure Pd or Pt targets and of PtPd composite target at different ablation times, in which the composition of the target determines the composition of the resulting NPs [4, 5].

Some of the work described in this chapter has been previously published as:

¹ M. Censabella, V. Torrisi, S. Boninelli, C. Bongiorno, M. G. Grimaldi, F. Ruffino, Laser ablation synthesis of mono- and bimetallic Pt and Pd nanoparticles and fabrication of Pt-Pd/Graphene nanocomposites, 475 (2019) 494-503. <https://doi.org/10.1016/j.apsusc.2019.01.029>

In addition, I used the produced nanoparticles to decorate graphene layers by simple spin-coating of the colloidal solutions onto the substrates, obtaining NPs/graphene nanocomposites. Indeed, such hybrid composites are considered promising candidates for the design and production of innovative and functional devices, thanks to the properties arising from the synergistic combination of the characteristics of both components.

Furthermore, a study on the charge transfer effect between nanoparticles and graphene is here presented.

3.1 Experimental section

- *Synthesis of colloidal NPs*

Laser ablation was performed by pulsed (10 ns) Nd:YAG Laser operating at $\lambda = 1064$ nm, at fluence 5 J/cm^2 and at repetition rate of 10 Hz, with 6 W of power (Quanta-ray PRO-Series pulsed Nd:YAG laser). As shown in figure 3.1, the beam laser was focused perpendicularly aligned to the target by means of a lens of 20 cm focal length. The target was placed at the bottom of a teflon vessel that was filled with 8 mL of deionized Milli-Q water (resistivity $18 \text{ M}\Omega \text{ cm}$). The spot laser has a circular shape of 2 mm in diameter.

In order to synthesize Pt NPs a pure platinum metal plate was used as target, with purity of 99,9 % and for the production of Pd NPs a pure palladium metal plate was used as target, with purity of 99,9 %. Instead, bimetallic PtPd NPs were produced by laser ablation of a composite target $\text{Pt}_{80}\text{Pd}_{20}$ (at. %).

Three sets of samples were prepared for each target, by changing the ablation times: 2, 8 and 12 minutes.

The targets have been weighed before and after the ablation using a micro analytical balance (Sartorius M5) with a sensitivity of $100 \mu\text{g}$, in order to estimate the total amount of material released in the solution. During the irradiation of the target, the solution's color becomes brown.

All the solutions have been kept in the fridge at 3°C to prevent the NPs agglomeration [4].

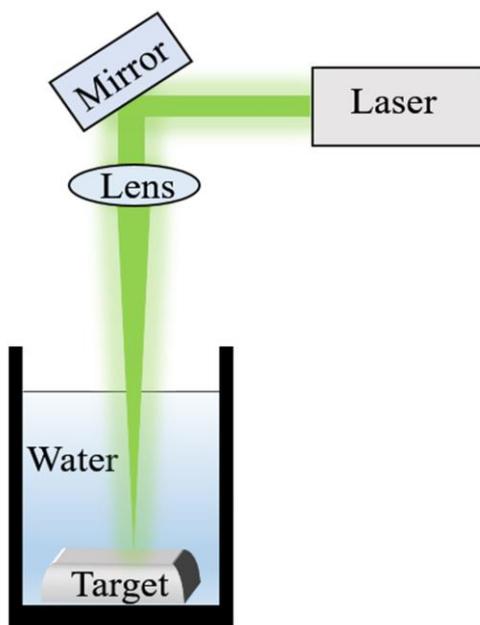


Figure 3.1 Schematic of experimental setup employed for the synthesis of colloidal NPs [6].

- *Characterizations of metallic NPs*

The as-produced colloids were analyzed by Ultraviolet-Visible spectroscopy (UV-Vis) using a Perkin-Elmer Lambda40 spectrometer in the wavelength range 200–1100 nm with an integrating sphere (Labsphere 20), using quartz cells with 1 cm light path.

In order to study the NPs morphology by using Transmission Electron Microscopy (TEM), a drop of synthesized colloidal solutions, for each sample, has been casted on TEM grid and left drying in air. The TEM images were taken by employing a 2010 JEOL instrument operating at 200 KeV accelerating voltage and the images were analyzed by Gatan Digital Micrograph software to determine the NPs size distribution. The mean value of the NPs diameter, $\langle D \rangle$, for each sample has been calculated on a statistical

population of 900 particles, with associated error the standard deviation on the mean value.

Also, High-Angle Annular Dark Field Scanning Transmission Electron Microscopy (HAADF-STEM) images were obtained by STEM. The HAADF images were registered using a camera length of 120 mm and a collection angle of 50 - 180 mrad.

Energy Dispersive X-ray (EDX) analyses were performed using a Gemini Field Emission SEM (FE-SEM) Carl Zeiss SUPRA 25, equipped with an EDAX EDX detector.

Moreover, the crystalline structure of the NPs was checked by using the Selected Area Electron Diffraction (SAED) technique in TEM.

Also, a drop of colloidal solutions for each sample has been casted on silicon substrate in order to perform XRD characterization. The NPs' structure was analyzed in grazing incidence mode ($\theta_{inc} = 0.1^\circ$) using a Smartlab Rigaku diffractometer, equipped with a rotating anode of Cu K_α radiation ($\lambda=1.54056 \text{ \AA}$) operating at 45 kV and 200 mA.

- ***Synthesis of NPs/Graphene nanocomposites***

Graphene substrates, produced via Chemical Vapor Deposition (CVD) method, were purchased from Graphene Laboratories (NY, USA, graphene-supermarket.com). Graphene was grown directly on nickel film deposited on an oxidized silicon wafer.

In order to fabricate NPs/Graphene nanocomposite a drop of colloidal solutions for each sample has been casted and spin-coated onto graphene substrate.

- ***Characterization of NPs/Graphene nanocomposites***

The morphology of NPs/Graphene nanocomposite was characterized by SEM, using a Zeiss FEG-SEM Supra 25 Microscope operating at 5 kV and the resulting SEM images were analyzed using the Gatan Digital Micrograph software in order to estimate the surface density of the nanoparticles on the graphene.

Raman spectra on the samples were acquired by using a micro-Raman spectrometer (Confocal Raman–AFM SNOM, WITec ALPHA300RS, ULM, Germany) equipped with a charge-coupled device (CCD) system. A 532 nm laser line (output power ~ 32 mW, power on the sample ranging from 0.5 to 10 mW), a grating with 600 grooves mm^{-1} and a 100 \times differential interference contrast (DIC) objective (NA 0.9) were used. Several Raman spectra (10–15 for each sample) of bare graphene and nanocomposites were collected to ensure the repeatability of the results and in order to calculate the error in the peak values. In addition, the spectra for different sample are acquired in areas with the same contrast at optical microscope, in order to guarantee similar number of layers, between 2 and 3 [7].

The AFM image and the current–voltage (I–V) characteristics of the samples were acquired, at room-temperature, by C-AFM (Conductive-Atomic Force Microscopy) using a Bruker-Innova microscope, in contact mode, equipped with a current amplifier and ultra-sharpened Pt tips (SCM-PIT by Bruker probes, radius of curvature = 20 nm). For each sample, at least 100 C-AFM I–V characteristics were acquired in 100 different points on the sample surface. The AFM image have been taken in scanning areas of $5 \times 5 \mu\text{m}^2$, in order to ensure punctual measurements on NP and Out of NP on the same number of graphene layers.

3.2 Synthesis by pulsed laser ablation in liquid of mono and bimetallic Pt/Pd nanoparticles

Here I report a facile synthesis of monometallic and bimetallic PtPd NPs by PLAL. A complete characterization of the produced nanoparticles is also presented. In particular, it has been characterized their stability, morphology and crystalline structure.

3.2.1 Results and discussion

- **Monometallic NPs**

In figure 3.2 a)-c) are shown the Pt colloidal solutions obtained by changing the ablation times: 2 a), 8 b) and 12 c) minutes.

Instead, Pd solutions ablated for 2 (2'), 8 (8') and 12 minutes (12') are shown in figure 3.2.d), e) and f), respectively. But after few minutes, in the 8' (fig. 3.2.h) and 12' (fig. 3.2.i) Pd solutions the NPs aggregates formation and the sedimentation take place. On the contrary, 2'-Pd (fig. 3.2.g) and all Pt colloidal solutions seem to remain stable.

Figure 3.2.j) shows the solution density [g/L] as a function of ablation time of the colloidal stable solutions, calculated weighing the targets before and after ablation and assuming that ablated material has been totally converted in nanoparticles. The dashed line is only a guide for the eye.

In order to evaluate the colloids' stability over time, in addition to the visual evidence shown in figure 3.2, UV-Vis extinction spectra were carried out immediately after the ablation process and 5 days after the production stage.

The extinction spectra (absorbance + scattering) indicate that the surface plasmon resonance band of these samples appeared in the UV region at 216 nm (fig.3.3.a for PtNPs) and 218 nm (fig 3.3.b for Pd NPs) wavelength. These values are in good agreement with other work in literature [8, 9].

As shown in figure 3.3.a) and 3.3.b), the spectra acquired immediately after the nanoparticles production and after 5 days seem to be identical, within an error of 5%. This is true both for colloids with PtNPs than Pd 2' NPs. For Pt NPs is reported only Pt 2' solution's spectrum as example, because the others spectra are identical to the latter.

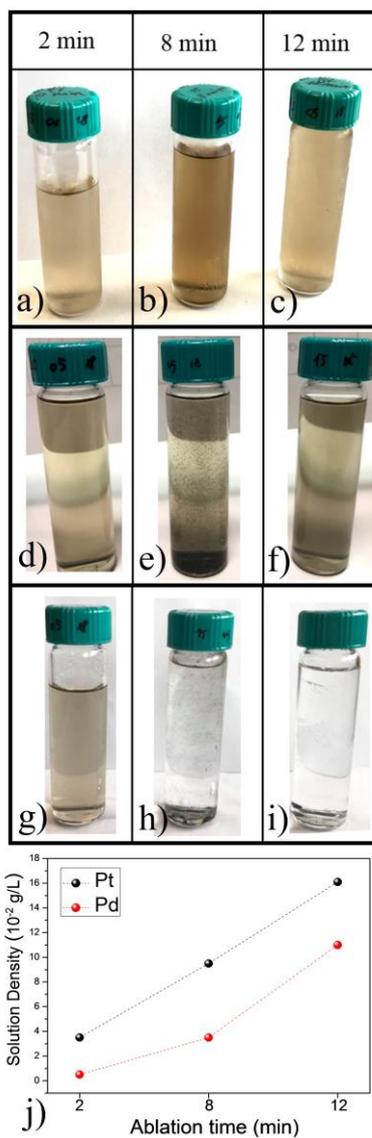


Figure 3.2 Pictures of colloidal solutions obtained by Pt target ablation for 2 (3.2.a), 8 (3.2.b) and 12 (3.2.c) minutes and Pd target ablation for 2 (3.2.d), 8 (3.2.e) and 12 (3.2.f) minutes. After few hours Pt solutions and Pd 2' (3.2.g) solution are still stable, instead Pd solutions 8' (3.2.h) and 12' (3.2.i) aggregated. Solution densities of ablated masses as a function of ablation time (3.2.j) [6].

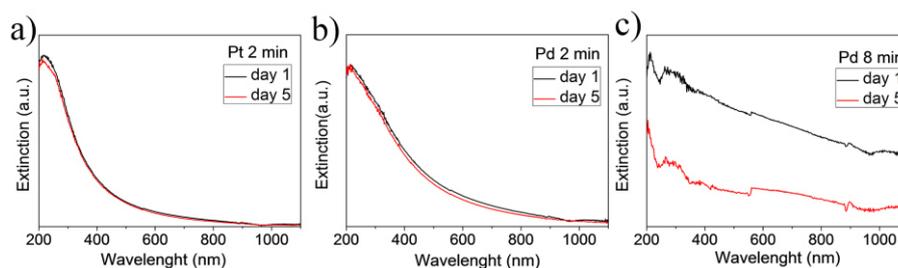


Figure 3.3 UV-Vis Extinction spectra of laser synthesized colloidal NPs immediately after the ablation process and after 5 days the production stage. In particular, Pt 2' NPs 3.3.a), Pd 2' NPs 3.3.b) and Pd 8' NPs [6].

Instead, I report in figure 3.3.c) the extinction spectra of Pd 8' solution acquired immediately after the nanoparticles production and after 5 days. As recognizable by the picture, the spectra are completely different compared to Pd 2'solution, because, just after a few minutes from their production, sedimentation takes place. So, I can affirm that the solutions obtained for 8 and 12 minutes of ablation time are not stable. This, probably, because the solution density of ablated material is high, determining the formation of very concentrated solutions and, in the same volume, the particle-particle distance decreases. The decrease of this distance causes, for the palladium particles, an increase of the attractive interaction that lead to the aggregation of the NPs and the subsequent sedimentation. This effect is not realized for Pt NPs, although by increasing the concentration and thus decreasing the distance, evidently the attractive forces between Pt NPs does not become so large as to cause particles' aggregation.

Thus, through laser ablation of a target of Pt at three different ablation times, I obtained stable Pt NPs and after laser ablation for 2 minutes of ablation time of a Pd target, I obtained stable Pd NPs. I have verified the stability after 5 days from their production, but as evidenced by Mafunè [8] and Cristoforetti [9], Pt and Pd NPs are stable for many days (>30 days).

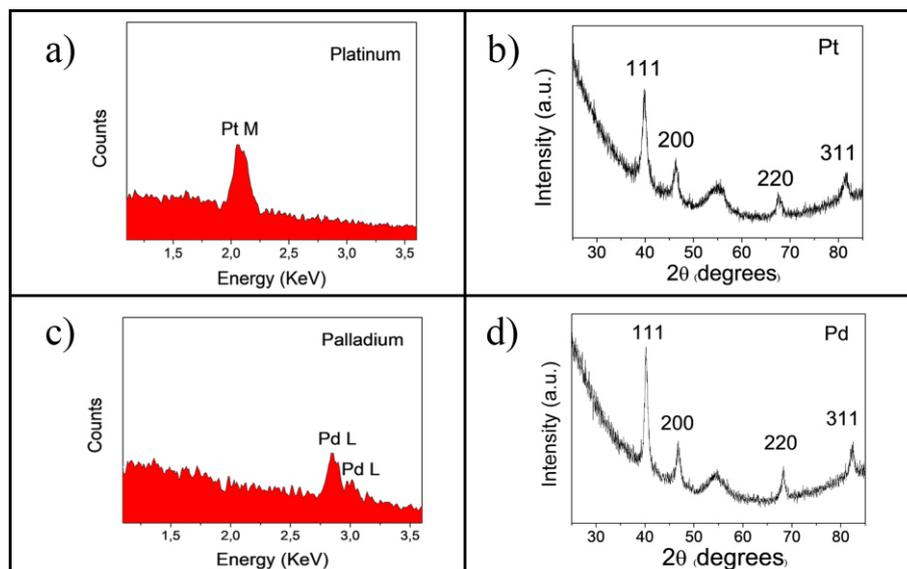


Figure 3.4 EDX spectrum a) and XRD pattern b) of Pt NPs and EDX spectrum c) and XRD pattern d) of Pd NPs [6].

EDX analyses on single NPs are shown in Figure 3.4.a) and 3.4.c). In particular, Figure 3.4.a) shows EDX analysis on a single Pt NP obtained by 12 minutes of ablation time, where is evident the presence of the Pt peak at 2.048 keV (Pt shell M). Instead, Figure 3.4.c) displays EDX analysis on a single Pd NP resulting by 2 minutes of ablation time, in which the two main Pd peaks were present at 2.838 keV ($L\alpha$) and 2.990 keV ($L\beta_1$).

XRD measurements on the colloidal solutions were performed in order to study the crystalline structure of the NPs. So, a drop of Pt and Pd colloidal solution obtained by 8' of ablation time have been casted on silicon substrate and the drop complete evaporation was observed in 24 hours in standard conditions (in air and room-temperature). XRD patterns of Pt NPs is shown in Figure 3.4.b), where there are four diffraction peaks at $39,8^\circ$ (111), $46,4^\circ$ (200), $67,6^\circ$ (220) and $81,5^\circ$ (311). Instead, Figure 3.4.d) shows Pd NPs diffraction peaks at $40,2^\circ$ (111), $46,8^\circ$ (200), $68,3^\circ$ (220) and $82,3^\circ$ (311). The XRD peaks match those of fcc Pt (JCPDF 04-0802) and Pd (JCPDF 46-1043), respectively.

The average size of the crystalline domain that induced the diffraction has been estimated from the XRD spectra by using the Debye–Scherrer approximation: $D = K \lambda / \beta \cos\theta$, where K is a dimensionless shape factor close to unity, λ is the X-ray wavelength (Cu K α radiation $\lambda=1540,56 \text{ \AA}$), β is the line broadening at half the maximum intensity and θ is the Bragg angle. This value is 7 nm for Pt NPs and 12 nm for Pd NPs [10].

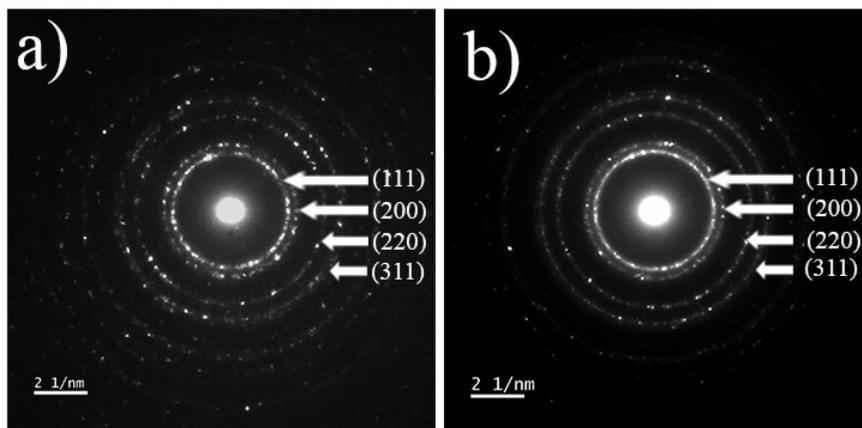


Figure 3.5 SAED pattern of Pt 2' NPs 3.5.a) and Pd 2' NPs 3.5.b). The diffraction rings correspond to d-spacing, that refer to the (111), (200), (220) and (311) planes of face-centered cubic structure of Pt and Pd metal, respectively [6].

In addition to the XRD measurements, the crystalline structure of the nanoparticles is confirmed by SAED measurements, showed in figure 3.5. In particular, in figure 3.5.a the diffraction rings correspond to d-spacing of 2.27, 1.96, 1.39, 1.19 \AA . In figure 3.5.b the diffraction rings correspond to d-spacing of 2.24, 1.94, 1.37, 1.17 \AA . These values refer to the (111), (200), (220) and (311) planes of face-centered cubic structure of Pt (fig. 3.5.a) and Pd (fig 3.5.b) metal, respectively

Figure 3.6.a) is a TEM image of Pt NPs obtained by ablation for 2 minutes, which shows that the NPs present a circular plan-view shape indicating a three-dimensional spherical shape. The particles' diameter has been measured by TEM image and size distribution for Pt 2' NPs is shown in fig. 3.6.b). Most

of particles are in the order of 5-10 nm, but there are also smaller and bigger NPs.

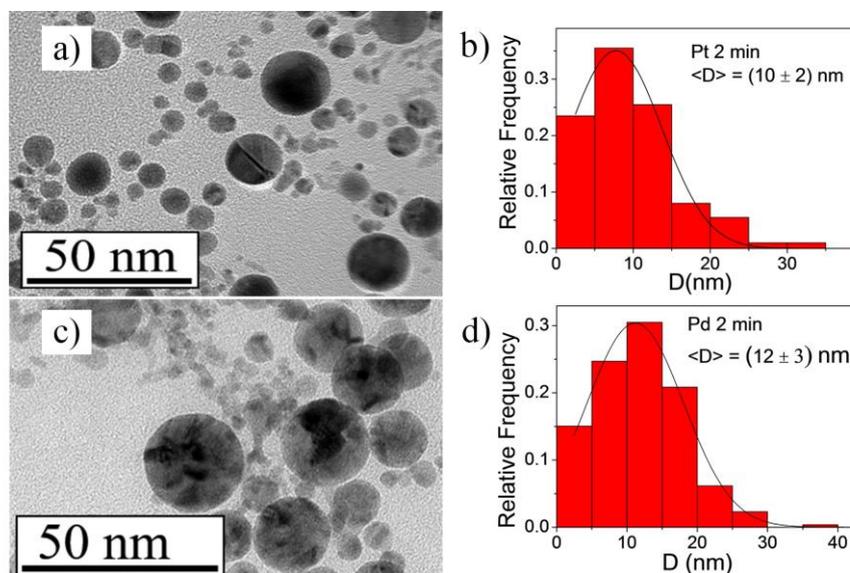


Figure 3.6 TEM image 3.6.a) of Pt 2' NPs and their diameters distribution 3.6.b). TEM image 3.6.c) of Pd 2' NPs and their diameters distribution 3.6.d) [6].

Also Pd NPs have spherical shape, as shown in TEM image of Pd 2' NPs, in figure 3.6.c). The diameter distribution (fig. 3.6.d) shows that the mean value is around 12 nm.

The mean diameter histogram is displayed in figure 3.7. The mean value is evaluated by Gaussian distribution (black line in fig. 3.6.b and 3.6.d) and the associated error is the standard deviation on the mean value. In particular, the evaluated mean values and corresponding errors for the analyzed samples are reported in the plot in Fig. 3.7.

These values are close to the crystalline size valuated by Scherrer equation and this is a clear evidence that the NPs are, basically, single crystals [5].

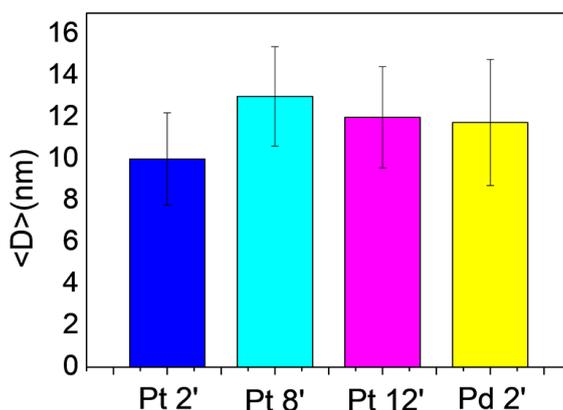


Figure 3.7 Mean diameters of monometallic NPs [6].

The effect of the ablation time is not very strong, indeed the average particles size changes of few nanometers. The particles become larger with increasing ablation time until the high repetition of the pulsed laser cause downsizing by laser fragmentation during laser ablation [4].

However, as demonstrated in previous literature, there are other multiple strategies suitable for varying the particle sizes produced by laser ablation. These strategies are: to change the laser energy and the lens-to-sample distance, in order to change the laser spot' size onto the target and, consequently, the laser fluence [9]. Also, the solvent used can greatly influence the ablation process, for example by reducing the size of the nanoparticles due to an adsorption by solvent's molecules on the particle surface [4].

- **Bimetallic NPs**

In order to produce bimetallic NPs, a composite target made by eighty atomic percent of Pt and twenty atomic percent of Pd was ablated. Again, the ablation times were 2, 8 and 12 minutes.

An optical image (photo) of the resulting colloidal solutions is displayed in figure 3.8 a-c). After several days the solutions appear still stable (fig. 3.8 d-f), as in the case of the Pt NPs solutions.

The solution density [g/L] of the stable solutions (monometallic and bimetallic NPs) is shown in figure 3.8.g). Also in this case of bimetallic NPs (blue line), assuming that ablated material has been totally converted in nanoparticles.

For evaluate the colloids' stability over time, UV-Vis extinction spectra were carried out immediately after the ablation process and 5 days after the production stage.

The extinction spectra indicate that the surface plasmon resonance band of these samples appeared in the UV region at 222 nm wavelength. As shown in figure 3.9, the spectrum acquired immediately after the nanoparticles production and after 5 days seem to be identical, within an error of 6%. The stability of bimetallic PtPd nanoparticles is explained by the fact that the ablated target is made by 80% of Pt and 20% of Pd. Only PtPd 2' solution's extinction spectrum is reported as example.

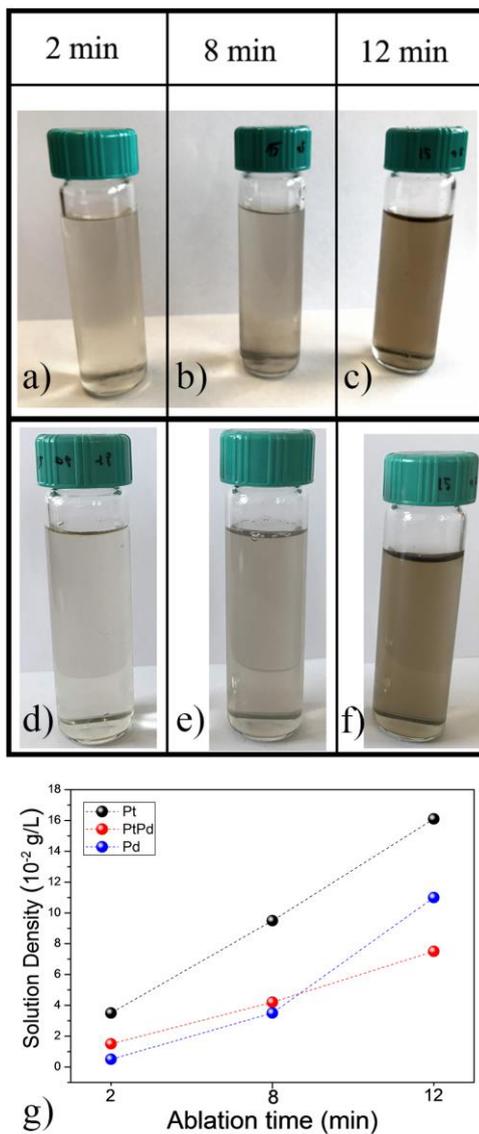


Figure 3.8 Photographs of colloidal solutions obtained by ablating a composite target $\text{Pt}_{80}\text{Pd}_{20}$ (at. %), for 2 (3.8.a), 8 (3.8.b) and 12 (3.8.c) minutes. Optical images (3.8.d-f) of solutions after several days. Solution densities of ablated masses as a function of ablation time [6].

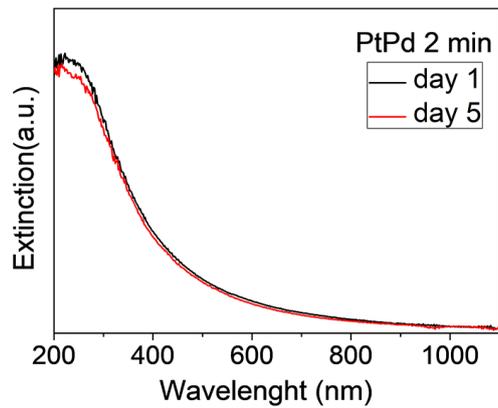


Figure 3.9 UV-Vis Extinction spectra of laser synthesized colloidal bimetallic PtPd NPs immediately after the ablation process and after 5 days the production stage [6].

Figure 3.10 shows EDX analysis performed on a single NP resulting by 8 minutes of ablation. In particular, the simultaneous presence of the Pt peak at 2.048 keV (Pt shell M) and of the two main Pd peaks at 2.838 keV (Pd shell $L\alpha$) and 2.990 keV (Pd shell $L\beta_1$) (see fig. 3.10.b) were found, indicating that the NP truly a bimetallic PtPd structure.

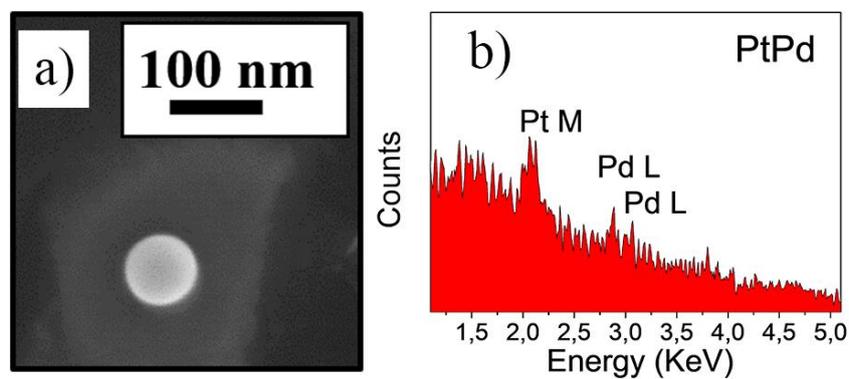


Figure 3.10 SEM image (a) and EDX spectrum (b) of a single NP obtained by laser ablation of a composite target PtPd for 8 minutes. The presence of the characteristic peaks of Pt (2.048 keV) and Pd (2.838 keV and 2.990 keV) is evident [6].

HAADF-STEM measurements on the bimetallic PtPd NPs were performed after deposition on the TEM grid from the starting solutions. These analyses were carried out to determine whether the NPs consisted of a homogeneous PtPd alloy or if Pd and Pt in the same NP, even if simultaneously present, are spatially separated as, for example, in a core-shell structure. Indeed, in the HAADF-STEM images the contrast is related with the atomic number Z of the elements in the samples (Z -contrast), so, the lighter elements appear lackluster while the heavier elements appear brighter [11-13]. In this case, the difference between the atomic number of the elements Pd ($Z=46$) and Pt ($Z=78$) should be clearly distinguishable in the contrast of the image. However, as you can see in the figure 3.11, no difference can be observed between the Pt and Pd elements in a single nanoparticle obtained by laser ablation for 8 minutes. Furthermore, whereas the STEM images are due to the mass contrast, I compared 2 nanoparticles with different image contrast to 2 other nanoparticles with equal size (in which, therefore, the mass volumes crossed by the beam are comparable): in particular, in figure 3.11, NP called "a" (very bright) with diameter size about $D=41$ nm and the one called "c" (less bright) with diameter $D=21$ nm can be compared, respectively, with the NP called "b" ($D=40$ nm) and "d" ($D=21$ nm). Also in this case, there are no significant contrast differences between "a" and "c" and between "b" and "d". In fact, the two particles in comparison are brilliant in the same way and, therefore, have the same elemental composition.

So I can affirm that the NPs are bimetallic PtPd, as observed in the EDX measurements, and, thanks to HAADF STEM measurements, that Pt and Pd are homogeneously distributed on the whole volume of the particles and that, therefore, there is no phase separation between the two elements.

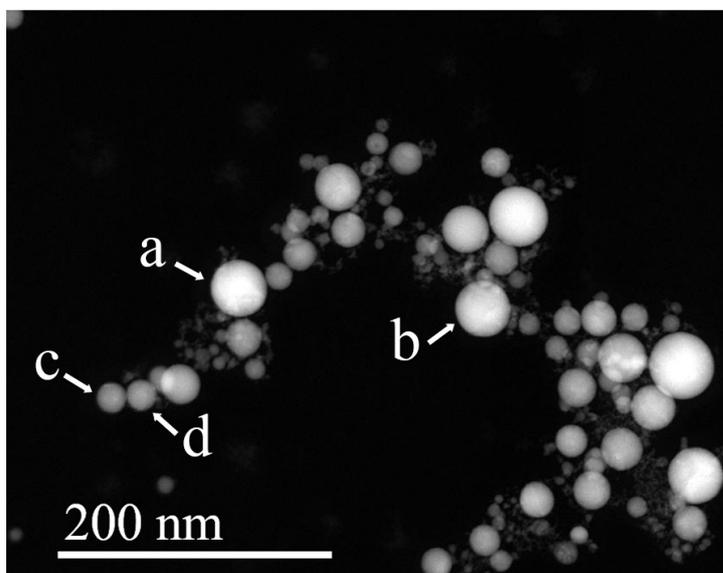


Figure 3.11 HAADF STEM image of bimetallic PtPd NPs obtained by laser ablation for 8 minutes. The nanoparticle called “a” has the same diameter and the same contrast of the nanoparticle “b”, as well as the nanoparticle “c” has the same contrast and size of nanoparticle “d”. Therefore, Pt and Pd are homogeneously distributed on the whole volume of the particles [6].

Moreover, the NPs’ crystalline structure is confirmed by SAED measurements, showed in figure 3.12. The diffraction rings correspond to d-spacing of 2.25, 1.95, 1.39, 1.19 Å. These values are within the monometallic Pt and Pd values, thus indicating the formation of PtPd alloy [14].

As shown in the previous figures the bimetallic NPs are spherical. The PtPd particles’ size has been measured by TEM images. Figure 3.13 shows a TEM image (fig. 3.13.a) and size distribution (fig. 3.13.b) of PtPd bimetallic NPs obtained by ablation for 2’. Most of particles are in the order of 1-10 nm, but there are, also, many bigger NPs.

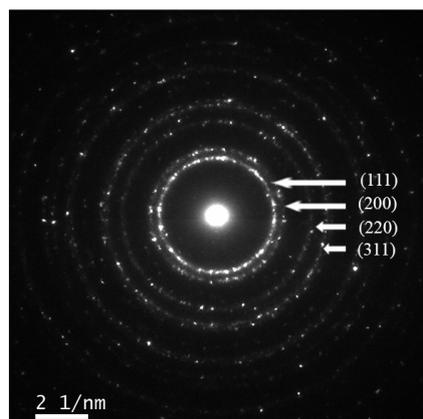


Figure 3.12 SAED pattern of PtPd 2' NPs. The diffraction rings correspond to d-spacing, that refer to the (111), (200), (220) and (311) planes of structure of PtPd alloy [6].

The mean diameters, $\langle D \rangle$, of the NPs are shown in figure 3.14. In this case, the mean value is evaluated by LogNormal distribution (black line in fig. 3.13.b) and the associated error is the standard deviation on the mean value.

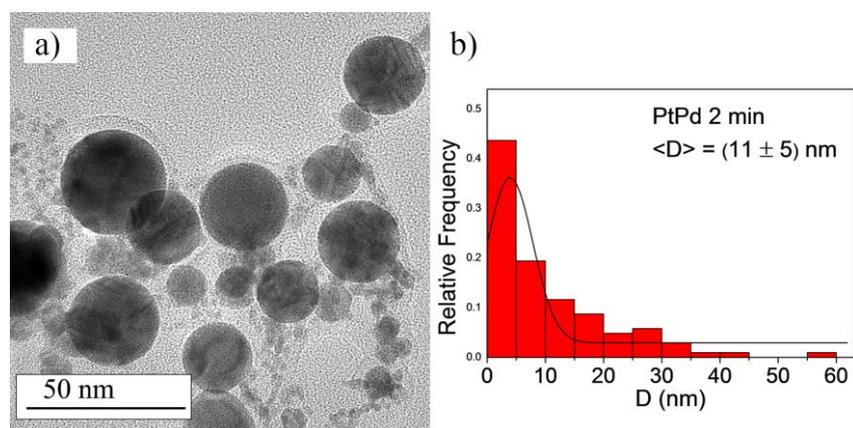


Figure 3.13 TEM image a) and diameter distribution b) of bimetallic PtPd NPs obtained by laser ablation of composite target for 2 minutes [6].

Again, the average particles size changes of few nanometers by changing the ablation times. Increasing ablation time, the particles become larger until the nanoparticles fragmentation occurs [4].

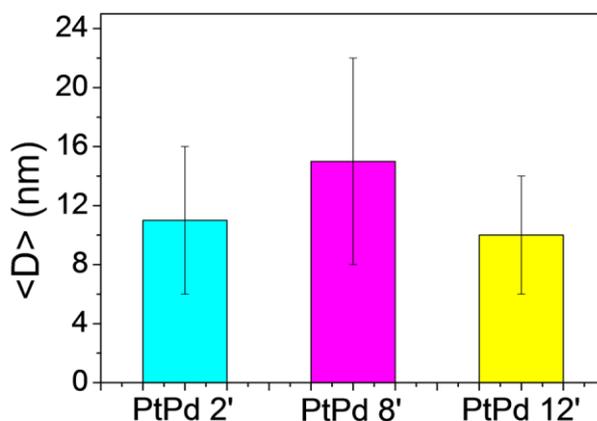


Figure 3.14 Mean diameter histogram of bimetallic PtPd NPs [6].

3.3 Study of the charge transfer effect in NPs/Graphene hybrid composites

Here we report a study on the charge transfer effect between metal NPs and graphene substrate. In particular, I wanted to investigate how chemical composition of NPs influences this effect. Therefore, the stable NPs of Pt, Pd and PtPd, produced by laser ablation for 2 minutes of ablation time, have been loaded on graphene by simple spin-coating of colloidal solution. Raman Spectroscopy and C-AFM measurements were performed on these NPs/graphene nanocomposites and a combined analysis of these results allowed us to demonstrate that the chemical composition of the metal nanoparticles is a key parameter in determining the charge transfer phenomenon.

3.3.1 Results and discussion

Graphene is a two-dimensional crystal, consisting of one-atom thick monolayer of sp^2 hybridized carbon atoms organized in a honeycomb lattice (fig. 3.15) [6]. For the first time, it was produced by oxidation and by carbon precipitation on metal catalysts in 1974 [15], but since its isolation by simple mechanical exfoliation of graphite in 2004 [16] it has attracted tremendous attention in the scientific community due to its exceptional proprieties [17]: it exhibits charge-carrier mobility up to $10^6 \text{ cm}^2 \text{ V}^{-1}$ at room temperature [18], electrical conductivity of up to 6000 Scm^{-1} [19], thermal conductivity of $5000 \text{ Wm}^{-1}\text{K}^{-1}$ [20], optical transpance [21], large specific surface area [22] and mechanical strength (with a Young's modulus of 1 TPa single layer graphene is the strongest material ever measured [23]). These properties make it promising for a variety of exciting application.

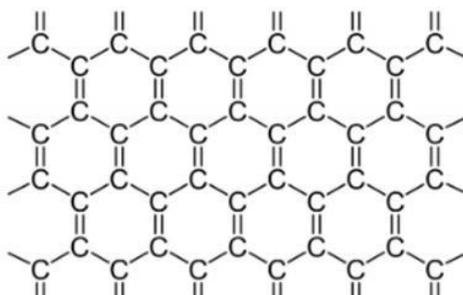


Figure 3.15 A single layer of carbon atoms arranged in such a honeycomb structure.

In particular, the novel optoelectronic, catalytic and magnetic properties of graphene/metal NPs nanocomposites have attracted great attention. In fact, due to sp^2 hybridization of carbon bonds present in graphene, which facilitates the delocalization of electrons, graphene possesses excellent electronic conduction, that could be enhanced loading metal NPs on graphene, combining the properties of both components. This can lead to a nanocomposite with larger active surface areas and improved electron transport useful for various applications including catalytic reactions,

electronic and optical devices, energy storage and energy conversion [6,17,22].

In this work, graphene grown by CVD on Ni has been used as substrate to load the NPs. Figure 3.16 is a SEM image of the used graphene. Graphene was purchased from graphene-supermarket and has the following technical characteristics [24]: it is a polycrystalline film of few layers graphene of different thickness, usually between 1-7 layers with an average of 4 monolayer thickness; as show in figure 3.16.a, graphene looks like a patchwork, whereas each “patch” has a different thickness, about 3-10 microns; the graphene layers within the same patch are aligned relative to each other (there is a graphitic AB-stacking order) [24]. Figure 3.16.b is an enlargement of fig. 3.16.a.

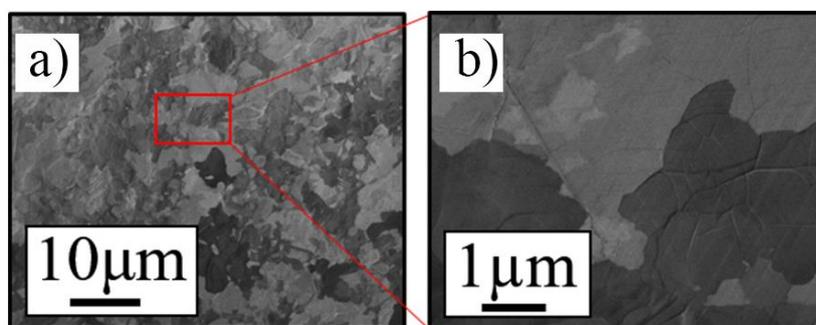


Figure 3.16 SEM image of multilayer graphene film grown on nickel (3.16.a). Figure 3.16.b is an enlargement of fig. 3.16.a [6].

In literature, many efforts have been devoted to study the interaction between graphene and metal surfaces. The adsorption between nanoparticles and graphene could be classified into two different categories: either a chemisorption, with strong interaction between graphene and metals and orbital hybridization, or a physisorption, with weak interaction and charge transfer. In the first case the adsorption energies are around 0.09-0.4 eV per atom and with equilibrium interfacial distances $< 2.5 \text{ \AA}$. For physisorption the adsorption energies are smaller at around 0.03-0.05 eV per atom carbon with equilibrium interfacial distances $> 3 \text{ \AA}$ [25].

In order to have strong bonds, for example covalent bonds, the functionalization of both graphene and nanoparticles is required. Thus, it is necessary to use surfactants such as polyvinylpyrrolidone [26,27] or reductants such as N_2H_4 [28] and $NaBH_4$ [29,30]. But the use of these additives often requires multiple steps and makes the synthesis and the purification complex.

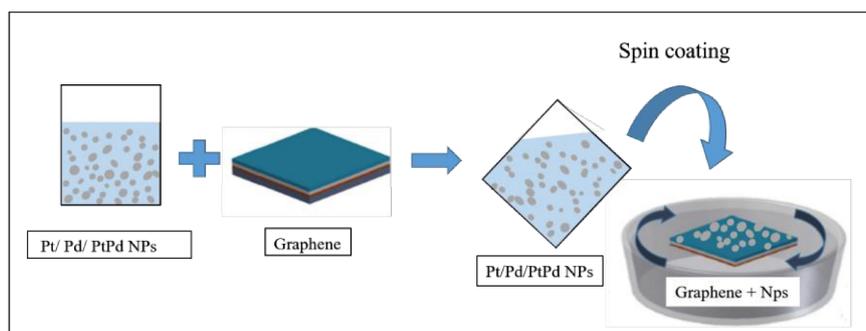


Figure 3.17 Schematic representation of the fabrication of NPs/graphene nanocomposites. A drop of colloidal solution has been casted and spin coated onto graphene substrate.

To reduce the complexity of the system, I used pure and ligand-free nanoparticles produced by PLAL. The NPs were used to decorate graphene by simple spin-coating of the colloidal solutions onto substrates, as schematized in fig.3.17. This can only be considered a mixture, in which, between nanoparticles and graphene, there is physisorption and therefore only weak bonds, such as van der Waals forces.

The surface morphology of the as-prepared NPs/graphene nanocomposite was characterized by SEM analysis. As seen from the high magnification SEM images in fig. 3.18.a-c, large quantities of NPs are dispersed on the surface of graphene. A structure presenting a “starry sky” type morphology is obtained. Several SEM images, for each sample, were analyzed to estimate the surface density of the nanoparticles on graphene, which is of the order of 10^{10} nanoparticles/cm², as displayed in fig.3.18.d.

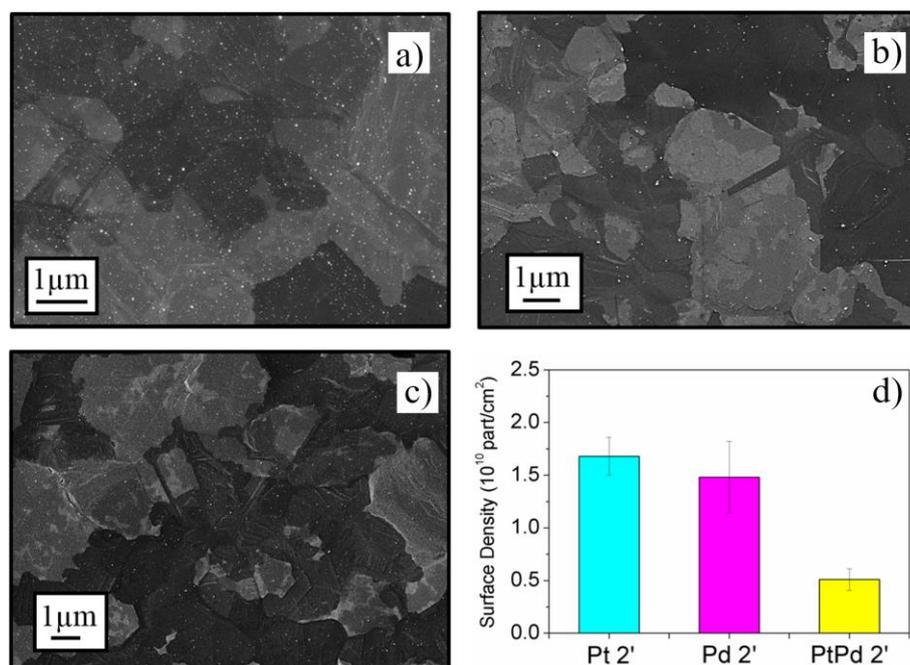


Figure 3.18 SEM images of metal NPs/graphene nanocomposites. In particular, Pt NPs on graphene in fig.3.18.a, Pd NPs/graphene in (b) and PtPd bimetallic NPs/Graphene in (c). Surface density of the NPs on graphene substrate (d) [17].

- **Charge Transfer in Graphene**

It is known in the literature that metallic films deposited on graphene modify the electronic structure of graphene, through charge transfer. So the Fermi Energy can move away from the conical points, resulting in doping with either electrons or holes [31-32]. A very useful technique to characterize the charge transfer effects of graphene-based systems is Raman spectroscopy. Indeed, the Raman spectrum of graphene contains information about both electronic properties and atomic structure [33]. It has three main peaks: the D-band, located at $\sim 1350\text{ cm}^{-1}$, G-band at $\sim 1582\text{ cm}^{-1}$ and 2D band at $\sim 2700\text{ cm}^{-1}$. The D-band appears in the case of microscopic defects in the graphene structure, but can also originate from chemical doping, grain boundaries or

other factors. The spectrum of defect-free graphene does not have a D band [34].

As reported by Das et al. [32], through the intensity ratio and the value shift of the G and 2D peaks of the graphene's Raman spectrum is possible to identify the graphene doping. Figure 3.19 shows how the Raman parameters (positions of the G (a) and 2D peak (b) and the 2D/G intensity ratio (c)) vary as a function of doping. In particular, the Raman shift of the G peak increases up to 30 cm^{-1} for hole doping and up to 25 cm^{-1} for electron doping; therefore, the presence of doping (hole or electron) determines an upshift of G peak [32]. Instead, the position of the 2D peak decreases (red shift) with increasing electron concentration in the system and increases (blue shift) with the increasing holes concentration. This allows the use of the 2D peak to discriminate between electron and hole doping. Moreover, in figure 3.19.c is shown the variation of the intensity ratio of the 2D and G peaks, $I(2D)/I(G)$: both in the presence of doping with holes or with electrons, this intensity ratio decreases.

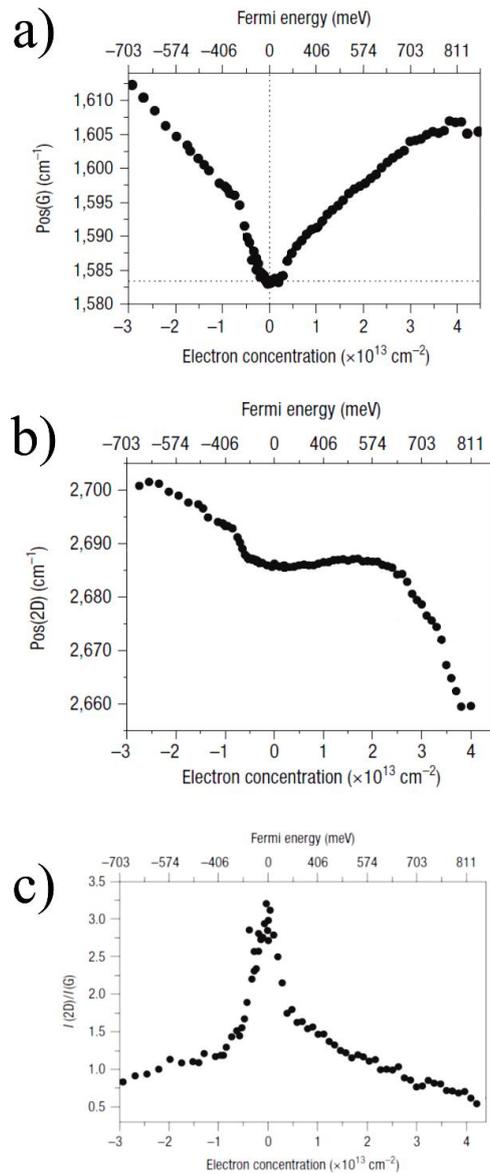


Figure 3.19 Position of the G a) and 2D peak b) as a function of the hole and electron doping. Ratio of the intensity of the 2D peak to the intensity of the G peak exhibits a dependence of the electron concentration [32].

The effect of the deposition of Pt films on pristine graphene was reported by Iqbal et al. [35]. In particular, thin layer of Pt with different thickness (1, 3 and 5 nm) were thermally evaporated on graphene single layer. The Raman spectra are shown in fig. 3.20: a change in the intensities of the G and 2D peaks are observed after the Pt coating. The $I(2D)/I(G)$ ratio becomes smaller with the increase in the thickness of the deposited film. Also, the 2D band is red-shifted and the G band is up-shifted: as the thickness of the Pt film increases, the shift increases. The blue shift of the G band position and the red shift of the 2D band position indicate the n-doping of graphene caused by the deposition of the Pt film.

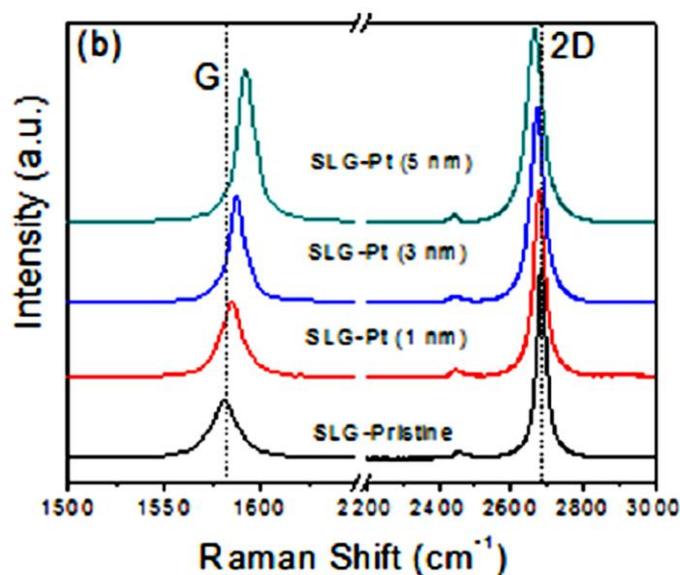


Figure 3.20 Raman spectra of pristine monolayer graphene before and after 1, 3 and 5 nm Pt deposition [35].

- ***Charge Transfer in Nps/Graphene nanocomposites***

I employed Raman spectroscopy on NPs/graphene nanocomposites in order to investigate the effect of the NPs elemental composition on the charge transfer phenomena.

In addition, the spectra for different sample are acquired in areas with the same contrast at optical microscope, in order to guarantee similar number of layers, between 2 and 3 [7]. In figure 3.21 are shown the Raman spectra in comparison. In particular, the G and 2D peak of the bare graphene (black line) are observed at 1579,9 and at 2699,4 cm^{-1} . The absence of D band suggests that graphene used is defect free. After decoration of NPs on graphene the D peak appears in all samples, because the presence of NPs alters the perfect structure of graphene pristine.

In addition, the G bands of Raman spectra of NPs/graphene samples are blue-shifted towards higher frequencies, while the 2D bands are red-shifted towards lower frequencies.

In particular, for Pt NPs/graphene (pink line) G band is upshifted by 4,95 cm^{-1} and 2D peak is shifted by 15,32 cm^{-1} from graphene, with peak values at 1587,34 cm^{-1} and 2684,08 cm^{-1} , respectively; in Pd NPs/graphene (green line) the G peak is at 1582,39 (upshifted by 2,49 cm^{-1}) and the 2D peak value is at 2688,37 cm^{-1} and shifted of 11,03 cm^{-1} ; graphene decorated with bimetallic PtPd NPs (blue line) has G peak at 1580,1 and 2D peak at 2691,14 cm^{-1} , with smallest peak shift: blue-shift by 0,2 cm^{-1} and red-shift by 8,26 cm^{-1} , respectively.

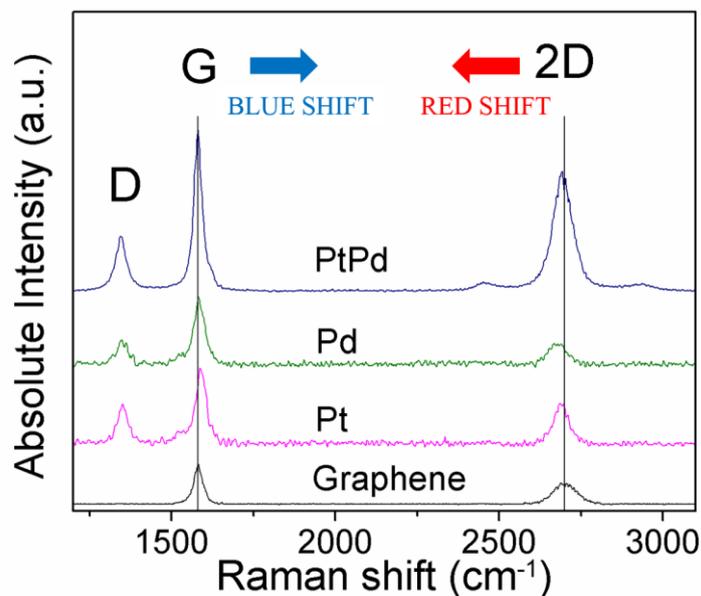


Figure 3.21 Raman spectra of graphene, Pt NPs/graphene, Pd NPs/graphene and PtPd NPs/graphene. A blue-shift of G peak and a red-shift of 2D peak of Raman spectra of metal NPs/graphene are evident. These shifts indicate an n-doping effect of the NPs on graphene [17].

More in detail, the figure 3.22 shows the histograms that highlight the differences between the different samples. In particular, fig. 3.22.a shows the ratio of $I(2D)/I(G)$, that is higher for Pt NPs/graphene sample and lower for PtPd NPs decoration. The G peak shift values (cm^{-1}) are displayed in fig. 3.22.b: the higher upshift value is obtained for Pt NPs/graphene sample instead the lower upshift is obtained for bimetallic PtPd NPs decoration. The same behavior has been obtained for 2D peak shift (cm^{-1}) displayed in fig. 3.22.c, in fact, the graphene's decoration with Pt NPs causes a bigger 2D peak shift, instead the bimetallic PtPd NPs decoration determines the smaller peak shift.

As shown in literature [31,32,35], the decrease of the $I(2D)/I(G)$ ratio and the blue-shift of G bands indicate that the NPs decoration cause a doping effect of the graphene layer and, in addition, the red-shift of the 2D bands indicate

an n-type doping, in which the electrons are transferred from metal NPs to the graphene layer. In particular, the more pronounced value peak shifts (G and 2D) in the Pt NPs/graphene samples correspond to a larger increase in electron density in the graphene layers. Instead, lower peak shift in the Pd NPs/graphene samples indicates, with respect to the Pt case, a lower increase in electron density in the graphene layers. Finally, the shift is much lower in the PdPt NPs/graphene samples, with respect to the Pt and Pd cases, indicating the lowest increase in electron density in the graphene layers [31].

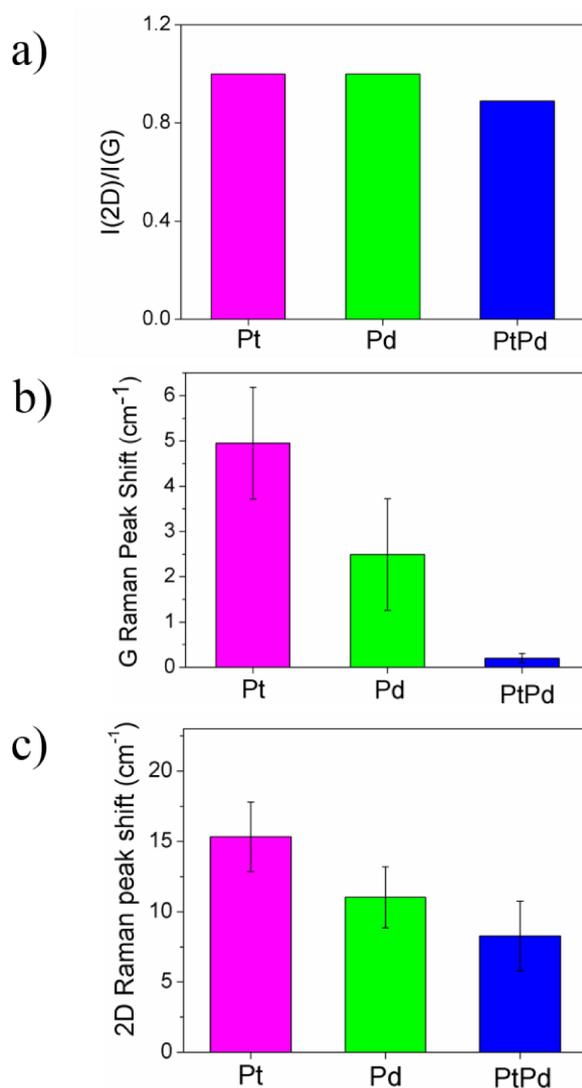


Figure 3.22 Histogram of I(2D)/I(G) intensity ratio (a), G peak shift (b) and 2D peak shift (c) of Raman spectra of metal NPs (Pt, Pd and PtPd NPs)/graphene composite.

In order to confirm this charge transfer effect, C-AFM was employed to probe, on the nanoscale, the electrical properties of the NPs/graphene samples.

A schematic representation of the experimental setup used is shown in the figure 3.23.

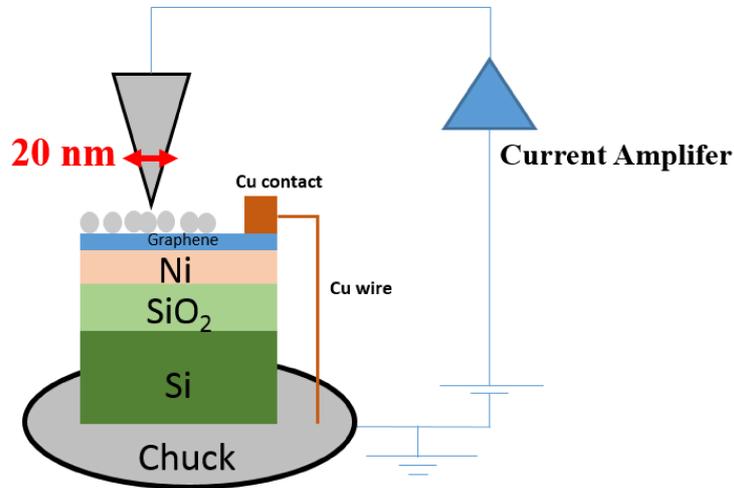


Figure 3.23 Schematic representation of experimental setup employed for C-AFM measurements.

Figure 3.24 shows AFM images and I-V characteristics acquired using the C-AFM methodology. In particular, in fig. 3.24.a is displayed AFM image (5 μm x 5 μm) of the Pt NPs/graphene sample, where agglomerates of NPs are evident on the surface of graphene. With nanometric resolution, C-AFM measurements are performed on one or few nanoparticles and on the substrate without particles. I observed that changing the acquisition point in the sample surface, on NPs and out of NPs (i. e. direct contact of the tip to graphene), the I-V characteristics change significantly. One of the 100 I-V acquired curves (randomly chosen) On (black line) and Out (red line) NPs is shown in fig. 3.24.b, where a change of the slope of the I-V characteristic is evident due to the effect of the NPs on graphene. Figure 3.24.c is an enlargement of the fig. 3.24.b, where, clearly, is possible to recognize the difference between the two different I-V. In the same way fig. 3.24.d, e, f and fig. 3.24.g, h, i are, respectively, AFM image and I-V characteristics of Pd NPs/graphene and PtPd NPs/graphene samples. We note that the I-V characteristics of the

different samples cannot be directly compared one with other, due to the likely different number of graphene layers which affects the absolute measured values for the current for a fixed voltage (for a fixed voltage, higher the number of graphene layers, lower the current). What is important, as result of the experiment, is the relative comparison of the I-V curves On the NPs and Out of the NPs, in this last case, however, in a random point within the same graphene patch where NPs were identified for the I-V measurements: in this way, I'm confident that, in each sample, the difference between the I-V curves obtained On NPs and Out of NPs is due, solely, to the presence/absence of the NPs since the number of the underlying graphene layers is the same. With this consideration, in particular, the relative change in the slope of I-V characteristic is more pronounced in the case of Pt NPs decoration. This is in agreement with the bigger G peak blue-shift and the 2D peak red-shift found in the Raman measurements displayed in fig. 3.22.b and 3.22.c. In order to evaluate the amount of the change in the slopes of I-V characteristics, in the three samples, the differences between measured current Out of NPs and On NPs ($\Delta I = \text{Current Out NP} - \text{Current On NP}$), fixing, for example, 10V, where the current values difference is larger, have been extracted and plotted in the histogram in fig. 3.25. In particular, this difference is more pronounced in the Pt NPs/graphene samples, where I found larger value shift in the Raman measurement. Finally, it is much lower in the PdPt NPs/graphene samples, where I found the lowest value shift in the Raman spectrum, with respect to the Pt and Pd cases.

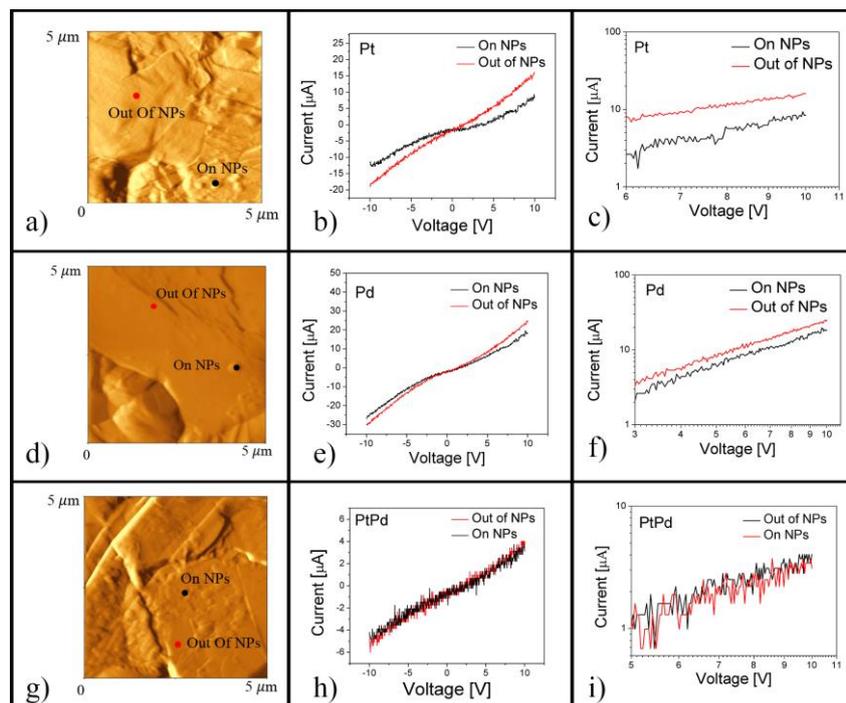


Figure 3.24 AFM image (a) and I-V characteristics (b) of Pt NPs/graphene nanocomposite; (c) is an enlargement of fig. (b). AFM image (d) and I-V characteristics (e) of Pd NPs/graphene nanocomposite; (f) is an enlargement of fig. (e). AFM image (g) and I-V characteristics (h) of PtPd NPs/graphene nanocomposite; (i) is an enlargement of fig. (h).

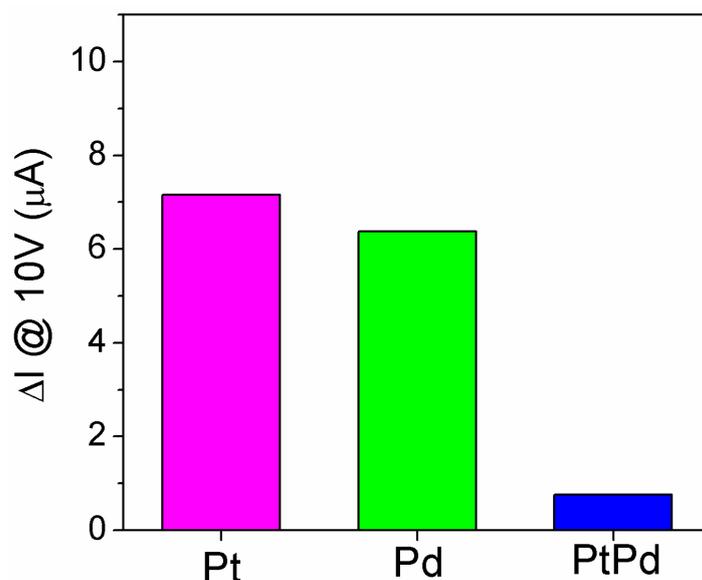


Figure 3.25 Histogram of differences between current Out of NPs and On NPs ($\Delta I = \text{Current Out NP} - \text{Current On NP}$ (μA)), measured at voltage of 10 V, for the various type of NPs (Pt, Pd, PdPt) on graphene.

3.4 Conclusions

In this chapter, it was shown that by laser ablation of pure target of Pt/Pd I produced monometallic NPs and by laser ablation of composite $Pt_{80}Pd_{20}$ target, I obtained PtPd bimetallic NPs. The colloids' stability over time is evaluated by UV-Vis spectroscopy. The chemical analysis of the nanoparticles was done by XRD, SAED and EDX techniques, which confirmed the monometallic and bimetallic nature of nanoparticles. Also, through HAADF-STEM measurements, it was found in bimetallic NPs that Pt and Pd are homogeneously distributed on the whole volume of the particles. The average size of the NPs was estimated by TEM images and it is around 10-15 nm.

After the fabrication and the characterization, the NPs have been used to decorate graphene substrates. By using SEM images the surface density of the NPs on graphene was evaluated to be of the order of 10^{10} part/cm².

From the characterization of these NPs/graphene samples, I found that the metal NPs deposited on graphene modify the electronic structure of graphene through charge transfer. In particular, I found a G Raman peak upshift and 2D Raman peak downshift, which indicate a n-doping effect, where the electrons are transferred from the NPs to the graphene layer. I, also, confirmed this effect employing C-AFM measurements: I found that the slopes of the I-V characteristics change due to the effect of the NPs on the graphene. In particular, these changes follow the Raman peak shifts, highlighting that the chemical composition of the NPs drives the charge transfer phenomena.

Such prepared NPs/graphene nanocomposites may find important devices applications in a wide variety of fields which fuel cells, sensors, catalytic reactions and electronic and optical devices, so to exploiting the fascinating synergic properties of Pt/Pd NPs and graphene.

Chapter 3 References

1. M. Yamauchi, H. Kobayashi, H. Kitagawa, Hydrogen Storage Mediated by Pd and Pt Nanoparticles, *Chem. Phys. Chem.*, 10 (2009) 2566 – 2576. <https://doi.org/10.1002/cphc.200900289>
2. P. Suchomel, L. Kvitek, R. Pucek, A. Panacek, A. Halder, S. Vajda, R. Zboril, Simple size-controlled synthesis of Au nanoparticles and their size-dependent catalytic activity, *Scientific Reports*, 8 (2018) 4589. DOI:10.1038/s41598-018-22976-5
3. L. Liu, A. Corma, Metal Catalysts for Heterogeneous Catalysis: From Single Atoms to Nanoclusters and Nanoparticles, *Chem. Rev.*, 118 (2018) 4981–5079. DOI: 10.1021/acs.chemrev.7b00776
4. S. Barcikowski, V. Amendola, G. Marzun, C. Rehbock, S. Reichenberger, D. Zhang, B. Gokce, *Handbook of laser synthesis of colloids*, DuEPublico, 2016.
5. J. Zhang, D. N. Oko, S. Garbarino, R. Imbeault, M. Chaker, A. C. Tavares, D. Guay, D. Ma, Preparation of PtAu Alloy Colloids by Laser Ablation in Solution and Their Characterization, *J. Phys. Chem. C.*, 116 (2012) 13413-13420. <https://pubs.acs.org/doi/abs/10.1021/jp302485g>
6. M. Censabella, V. Torrisi, S. Boninelli, C. Bongiorno, M. G. Grimaldi, F. Ruffino, Laser ablation synthesis of mono- and bimetallic Pt and Pd nanoparticles and fabrication of Pt-Pd/Graphene nanocomposites, 475 (2019) 494-503. <https://doi.org/10.1016/j.apsusc.2019.01.029>
7. M. Bayle, N. Reckinger, A. Felten, P. Landois, O. Lancry, B. Dutertre, J. F. Colomer, A. A. Zahab, L. Henrard, J. L. Sauvajol, M. Paillet, Determining the number of layers in few-layer graphene by combining Raman spectroscopy and optical contrast, *J. Raman Spectrosc.*, 49 (2018) 36-45. DOI: <https://doi.org/10.1002/jrs.5279>
8. F. Mafunè, J. Kohno, Y. Takeda, T. Kondow, Formation of Stable Platinum Nanoparticles by Laser Ablation in Water, *J. Phys. Chem.*

- B 107 (2003) 4218-4223.
<https://pubs.acs.org/doi/abs/10.1021/jp021580k>
9. G. Cristoforetti, E. Pitzalis, R. Spiniello, R. Ishak, M. M. Miranda, Production of Palladium Nanoparticles by Pulsed Laser Ablation in Water and Their characterization, *J. Phys. Chem. C.* 115 (2011) 5073-5083. <https://pubs.acs.org/doi/abs/10.1021/jp109281q>
 10. B. D. Cullity, *Elements of X-ray Diffraction*, Addison-Wesley, Reading, MA, 1978.
 11. R. Esparza, A. Santovena, A. Ruiz-Baltazar, A. Angeles-Pascual, J. Maya-Cornejo, J. Ledesma-Garcia, R. Perez, Study of PtPd Bimetallic Nanoparticles for Fuel Cell Applications, *Mater. Res.* 20 (2017) 1193-1200. <http://dx.doi.org/10.1590/1980-5373-mr-2016-0934>
 12. R. Esparza, A. F. Garzia-Ruiz, J. J. Velázquez Salazar, R. Pérez, M. J. Yacamán, Structural characterization of Pt-Pd core-shell nanoparticles by Cs-corrected STEM, *J. Nanopart. Res.*, 15 (2012) 1342, <https://doi.org/10.1007/s11051-012-1342-2>
 13. J. S. Pennycook, P. D. Nellist, *Scanning Transmission Electron Microscopy: Imaging and Analysis*, Springer Science & Business Media (2011)
 14. G. Zhang, C. Huang, R. Qin, Z. Shao, D. An, W. Zhang, Y. Wang, Uniform Pd-Pt alloy nanoparticles supported on graphite nanoplatelets with high electrocatalytic activity towards methanol oxidation, *J. Mater. Chem. A.*, 3 (2015) 5204–5211. doi:10.1039/c4ta06076h
 15. J. C. Shelton, H. R. Patil, J. M. Blakely, Equilibrium segregation of carbon to a nickel (111) surface: A surface phase transition, *Surface Science*, 43 (1974) 493-520. [https://doi.org/10.1016/0039-6028\(74\)90272-6](https://doi.org/10.1016/0039-6028(74)90272-6)
 16. K. S. Novoselov, A. K. Geim, S. V. Morozov, D. Jiang, Y. Zhang, S. V. Dubonos, I. V. Grigorieva, A. A. Firsov, Electric Field Effect in Atomically Thin Carbon Films, *Science*, 306 (2004) 666–669. doi:10.1126/science.1102896. DOI: 10.1126/science.1102896
 17. M. Censabella, V. Torrisi, G. Compagnini, M. G. Grimaldi, F. Ruffino, Fabrication of Metal Nanoparticles-Graphene

- Nanocomposites and Study of the Charge Transfer Effect, *Physica E: Low-dimensional Systems and Nanostructures*, submitted
18. Y. Seekaew, O. Arayawut, K. Timsorn, C. Wongchoosuk, Chapter Nine - Synthesis, Characterization, and Applications of Graphene and Derivatives, *Carbon-Based Nanofillers and Their Rubber Nanocomposites Carbon Nano-Objects 2019*, Pages 259-283. <https://doi.org/10.1016/B978-0-12-813248-7.00009-2>
 19. X. Du, I. Skachko, A. Barker, E. Y. Andrei, Approaching ballistic transport in suspended graphene *Nat. Nanotechnol.*, 3 (2008) 491–495 <https://doi.org/10.1038/nnano.2008.199>
 20. A. A. Balandin, S. Ghosh, W. Bao, I. Calizo, D. Teweldebrhan, F. Miao and C. N. Lau, Superior Thermal Conductivity of Single-Layer Graphene, *Nano Lett.*, 8 (2008) 902–907. <https://doi.org/10.1021/nl0731872>
 21. S. Pang, Y. Hernandez, X. Feng and K. Mullen, Graphene as Transparent Electrode Material for Organic Electronics, *Adv. Mater.*, 23 (2011) 2779–2795. DOI: 10.1002/adma.201100304
 22. M. Khan, M. N. Tahir, S. F. Adil, H. U. Khan, M. R. H. Siddiqui, A. Al-warthan, W. Tremel, Graphene based metal and metal oxide nanocomposites: synthesis, properties and their applications , *J. Mater. Chem. A*, 3 (2015) 18753. DOI: 10.1039/c5ta02240a
 23. C. Lee, X. Wei, J. W. Kysar and J. Hone, Measurement of the elastic properties and intrinsic strength of monolayer graphene. *Science*, 321 (2008) 385–388. DOI: 10.1126/science.1157996
 24. <https://graphene-supermarket.com/One-wafer-100mm-Graphene-Film-on-Nickel.html>
 25. C. Gong, G. Lee, B. Shan, E. M. Vogel, R. M. Wallace, K. Cho, First-principles study of metal-graphene interfaces, *J. Appl. Phys.* 108 (2010) 123711. <https://doi.org/10.1063/1.3524232>
 26. F. Xu, Y. Sun, Y. Zhang, Y. Shi, Z. Wen, Z. Li, Graphene-Pt nanocomposite for nonenzymatic detection of hydrogen peroxide with enhanced sensitivity, *Electrochem. Commun.* 13 (2011) 1131–1134. <https://doi.org/10.1016/j.elecom.2011.07.017>
 27. S. Guo, S. Dong, E. Wang, Three-dimensional Pt-on-Pd bimetallic nanodendrites supported on graphene nanosheet: facile synthesis

- and used as an advanced nanoelectrocatalyst for methanol oxidation, *ACS Nano*, 4 (2010) 547–555. doi: 10.1021/nn9014483
28. R. Nie, J. Wang, L. Wang, Y. Qin, P. Chen, Z. Hou, Platinum supported on reduced graphene oxide as a catalyst for hydrogenation of nitroarenes, *Carbon N. Y.*, 50 (2012) 586–596. doi: 10.1016/j.carbon.2011.09.017.
 29. Y. Li, Y. Li, E. Zhu, T. McLouth, C. Y. Chiu, X. Huang, Y. Huang, Stabilization of high-performance oxygen reduction reaction Pt electrocatalyst supported on reduced graphene oxide/carbon black composite, *J. Am. Chem. Soc.*, 134 (2012) 12326–12329. doi: 10.1021/ja3031449
 30. B. Seger, P. V. Kamat, Electrocatalytically Active Graphene-Platinum Nanocomposites . Role of 2-D Carbon Support in PEM Fuel Cells Electrocatalytically Active Graphene-Platinum Nanocomposites . Role of 2-D Carbon Support in PEM Fuel Cells, (2009) 7990–7995. doi:10.1021/jp900360k
 31. H. Zhou, F. Yu, H. Yang, C. Qiu, M. Chen, L. Hu, Y. Guo, H. Yang, C. Gub, L. Sun, Layer dependent morphologies and charge transfer of Pd on n-layer graphenes, *ChemComm*, 47 (2011) 9408–9410. DOI: 10.1039/C1CC13338A
 32. A. Das, S. Pisana, B. Chakraborty, S. Piscanec, S. Saha, U. Waghmare, K. Novoselov, H. Krishnamurthy, A. Geim, A. Ferrari, Monitoring dopants by Raman scattering in an electrochemically top-gated graphene transistor, *Nat. Nanotechnol.*, 3 (2008) 210. DOI:10.1038/nnano.2008.67
 33. A. C. Ferrari, D. M. Basko, Raman Spectroscopy as a versatile tool for studying the properties of graphene, *Nature Nanotechnology*, 8 (2013) 235-246. <https://doi.org/10.1038/nnano.2013.46>
 34. L. M. Malard, M. A. Pimenta, G. Dresselhaus, M. S. Dresselhaus, Raman spectroscopy in graphene, *Physics Reports*, 473 (2009) 51-87. <https://doi.org/10.1016/j.physrep.2009.02.003>
 35. M. W. Iqbal, M. Z. Iqbal, M. F. Khan, X. Jin, C. Hwang, J. Eom, Modification of the structural and electrical properties of graphene layers by Pt adsorbates, *Sci. Technol. Adv. Mater.*, 15 (2014) 055002. doi: 10.1088/1468-6996/15/5/055002

Chapter 4

Light-assisted Impedance Studies of Grain Boundaries in the Thin Film Proton Conductors grown by Pulsed Laser Deposition

In the first chapter, we have seen how perovskite thin films are attracting great attention from the scientific community, especially in the field of fuel cells and, in particular, in Solid Oxide Fuel Cells (SOFCs). For many years, the SOFCs' research has been based on oxygen-ion conductors. Anyway, in recent years, the interest towards High-Temperatures Proton Conductors (HTPCs) is increasing. The great advantage, with respect to oxygen-ion conductors, is that they can achieve high proton conductivity at low temperatures (350°), taking advantage of the relatively low activation energy. Furthermore, in a proton conductor the water is produced at cathode and not at the anode, as instead occurs in an oxygen-ion conductor [1].

In a HTPC the electrolyte is an oxide with perovskite type structure, where the A site is occupied by an alkaline earth element, in particular Barium, while the B site is occupied by a tetravalent element, usually Ce or Zr. To promote protonic conductivity, it is paramount to dope the B-site with trivalent elements, such as Y. This doping leads to the formation of oxygen-ion vacancies, which play a crucial role in the formation of mobile protons [1-4]. They can migrate, by a hopping mechanism, from one oxygen ion to the next (for details see the section 1.1.3).

The work presented in this chapter was carried out at the Paul Scherrer Institut (Villigen, Switzerland), in the "Thin Films and Interfaces Group", where I spent a research period from 1 January to 1 July 2019.

Among the oxide proton conductors, yttrium doped barium zirconate (BZY) shows the best performance. It has good chemical stability and high grain interior conductivity, but the presence of large grain boundary regions results in quite low total conductivity (bulk + grain) [5-11].

The total conductivity could be improved or by decreasing the density of grain boundaries (GBs) or by increasing the specific GB's conductivity.

In literature, the blocking effect is explained by the presence of a space charge layer at the grain boundary. In particular, a positively charged grain boundary core exists at the grain boundary. To compensate the positive charge, a depletion layer of positively charged oxygen vacancies and an accumulation layer of negatively charged dopants are formed at both sides of the grain boundary core (fig. 4.1). Considering that the conductivity is proportional to the oxygen vacancy concentration, the depletion layer of oxygen vacancies at the grain boundary causes high resistance [12-13].

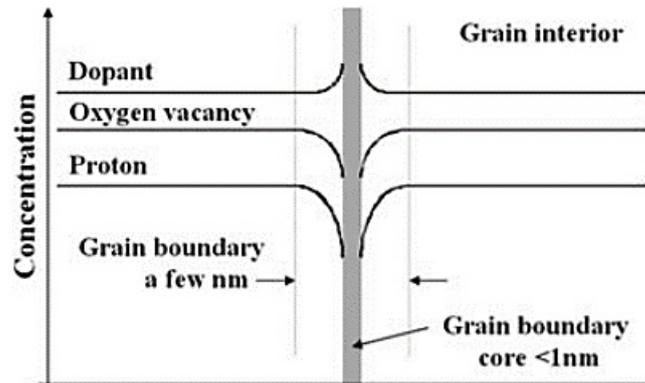


Figure 4.1 Schematic illustration of the space charge layer at the grain boundary [13].

Here, I present preliminary results on the increase of the grain boundary conductivity due to the UV illumination. In particular, epitaxial 20% Y-doped BaZrO₃ films have been grown by PLD on MgO substrate. Impedance Spectroscopy measurements were performed on these films, without and with illumination of the films with an excimer lamp, with wavelength of 222 nm. This photon energy is greater compared to the energy band gap of the BZY.

In this way, the photon can be absorbed and an electron-hole pair created. The photo-generated charges injected into the GB region reduce the width of the space charge layer, therefore lowering the potential barrier for proton transport across the GB.

4.1 Experimental section

Thin films have been grown in an ultrahigh vacuum PLD chamber from Twente Solid State Technology (TSST). KrF laser (Lambda Physics) with a wavelength of 248 nm and a pulse length of 25 ns is used to ablate sintered pellet of 20% Y-doped BaZrO₃. In a PLD process, the stoichiometry of the film usually reflects the stoichiometry of the pellet used as target [11]. The fluence of 2 J/cm² and a repetition rate of 2 Hz were used. A background pressure of O₂ was set at 0.1 mbar. The deposition rates have been accurately calibrated by X-Ray reflectometry (XRR) to be $\approx 0.36 \text{ \AA/pulse}$. The substrates, MgO (001) purchased from Crystec GmbH, was in front of the target at distance of 4 cm (see fig. 4.2.a). High temperature ($>750^\circ\text{C}$) was used during the deposition (fig. 4.2.b) and it was read out with a pyrometer. In order to ensure a reliable temperature reading a drop of Pt paste was dried on the side of the sample holder (fig. 4.2.c), because the emissivity value (0.97) of platinum black was used as setting of the pyrometer.

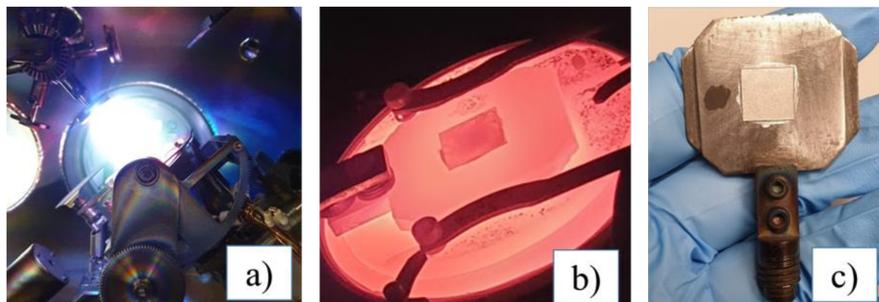


Figure 4.2 Potographs of pulsed laser deposition (a), of high temperature value reached of sample holder (b), of sample holder with a drop of platinum paste for reliable reading of the pyrometer.

Two sets of samples were prepared, labeled sets A and B, which differ for the different film thickness (the samples A are thicker while samples B are thinner). Each set consists of three samples with different growth parameters, see Tables 4.1 and 4.2. In particular, A3 sample has been grown with the aim to reproduce the sample A1.

Tab. 4.1 Thick samples with different growth parameters

Sample A	Thickness [nm]	Grown temperature [°C]
A1	500	770
A2	250	780
A3	500	773

Tab. 4.2 Thin samples with different growth parameters

Sample B	Thickness [nm]	Grown temperature [°C]
B1	36	755
B2	36	780
B3	39	767

Crystalline structure was analyzed in $\omega - 2\theta$ scan mode with a Seifert diffractometer with monochromatic $\text{CuK}\alpha 1$ radiation ($\lambda=1.5418 \text{ \AA}$, 40kV, 30 mA). The film thickness of the B samples was checked with XRR.

For the thick samples (A serie), the film thickness was checked with Scanning Electron Microscope (FE-SEM, Hitachi, S-4800).

A magneton sputtering equipped in the loadlock of the TSST chamber, is used to deposite Pt electrodes~150 nm (40 mW, 12 minutes, 7.5×10^{-2} mbar). Pt electrodes were deposited on the thin films using a shadow mask wich patterns two strips (8 mm width) separated by a distance of 1 mm (the conduction channel). A schematic representation is shown in fig. 4.3.a.

Au wires has been glued with silver paste in order to connect the electrodes to the electronics for the electrical characterization (fig. 4.3.b).

Electrical characterizations were performed by Impedance Spectroscopy, in-plane direction, in wet argon atmosphere, with a Solatron 1260 impedance/gain phase analyzer. The excitation voltage was 3V in the frequency range between 1 Hz to 1 MHz and in the temperature range between 180 to 300°C. Z plot software was used for the measurements and Zview software was used to fit the complex impedance plane plots with RC parallel circuit, shown in fig. 4.3.c. The proton conductivity was calculated using the follow equation, where R is the resistance, t is the thickness of the thin film, w and L are respectively the width and the distance of the Pt electrodes.

$$\sigma = \frac{L}{w} \frac{1}{t R} \quad [4.1]$$

The UV-Visible absorption spectrum of BZY has been recorded by using a UV/Vis/near-IR Spectrometer (Varian Cary 500).

An excimer lamp KrCl* glow discharge at 222 nm was used to illuminate the sample during the impedance spectroscopy measurements, in a homemade experimental apparatus.



Figure 4.3 Schematic representation (a) of the two electrodes (width w , distance L) deposited on the thin film (thickness t). Photograph of the sample after glued Au wires for electrical characterization (b). RC parallel circuit used to fit the data (c).

4.2 Results and discussion

The crystalline structure of BaZrO_3 is cubic, with lattice parameter of 4.1973 \AA . The substitution of Y in Zr sites determines an increase of the unit cell volume, $a = 4.223 \text{ \AA}$ [11, 14, 15]. PLD is a growth technique that allows a fine control of crystallinity and composition.

The chemical composition of the films was analyzed with RBS and Particle Induced X-ray Emission (PIXE) (Fig. 4.4). In particular, with RBS has been obtained the ratio of Ba:(Zr+Y):O. The masses of Zr and Y are too similar to be distinct with RBS, for this reason, the ratio Zr:Y has been obtained with PIXE. The film composition found to be $\text{Ba}_{0.98}\text{Zr}_{0.82}\text{Y}_{0.21}\text{O}_{2.85}$, with error for Ba, Y, Zr are ± 0.02 and for O ± 0.11 , in good agreement with the target composition (20% Y-doped BaZrO_3) [16].

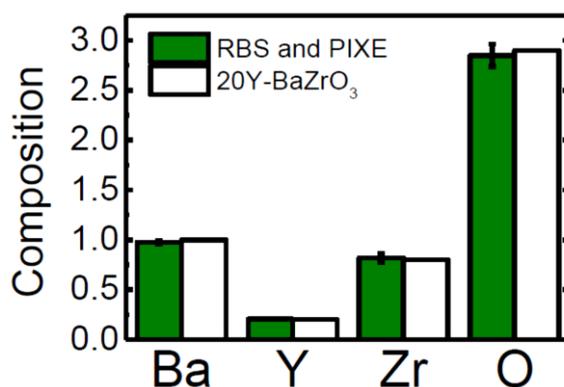


Figure 4.4 Compositional analysis of BZY film. The composition is obtained with a combination of RBS and PIXE measurements. The composition of 20% Y-doped BaZrO_3 is shown for comparison [16].

However, to ensure a highly crystalline growth, a good crystallographic matching between the substrate and the film is required ($a_{\text{film}} \approx a_{\text{substrate}}$). I have chosen (001) oriented MgO as substrate for two reasons: first because has the same cubic symmetry ($a = 4.212 \text{ \AA}$), allowing good epitaxial growth, and, in addition, it is insulating, allowing electrical characterizations of the thin films.

XRD patterns of the prepared BZY films are shown in fig. 4.5. In particular, fig. 4.5.a shows the out-of-plane $\omega - 2\theta$ scan of the sample A1: the (002) reflection of the MgO substrate and of the BZY and the (001) reflection of the film (forbidden for the substrate) are present; there are also two other small peaks due to other orientations, highlighting that the film is highly textured BZY film and not perfectly epitaxial. This probably because the film's thickness is ≈ 500 nm, indeed, when the film grows some crystalline defects (grain boundary, dislocations) can determine the loss of the epitaxial growth relationship, introducing, for example, nucleation points of crystallites with different orientations [16]. Instead, fig. 4.5.b shows the XRD pattern of B1 sample, where is confirmed the epitaxial (001) orientation of the BZY thin film: there is the (001) peak, with weak intensity, and the (002) reflection of film overlaps with the MgO reflection.

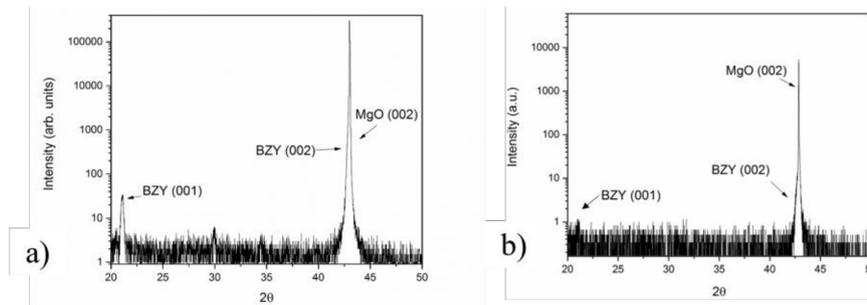


Figure 4.5 Out-of-plane $\omega - 2\theta$ scan of A1 (highly textured) (a) and B1 (epitaxial) (b) sample.

The thicknesses of thin sample (B serie), indicated in tab. 4.2, have been evaluated by XRR. In particular, in fig. 4.6 is shown the XRR spectrum of sample B1. The film thickness t is calculated as follows

$$t = \frac{\lambda}{2 * \sqrt{\frac{\Delta\theta^2}{\Delta n^2}}} \quad [4.2]$$

where λ is the wavelength, n the order of diffraction, θ the value of the minimum and $\frac{\Delta\theta^2}{\Delta n^2}$ is the slope obtained from linear fit of θ^2 versus n^2 .

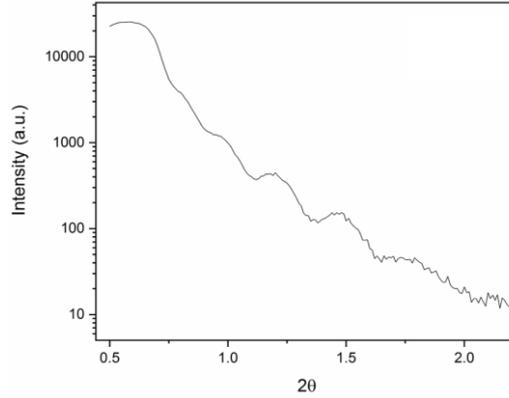


Figure 4.6 X-Ray Reflectivity spectra of B1 sample.

Impedance spectroscopy in humidified Ar atmosphere is used to evaluate the conductivity of the sample. Impedance spectra recorded in this work, because we are considering thin films, exhibit only one semicircle in the Niquyst plot (Z' vs iZ'') where the intercept with the x-axis determines the resistance value. This resistance value is a total resistance, that takes into account the contributions of the grain boundary and bulk resistances, which, in bulk samples, would be distinguishable in two different semicircles.

The figure 4.7 shows Niquyst plots obtained at two different temperatures, for B1 sample, taken as general example: higher temperatures determine a lower resistance, and therefore a smaller semicircle. By using the formula 4.1, from resistance value is possible to calculate the conductivity, and since from the Nernst-Eistein equation the conductivity can be written as

$$\sigma = \frac{A}{T} \exp\left(-\frac{E_a}{kT}\right) \quad [4.3]$$

where A is a temperature independent factor. In figure 4.8 are plotted the conductivities as a function of $1/T$ (Arrhenius plot) and the resulting slope corresponds to activation energy for proton conduction, E_a [16].

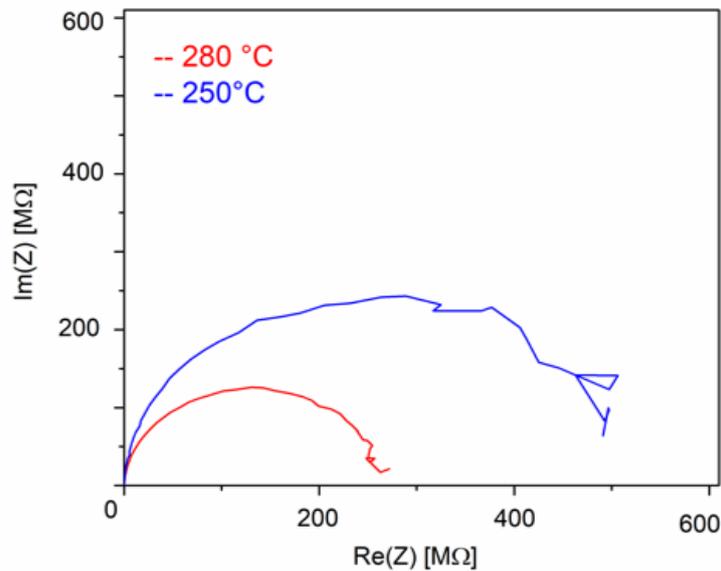


Figure 4.7 Nyquist plots of B1 sample at 280°C (red line) and 250°C (blue line).

The black dots in figure 4.8 represent the conductivity, at different temperature, of thicker sample (A1). In this case the activation energy was $E_a=0.59$ eV. Instead, the thinner samples (B serie) have a higher conductivity and lower activation energy compared to the highly-textured sample (A1). The best conductivity and lowest activation energy ($E_a = 0.44$ eV) are obtained for the sample B2, with thickness 36 nm and growth at 780°C.

From these results is highlighted that the growth temperature during the PLD process (shown at right of the fig. 4.8) influences the conductivity of the film. In addition, the sample's dehydration starts at about 300 °C, in fact is possible to see in the fig. 4.8, marked with the red circle, that the slope of the conductivity varies drastically above 300°C.

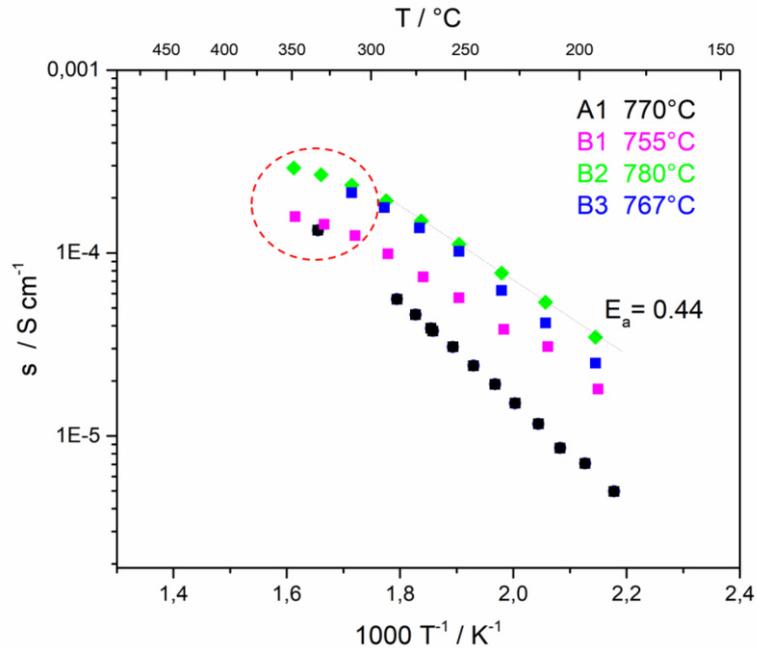


Figure 4.8 The Arrhenius plots of the conductivity for different samples, measured in wet Ar.

In order to calculate the Energy band gap value of BZY, one film has been grown on double side polished MgO substrate. By using UV-Vis spectrophotometer, the absorbance was checked and it is shown in figure 4.9.a. The type of electronic transition in BZY is assumed to be indirect by Hou [17] and Cavalcante [18]. The optical band gap energy (E_g) was calculated by the method proposed by Wood and Tauc [19] determined from the intercept of the fitted straight line in a plot of $(\alpha h\nu)^{1/2}$ versus photon energy ($h\nu$) (fig. 4.9.b). The used equation is the following:

$$\alpha h\nu \propto (h\nu - E_g)^n$$

where α is absorption coefficient, ν is the frequency, h is Planck's constant and $n=2$ for indirectly allowed transition. The optical band gap of the 20% Y-

doped BaZrO₃ was 4.97 eV, which is quite close to value reported by Leonidov et al. [20].

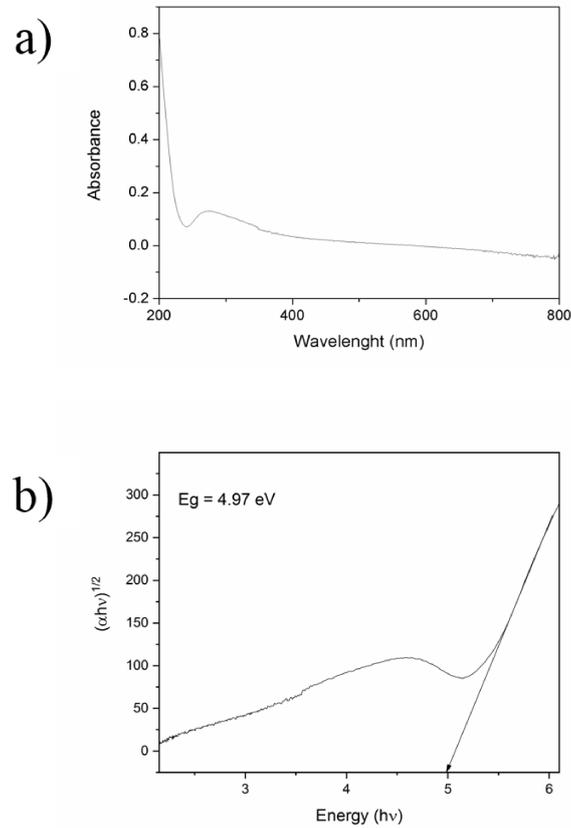


Figure 4.9 UV–Vis absorbance spectrum of 20% Y-doped BaZrO₃ (a) and Tauc plot of $(\alpha h\nu)^{1/2}$ versus photon energy (eV) (b).

The electrical measurements with contemporaneous illumination have been performed in a homemade experimental apparatus, equipped with an excimer lamp of KrCl with wavelength of 222 nm, under hydration in wet Ar. A photograph of the sample under illumination is shown in fig. 4.10.a. The measurements have been done at different temperatures, in dark and under

illumination, after leaving the lamp on for some minutes in order to stabilize the power. In figure 4.10.b is shown the Arrhenius plot for B2 sample (the sample that showed the better conductivity): how is possible to see, the illumination with the lamp didn't change the conductivity of the sample, which remained the same with and without illumination. The same measurement were performed for the other two thin sample, but again there was no change in the conductivity due to the lamp.

Figure 4.11.a shows the electrical characterization of thick sample A1, with and without illumination. On the contrary, in this case, the conductivity of the sample under illumination is higher compared to the one without lighting. The same measurements have been performed on the sample A2, film thickness ≈ 250 nm (fig. 4.11.b), but the effect of the illumination on the conductivity is not so evident.

Based on these results, I can assert that the film's thickness is a critical parameter on the modulation of grain boundary conductivity due to the illumination with the lamp. This because the film thickness determines how many photons are absorbed by the film and, consequently, how many electron-hole pairs are created. Probably the A2 and B serie samples are too thin to ensure a photons' absorption such as to be able to reduce the space charge layers at the grain boundary and, therefore, to change the conductivity.

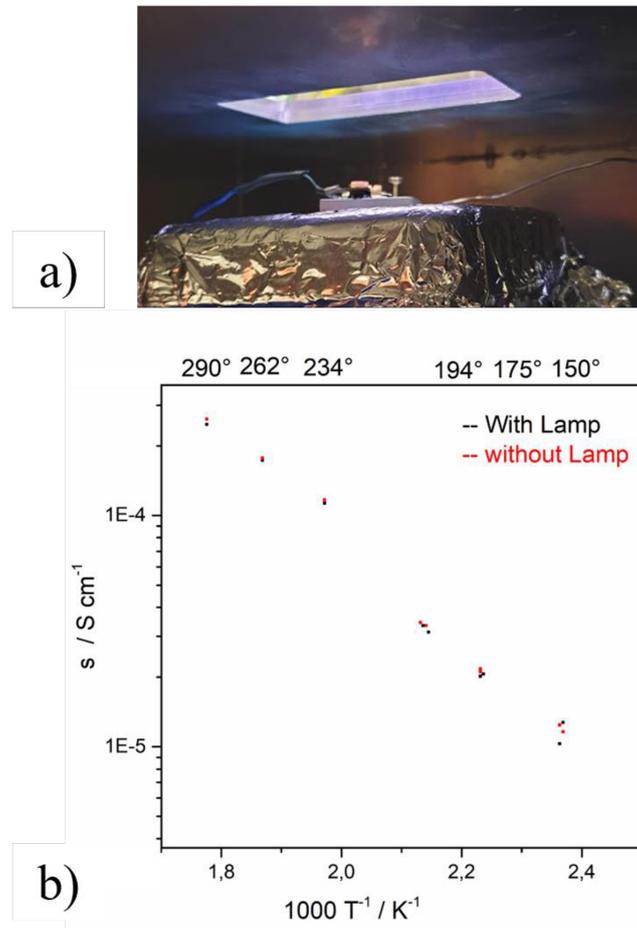


Figure 4.10 Photograph of B2 sample under illumination with an excimer lamp at 222 nm of wavelength (a). The Arrhenius plot for B2 sample: no changes of the conductivity due to the illumination with the excimer lamp (b).

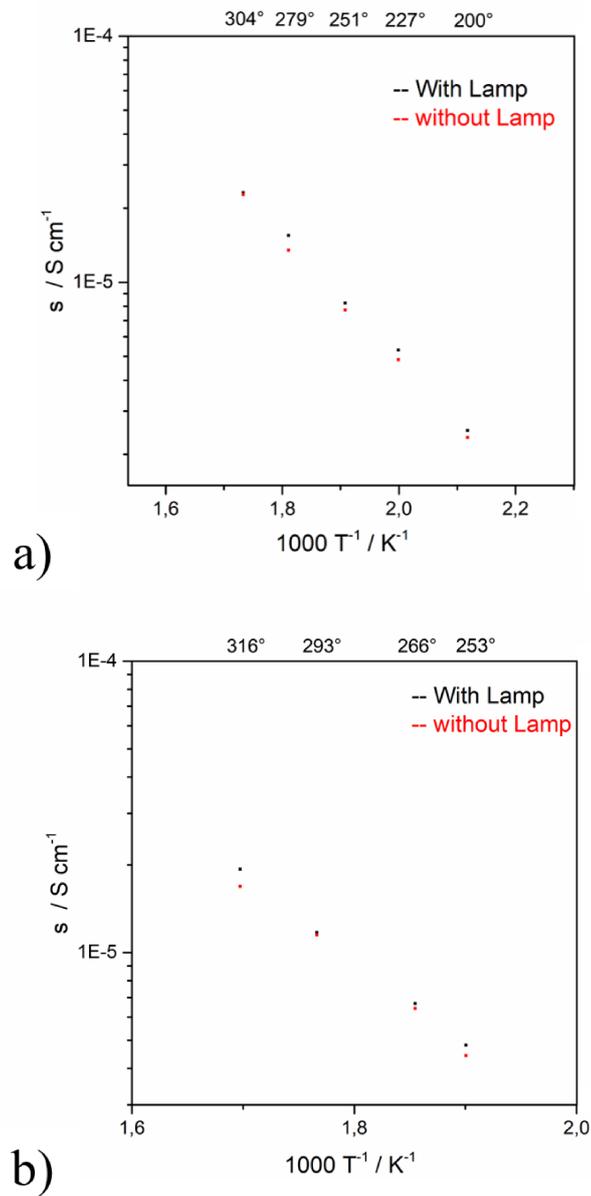


Figure 4.11 The Arrhenius plot for A1 (a) and A2 (b) sample: the film's thickness is a critical parameter on the modulation of conductivity due to illumination with the lamp.

In order to confirm the reproducibility of the obtained results, the electrical characterization have been performed on the sample A3, growth with the same characteristics of the sample A1 (thickness ≈ 500 nm, growth temperature $\approx 770^\circ\text{C}$). Also in this case, the conductivity is higher under illumination (fig. 4.12.a).

Furthermore, in order to confirm that the effect hasn't been caused by the increasing in temperature on the electrodes' surface due to illumination, the electrodes of the sample A3 have been covered with kapton tape, as shown in the insert in figure 4.12.b. In fact, as reported in the literature [21-23], the kapton tape absorbs the UV light in the same energy range of the excimer lamp. In this way, the only component of the sample able to absorb the radiation is represented by the exposed part of the film between the two electrodes. As shown in figure 4.12.b, also in this case, an increase in the conductivity under illumination was measured; the temperature range in this case has been kept below 250°C to avoid kapton's damage.

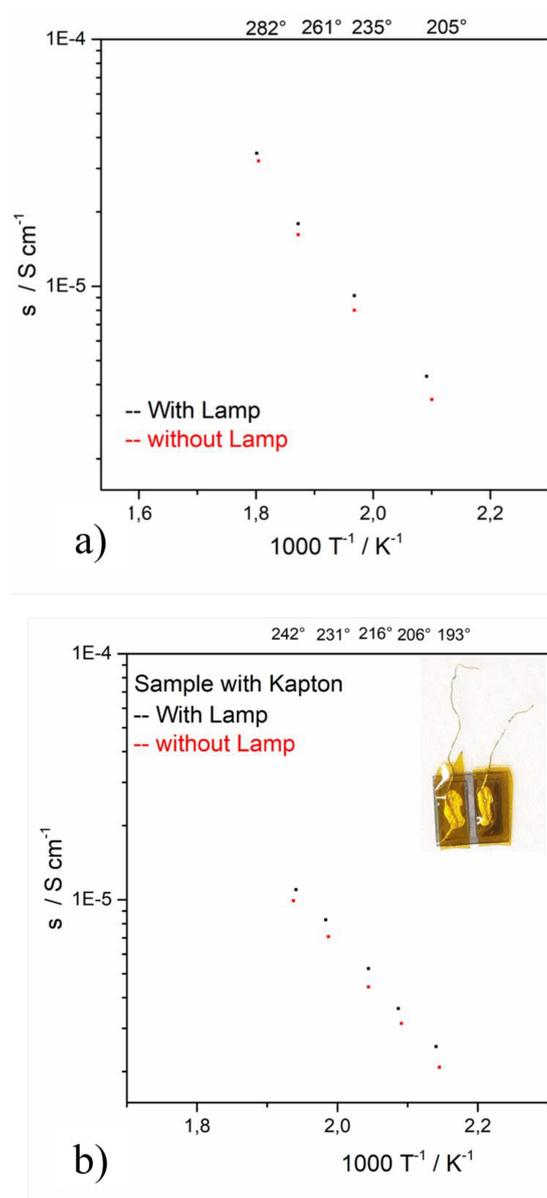


Figure 4.12 The Arrhenius plot for A3 (a) and A3 sample with the electrodes covered with kapton tape (b). In both cases, the conductivity is higher under illumination.

4.3 Conclusions

In this chapter have been shown the fabrication and the characterization of perovskite thin films of 20% Y-doped BaZrO₃ by using Pulsed Laser Deposition on single crystal substrate ((001) MgO). The crystalline structure and the thickness of these films have been characterized by using XRD and XRR. Pt electrodes have been deposited on the films by sputtering deposition and the electrical measurements were performed by impedance spectroscopy. The highest conductivity and lowest activation energy ($E_a = 0.44$ eV) are obtained for the thinner sample, with thickness 36 nm, and higher growth temperature 780°C. So, I can affirm that the growth temperature, during the PLD process, influences the conductivity of the film.

In addition, impedance spectroscopy measurements were performed illuminating the films with an excimer lamp, with wavelength of 222 nm. Under illumination the photons can be absorbed by the film and electron-hole pairs created; these electrons and holes can recombine at grain boundary regions, reducing the width of the space charge layer and, therefore, increasing the grain boundary conductivity. In particular, the film's thickness is a critical parameter on the modulation of conductivity due to the illumination with the lamp. This because the film thickness determines how many photons are absorbed by the film. In fact, I found in thicker sample (≈ 500 nm) that the proton conductivity is higher under illumination and decreases without illumination, instead in thin film the conductivity doesn't change under illumination. This, probably, because the samples are too thin to ensure a photons' absorption such as to be able to reduce the space charge layers at the grain boundary.

Chapter 4 References

1. E. Fabbri, D. Pergolesi, E. Traversa, Materials challenges toward proton-conducting oxide fuel cells: a critical review, *Chem. Soc. Rev.*, 39 (2010) 4355-4369. DOI: 10.1039/B902343G
2. H. Uchida, N. Maeda and H. Iwahara, Relation between proton and hole conduction in SrCeO₃-based solid electrolytes under water-containing atmospheres at high temperatures, *Solid State Ionics*, 11 (1983), 117–124. [https://doi.org/10.1016/0167-2738\(83\)90048-6](https://doi.org/10.1016/0167-2738(83)90048-6)
3. H. Iwahara, T. Yajima, T. Hibino and H. Ushida, Performance of Solid Oxide Fuel Cell Using Proton and Oxide Ion Mixed Conductors Based on BaCe_{1-x}Sm_xO_{3-α}, *J. Electrochem. Soc.*, 140 (1993) 1687–1691. doi: 10.1149/1.2221624
4. N. Bonanos, K. S. Knight, B. Ellis, Perovskite solid electrolytes: Structure, transport properties and fuel cell applications, *Solid State Ionics*, 79 (1995) 161–170. [https://doi.org/10.1016/0167-2738\(95\)00056-C](https://doi.org/10.1016/0167-2738(95)00056-C)
5. E. Fabbri, A. D'Epifanio, E. Di Bartolomeo, S. Licoccia, E. Traversa, Tailoring the chemical stability of Ba (Ce_{0.8-x}Zr_x) Y_{0.2}O₃ protonic conductors for intermediate temperature solid oxide fuel cells (IT-SOFCs), *Solid State Ion.*, 179 (2008) 558-564 <https://doi.org/10.1016/j.ssi.2008.04.002>
6. H. G. Bohn, T. J. Schober, Electrical conductivity of the high-temperature proton conductor BaZr_{0.9}Y_{0.1}O_{2.95}, *J. Am. Ceram. Soc.*, 83 (2000) 768-772. <https://doi.org/10.1111/j.1151-2916.2000.tb01272.x>
7. P. Babilo P., S. M. Haile, Enhanced sintering of yttrium-doped barium zirconate by addition of ZnO, *J. Am. Ceram. Soc.*, 88 (2005) 2362-2368. DOI: 10.1111/j.1551-2916.2005.00449.x
8. K. Katahira, Y. Kohchi, T. Shimura, H. Iwahara, Protonic conduction in Zr-substituted BaCeO₃, *Solid State Ion.*, 138 (2000) 91-98. [https://doi.org/10.1016/S0167-2738\(00\)00777-3](https://doi.org/10.1016/S0167-2738(00)00777-3)
9. K. D. Kreuer, Aspects of the formation and mobility of protonic charge carriers and the stability of perovskite-type oxides, *Solid*

- State Ion., 125 (1999) 285-302. [https://doi.org/10.1016/S0167-2738\(99\)00188-5](https://doi.org/10.1016/S0167-2738(99)00188-5)
10. K. D. Kreuer, Proton-Conducting Oxides, *Annu. Rev. Mater. Res.*, 33 (2003) 333–359. <https://doi.org/10.1146/annurev.matsci.33.022802.091825>
 11. D. Pergolesi, E. Fabbri, A. D'Epifanio, E. Di Bartolomeo, A. Tebano, S. Sanna, S. Licoccia, G. Balestrino, E. Traversa, High proton conduction in grain-boundary-free yttrium-doped barium zirconate films grown by pulsed laser deposition, *Nat. Mater.*, 9 (2010) 846-852. doi: 10.1038/nmat2837
 12. C. Kjolseth, H. Fjeld, Ø. Prytz, P. I. Dahl, C. Estournès, R. Haugrud, T. Norby, Space-charge theory applied to the grain boundary impedance of proton conducting $\text{BaZr}_{0.9}\text{Y}_{0.1}\text{O}_{3-\delta}$, *Solid State Ionics*, 181 (2010) 268–275. <https://doi.org/10.1016/j.ssi.2010.01.014>
 13. F. Iguchi, N. Sata and H. Yugami, Proton transport properties at the grain boundary of barium zirconate based proton conductors for intermediate temperature operating SOFC, *J. Mater. Chem.*, 20 (2010) 6265–6270. DOI:10.1039/C0JM00443J
 14. Y. B. Kim, T. M. Gur, H-J. Jung, R. Sinclair, F. B. Prinz, Effect of crystallinity on proton conductivity in yttrium-doped barium zirconate thin films, *Solid State Ionics*, 198 (2011), 39. DOI: 10.1016/j.ssi.2011.07.004
 15. K. Bae, D. Y. Jang, S. M. Choi, B. K. Kim, J-H Lee, J-W. Son, J. H. Shim Influence of background oxygen pressure on film properties of pulsed laser deposited Y:BaZrO₃, *Thin Solid Films*, 552 (2014) 24. <https://doi.org/10.1016/j.tsf.2013.12.006>
 16. A. Fluri, A. Marcolongo, V. Roddatis, A. Wokaun, D. Pergolesi, N. Marzari, T. Lippert, Enhanced Proton Conductivity in Y-Doped BaZrO₃ via Strain Engineering, *Adv. Sci.*, 4 (2017), 1700467-76. <https://doi.org/10.1002/advs.201700467>
 17. M. Huo, C. LK. Fu, Q. Guo, H. Liao, X. L. Deng, C. Y. Zhang, First principle study on electronic structures of barium zirconate titanate (BZT). *J Funct Mater.*, 42 (2011) 877–879.

18. L.S. Cavalcante, V.M. Longo, M. Zampieri, J.W.M. Espinosa, P.S. Pizani, J.R. Sambrano, J.A. Varela, E. Longo, M.L. Simões, C.A. Paskocimas, Experimental and theoretical correlation of very intense visible green photoluminescence in BaZrO₃ powders, *J. Appl. Phys.*, 103 (2008), 063527. <https://doi.org/10.1063/1.2901176>
19. D. L. Wood, J. Tauc, Weak absorption tails in amorphous semiconductors. *Phys Rev B.*, 5 (1972) 3144–3151. <https://doi.org/10.1103/PhysRevB.5.3144>
20. I. I. Leonidov, V. I. Tsidilkovski, E. S. Tropin, M. I. Vlasov, L. P. Putilov, Acceptor doping, hydration and band-gap engineering of BaZrO₃, *Materials Letters*, 212 (2018), 336-338. <https://doi.org/10.1016/j.matlet.2017.10.114>
21. Y. M. Jang, J. Y. Seo, K. H. Chae, M. H. Yi, Positive-type photosensitive polyimide based on a photobase generator containing oxime-urethane groups as a photosensitive compound, *Macromol. Res.*, 14 (2006) 300-305. <https://doi.org/10.1007/BF03219085>
22. S. Venkatachalam, M. Depriester, A. HadjSahraoui, B. Capoen, M. R. Ammar, D. Hourlier, Thermal conductivity of Kapton-derived carbon, *Carbon*, 114 (2017) 134-140. <https://doi.org/10.1016/j.carbon.2016.11.072>
23. H. S. Virk, Physical and chemical response of 70 MeV carbon ion irradiated Kapton-H polymer, *Nuclear Instruments and Methods in Physics Research Section B: Beam Interactions with Materials and Atoms*, 191 (2002) 739-743. [https://doi.org/10.1016/S0168-583X\(02\)00644-4](https://doi.org/10.1016/S0168-583X(02)00644-4)

Summary and Conclusions

In this thesis, the growth and fabrication of nanostructures by using laser-based techniques is presented. In fact, laser technique is versatile, simple, low-cost, high-throughput and environmentally friendly. In addition, with this method is possible to control the size, shape and composition of the manufactured materials, simply by changing some experimental parameters.

In particular, in this work, I presented three different laser-based techniques to fabricate nanostructures: laser irradiation of thin film deposited on surface, laser ablation in liquid environment and pulsed laser deposition.

By laser irradiation of deposited films, I produced mono- and bimetallic Pt/Pd NPs on FTO substrate. The NPs have been characterized from a point of view morphological and chemical. In particular, the NPs presented an average size > 50 nm, depending on the thickness of the irradiated film and of the substrate's topography.

By laser ablation of pure Pt/Pd target I produced monometallic NPs and by laser ablation of composite PtPd target I obtained PtPd bimetallic NPs. The average size of the NPs has been estimated to be around 10-15 nm. After the fabrication and the complete characterization, the NPs have been used to decorate graphene substrates. From the characterization of these NPs/graphene hybrid nanocomposite, I found that the metal NPs deposited on graphene modify the electronic structure of graphene through charge transfer and that the chemical composition of the NPs drives such charge transfer phenomena.

By using pulsed laser deposition, perovskite thin films of 20% Y-doped BaZrO₃ have been fabricated. The crystalline structure and the thickness of these films have been characterized. The electrical performance of these films showed that the growth temperature, during the PLD process, influences the

conductivity of the film. In addition, illuminating the BZY films with an excimer lamp, the increasing of the protonic conductivity at grain boundary has been showed.

To conclude, laser based techniques has been employed to fabricate 0-D and 2-D nanostructures, with different elemental and structural composition. Such fabricated nanostructures may find important devices applications in a wide variety of fields which fuel cells, sensors, catalysis and electronic and optical devices.

List of publications

This thesis is based on the following publications:

1. **M. Censabella**, V. Torrisci, G. Compagnini, M. G. Grimaldi, F. Ruffino, Fabrication of Metal Nanoparticles-Graphene Nanocomposites and Study of the Charge Transfer Effect, *Physica E: Low-dimensional Systems and Nanostructures*, Under review
2. **M. Censabella**, V. Torrisci, S. Boninelli, C. Bongiorno, M. G. Grimaldi, F. Ruffino, Laser ablation synthesis of mono- and bimetallic Pt and Pd nanoparticles and fabrication of Pt-Pd/Graphene nanocomposites, *Applied Surface Science*, 475 (2019) 494-503. <https://doi.org/10.1016/j.apsusc.2019.01.029>
3. V. Torrisci , **M. Censabella**, G. Piccitto, G. Compagnini, M. G. Grimaldi, F. Ruffino, Characteristics of Pd and Pt Nanoparticles Produced by Nanosecond Laser Irradiations of Thin Films Deposited on Topographically-Structured Transparent Conductive Oxides, *Coatings*, 8 (2018) 68. <https://doi.org/10.3390/coatings9020068>
4. **M. Censabella**, F. Ruffino, M. Zimbone, E. Bruno, M. G. Grimaldi, Self-Organization Based Fabrication of Bimetallic PtPd Nanoparticles on Transparent Conductive Oxide Substrates, *Phys. Status Solidi A*, 215 (2017) 1700524-1700524. <https://doi.org/10.1002/pssa.201700524>

Other publications:

5. **M. Censabella**, M. G. Grimaldi, F. Ruffino, Shape design of supported Au nanorods through morphological evolution: Coalescence, instability, reshaping, *Materials Characterization*, 147 (2019) 101-115 <https://doi.org/10.1016/j.matchar.2018.11.001>
6. A. Scandurra, F. Ruffino, **M. Censabella**, A. Terrasi, M. G. Grimaldi, Gold Nanoparticles-Graphene Paper Composite as High Efficient Electrochemical Glucose Sensor, submitted.

7. F. Ruffino, **M. Censabella**, V. Torrasi, M. G. Grimaldi, Size-selected growth of ultrathin SiO₂ nanowires on surface and their decoration by Au nanoparticles, *Materials Research Express*, 2 (2015) 025003. DOI: 10.1088/2053-1591/2/2/025003
8. F. Ruffino, **M. Censabella**, M. G. Grimaldi, Dewetted Pt Nanostructures on Silicon Carbide Surface, *Journal of Physics and Chemistry of Solids*, Under review
9. A. Marcelli, **M. Censabella**, L. Faillace, M. G. Grimaldi, G. Keppel, S. Macis, C. Pira, J. Scifo, B. Spataro, Nb superconductive thin film coating on flat Cu disks for high gradient applications. INFN-19-15/LNF, PrePrint published online at www.inf.infn.it

Conferences

Oral contributions:

1. **M. Censabella**, V. Torrasi, G. Compagnini, M. G. Grimaldi, F. Ruffino, Experimental Study of the Charge Transfer Effect in Graphene-Metal Nanoparticles Hybrid Composites, **FisMat 2019**, Catania (Italy);
2. **M. Censabella**, V. Torrasi, S. Boninelli, C. Bongiorno, M. G. Grimaldi, F. Ruffino Fabrication of Metal Nanoparticles-Graphene Nanocomposites and Study of the Charge Transfer Effect, **NanoInnovation 2018**, Rome (Italy);
3. **M. Censabella**, V. Torrasi, S. Boninelli, C. Bongiorno, M. G. Grimaldi, F. Ruffino, Laser ablation synthesis of Pd and Pt nanoparticles and fabrication of Pd/Pt-Graphene nanocomposites, **European Materials Research Society, Spring Meeting 2018**, Strasbourg (France).

Poster contributions:

4. **M. Censabella**, V. Torrisi, G. Compagnini, M. G. Grimaldi, F. Ruffino, Experimental Study of the Charge Transfer Effect in Graphene-Metal Nanoparticles Hybrid Composites, **European Materials Research Society, Spring Meeting 2019**, Nice (France).
5. A. L. Sortino, **M. Censabella**, G. Munzi, S. Boninelli, F. Ruffino, V. Privitera, Laser-based synthesis of gold nanostructures for optical sensing of glyphosate, **European Materials Research Society, Spring Meeting 2019**, Nice (France).
6. M. Zimbone, G. Cacciato, **M. Censabella**, M. Boutinguiza, V. Privitera and M. G. Grimaldi, Facile and Scalable Synthesis of Black-TiO_x for Environmental Water Purification, **European Materials Research Society, Spring Meeting 2017**, Strasbourg (France).
7. **M. Censabella**, F. Ruffino, M. Zimbone, E. Bruno, G. Pellegrino, M. G. Grimaldi, Self-organization based fabrication of bimetallic Pd-Pt nanoparticles on transparent conductive oxide substrates, **European Materials Research Society, Spring Meeting 2017**, Strasbourg (France)

Awards

Young Scientist Award at Symposium X of the E-MRS Spring Meeting 2018: “Photon assisted synthesis and processing of materials in nanomicroscale”

Schools and Workshops

- **Scanning Electron Microscopy School in Materials Science**, 12-15 December 2017, Bologna (Italy)

- **Workshop Italia-Israele: Materials and Technologies for Industrial Innovation**, 16-17 Ottobre 2018, Catania (Italy).
- **Scanning Probe Microscopy**, March-May 2017, Catania (Italy).
- **Accelerator based Materials Science at ETH**, 27 June 2019, Swiss Federal Institute of Technology in Zurich, (Switzerland).

Research Period Abroad

Guest PhD Student at Thin films and Interfaces Group, Paul Scherrer Institut, Villigen (Switzerland). January-July 2019

ETH

Eidgenössische Technische Hochschule Zürich
Swiss Federal Institute of Technology Zurich

Paul Scherrer Institut
Forschungsstrasse 111
5232 Villigen PSI
Switzerland

+41 56 310 21 11
www.psi.ch

Prof. Dr. Dr. h.c. Thomas Lippert
Research with Neutrons and Muons Division
OFLB/U110

direct +41 56 310 40 76
thomas.lippert@psi.ch

Department of Chemistry and Applied Biosciences

Laboratory of Inorganic Chemistry
ETH Zürich
CH-8093 Zürich
www.lac.ethz.ch

Villigen PSI, 22 July 19

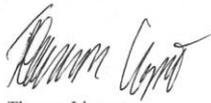
To whom it may concern:

We hereby (Prof. Dr. Thomas Lippert and Dr. Daniele Pergolesi) confirm that the Ph.D. student Maria Censabella has spent a research period at the *Paul Scherrer Institut* (Villigen, Switzerland) in the *Thin Films and Interfaces Group* from 07/01/2019 to 01/07/2019.

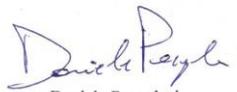
During this period, she worked on the investigation of the space charge effect at the grain boundary of proton conducting oxides, a project which is performed in collaboration with MIT and Kyushu University.

Maria used *Pulsed Laser Deposition* (PLD) to grow epitaxial thin films and characterized the crystalline structure and the thickness of these films with X-Ray Diffraction and Reflectometry. In addition, she performed electrical characterizations with electrochemical impedance spectroscopy (EIS).

She also attended the "Accelerator based Materials Science at ETH" Workshop on 27 June 2019.



Thomas Lippert



Daniele Pergolesi

Villigen, July 22, 2019

Curriculum Vitae

Maria Censabella was born in June 22, 1988 in Catania. She attained her Master Degree in Physics with full marks (110/110) on 23th of March 2016 at the University of Catania. In November 2016, she started the PhD course in Materials Science and Nanotechnology at the University of Catania and CNR-IMM. She is currently working (post-doc position) under the supervision of Prof. Maria Grazia



Grimaldi and Prof. Francesco Ruffino at the University of Catania, Dep. of Physics and Astronomy “Ettore Majorana”. She spent part of her PhD course (January-July 2019) at Paul Scherrer Institut (Villigen, Switzerland), in the “Thin films and Interfaces Group” under the supervision of Prof. Thomas Lippert and Dr. Daniele Pergolesi. Her main scientific interests are focused on the fabrication of metal nanoparticles and thin films by using laser based techniques. She was tutor of the course of Physics for the Course of Food Science and Technology at the University of Catania. She was PhD students’ representative in the Lecturer’s Committee of the PhD Programme and the Council of the Department of Physics and Astronomy “Ettore Majorana”. During the PhD course she presented the results of her research activity, giving both oral and poster contributions, at the following international conferences: FisMat 2019, Catania (Italy); European Materials Research Society, Spring Meeting 2019, Nice (France); NanoInnovation 2018, Rome (Italy); European Materials Research Society, Spring Meeting 2018, Strasbourg (France); European Materials Research Society, Spring Meeting 2017, Strasbourg (France). She won the Young Scientist Award at Symposium X of the E-MRS Spring Meeting 2018: “Photon assisted synthesis and processing of materials in nanomicroscale”. Maria Censabella is author or co-author of several articles, published in international referred scientific journals.

Acknowledgements

The Phd is a long journey, a great opportunity for everyone to grow, to improve yourself as a scientist, as a worker and as a person. It is a long individual journey but unrealizable alone. For the past three years many people have provided me their essential support.

First of all, I would like to thank Prof. Maria Grazia Grimaldi. She always helped, supported and gave me advices. She is for me an excellent example of a successful woman and scientist.

My deepest gratitude goes to Prof. Francesco Ruffino that accompanied me since my master degree. He is one of the most brilliant and intelligent researcher that I met. I'm also grateful for his human kindness, his patience and for his numerous advices. Thanks also because he daily helps and teaches me how to be a good scientist.

Thanks to the Rector of the University of Catania, Prof. Francesco Priolo, because he always believes in his students and with enthusiasm he infuses the passion for physics.

My gratitude also goes to Dr. Vittorio Privitera who has given me the possibility to work within the CNR-IMM. Thanks for his friendly advices and the many laughs at lunch.

I wish to thank the people I met during the period that I spent at Paul Scherrer Institut because they welcomed me as one of them: Natacha (my favorite French person), Elisa, Christof, Venkat, Zahra, Sibel, Marina, Banani, Eric, Craig, Luca, Xi, Gesara. Thanks to Professor Lippert that allowed me to be part of his beautiful team (Thin Films and Interfaces Group), he also allowed me to use all equipments of his laboratory and he always laughed with me. I really appreciate how he leads his group. A special thanks goes to Dr.

Acknowledgements

Daniele Pergolesi for having “adopted” me in his team, explaining patiently to me everything about proton conductors and PLD; thanks also for his friendly way of speaking and for all advices and laughs. Daniele is the supervisor that every PhD student should have. This experience at PSI was for me one of the best experience of my life, I came out of my comfort zone and I learned that I can do everything if I really want it.

My most sincere thankfulness to all amazing people met in these years: all the staff of researchers, professors, PhD students, fellowships and the funny technician G. Pantè. Thanks to the people that share the office with me: Melanie, Salvo and Nino.

Among the people met during these years there are also those ones who I use to call friends: Maria, Martina, Mario, Giacomo, Alessandro e Saro. With them I shared smiles, gripes, peaceful and madness moments, trips and happiness.

Thanks to my mom and dad, they always believe in me, support, help and love me. Thanks to my brothers and my sister in law because I did the best laughs with them. Thanks to my lovely nephews and nieces that give color to my days and life.

Finally, thanks to my beloved Antonio, for being my best friend and my partner. Thanks because he believes in me even when I do not do it. Antonio and Tobia are the most beautiful gifts that I have ever had. Coming to home and being unconditionally loved fills my heart every day.

